Study and Implementation of Fast Compressive 3-D Total Focusing Method Ultrasonic Imaging Using 2-D Sparse Arrays

by

Lucas PEREIRA PIEDADE

THESIS PRESENTED TO ÉCOLE DE TECHNOLOGIE SUPÉRIEURE IN
PARTIAL FULFILLMENT FOR THE DEGREE OF
DOCTOR OF PHILOSOPHY
Ph.D.

MONTREAL, "APRIL 12TH, 2024"

ÉCOLE DE TECHNOLOGIE SUPÉRIEURE
UNIVERSITÉ DU QUÉBEC

BOARD OF EXAMINERS

THIS THESIS HAS BEEN EVALUATED

BY THE FOLLOWING BOARD OF EXAMINERS

Mr. Pierre Bélanger, Thesis supervisor
Department of Mechanical Engineering, École de technologie supérieure

Mrs. Catherine Laporte, Chair, Board of Examiners
Department of Electrical Engineering, École de technologie supérieure

Mr. Ricardo Zednik, Member of the Jury
Department of Mechanical Engineering, École de technologie supérieure

Mr. Sébastien Bourguignon, External Independent Examiner
École centrale de Nantes

THIS THESIS WAS PRESENTED AND DEFENDED

IN THE PRESENCE OF A BOARD OF EXAMINERS AND THE PUBLIC

ON "MARCH 25TH, 2024"

AT ÉCOLE DE TECHNOLOGIE SUPÉRIEURE

ACKNOWLEDGEMENTS

Étude et Mise en Œuvre d'une Imagerie Ultrasonore 3D Rapide par la Méthode de Focalisation Totale Compressive Utilisant des Approches Parcimonieuses en 2D

Lucas PEREIRA PIEDADE

RÉSUMÉ

Cette thèse explore l'accent croissant mis sur l'imagerie tridimensionnelle dans le contrôle non destructif par ultrasons (CND), mettant l'accent sur l'importance du contrôle ultrasonore par sondes multiéléments (PAUT) et le potentiel émergent de la méthode de focalisation totale (TFM) pour l'imagerie à haute résolution. Lors de l'application de cette méthode dans un contexte d'imagerie en 2D à l'aide de sondes linéaires, des limites apparaissent concernant l'identification des défauts, notamment dans des scénarios avec des orientations aléatoires telles que des fissures, exigeant la nécessité de solutions d'imagerie en 3D. L'étude aborde les défis associés à l'utilisation de l'imagerie volumétrique dans le CND, se concentrant principalement sur les sondes matricielles dans le cadre de la TFM, dans le but de développer des stratégies novatrices d'acquisition ultrasonore et de traitement des données pour améliorer la productivité de la TFM en 3D. Le projet comporte deux aspects clés. Tout d'abord, le projet examine la complexité associée à la gestion d'un grand nombre d'éléments dans les sondes matricielles ultrasonores, explorant des techniques de réduction des éléments, notamment des stratégies de sélection d'éléments telles que les approches parcimonieux. Ensuite, la recherche se concentre sur des méthodologies visant à réduire le volume substantiel de données générées, en examinant des techniques innovantes de compression de données, telles que les approches d'échantillonnage compressif (CS). L'intégration de ces stratégies vise à ouvrir la voie au développement de scanners ultrasonores légers et à poser les bases théoriques de leur réalisation pratique. Premièrement, cette étude a introduit une méthode de conception de réseaux parcimonieux appliquée aux sondes linéaires et l'a comparée à la FMC et à l'imagerie par ondes planes (PWI). Ensuite, cette méthodologie de réseaux parcimonieux a été adaptée et étendue aux sondes matricielles pour optimiser l'efficacité de l'acquisition de données tout en équilibrant la qualité d'imagerie en 3D. Enfin, la méthode de réseaux parcimonieux a été combinée à un cadre CS efficace pour correspondre à l'augmentation des taux d'acquisition de données avec des réductions simultanées des volumes de données. Des essais expérimentaux sur des échantillons contenant des défauts artificiels ont été réalisés pour évaluer l'approche proposée. Les résultats de ce projet incluent trois réalisations significatives : (1) le TFM parcimonieux proposé a réduit de plus de 90% les séquence de tir tout en fournissant une grande précision, et ses performances étaient supérieures à celles de la PWI ; (2) une technique de réseau parcimonieux optimisé pour les sondes matricielles a permis une accélération de 9,8 fois de la TFM en 3D, préservant la qualité de l'image et les capacités de dimensionnement des défauts ; et (3) l'utilisation de CS et des réseaux parcimonieux a permis la récupération du signal ultrasonore à des taux d'échantillonnage inférieurs à la limite de Nyquist et une imagerie TFM plus rapide, indiquant une réduction potentielle de la complexité matérielle des dispositifs à ultrasons pour les applications de CND.

VIII

Study and Implementation of Fast Compressive 3-D Total Focusing Method Ultrasonic Imaging Using 2-D Sparse Arrays

Lucas PEREIRA PIEDADE

ABSTRACT

This thesis explores the increasing focus on three-dimensional imaging in ultrasonic nondestructive testing (NDT), emphasizing the significance of phased array ultrasonic testing (PAUT) and the emerging potential of the total focusing method (TFM) for high-resolution imaging. When applying this method to a 2-D imaging context using linear array probes, limitations arise concerning the identification of defects, particularly in scenarios with random orientations such as cracks, demanding the necessity for 3-D imaging solutions. The study addresses the challenges associated with the use of volumetric imaging in NDT, primarily focusing on matrix phased arrays within the TFM framework, aiming to develop innovative ultrasonic acquisition and data processing strategies to enhance 3-D TFM productivity. The project's scope involves two key facets. Firstly, the project examines the complexity associated with managing a high number of elements in ultrasonic matrix phased arrays, exploring element reduction techniques, notably element selection strategies like sparse arrays. Secondly, the research focuses on methodologies to reduce the substantial data volume generated, investigating innovative data compression techniques, such as compressive sensing (CS) approaches. The integration of these strategies is intended to pave the way for the development of lightweight ultrasonic scanners and to lay the theoretical foundation for their practical realization. Initially, this study introduced a method for designing sparse array layouts applied to linear phased arrays and compared it to the FMC and plane wave imaging (PWI). Then, this sparse array methodology was adapted and extended to matrix phased arrays to optimize data acquisition efficiency while balancing 3-D imaging quality. Finally, the sparse array methodology was combined with an efficient CS framework to match increased data acquisition rates with reductions in the data volumes at the same time. Experimental trials involving samples containing artificial flaws were performed to evaluate the proposed approach. As a result of this project, three significant outcomes were realized: (1) the proposed sparse-TFM reduced firing events by more than 90% while providing high accuracy, and its performance was superior to PWI; (2) an optimized sparse array technique for matrix probes achieved a 9.8-fold acceleration in 3-D TFM, preserving image quality and defect sizing capabilities; and (3) utilizing CS and sparse arrays enabled ultrasonic signal recovery at sampling rates below the Nyquist limit and faster TFM imaging, indicating a potential reduction of the hardware complexity in ultrasound devices for NDT applications.

Keywords: Ultrasonic matrix phased array, sparse array, compressive sensing (CS), total focusing method (TFM), volumetric imaging

TABLE OF CONTENTS

LIST OF TABLES

LIST OF FIGURES

Page

LIST OF ABBREVIATIONS

ADC	Analog-to-digital converter
BP	Beam pattern
CNR	Contrast-to-noise ratio
CR	Compression rate
CS	Compressive sensing
DAS	Delay-and-sum
DCT	Discrete cosine transform
EDM	Electrical discharge machining
FMC	Full matrix capture
GA	Genetic algorithm
GLL	Grating lobe levels
MLW	Main lobe width
NDT	Nondestructive testing
NP	Non-polynomial
PAUT	Phased array ultrasonic testing
PWI	Plane wave imaging
ROI	Region of interest
SA	Simulated annealing
SLL	Sidelobe levels

SNR   Signal-to-noise ratio

SR   Sampling rate

TFM   Total focusing method

TOF   Time of flight

UT   Ultrasonic testing

VOI   Volume of interest

3-D US   3-D ultrasonic imaging

LIST OF SYMBOLS AND UNITS OF MEASUREMENTS

dB	Decibel
E	Young's modulus
e	Emitting element
g_x	Gap length in x-direction
g_y	Gap length in y-direction
H	Hilbert transform
$I(x, z)$	Image intensity in 2-D
$I(x, y, z)$	Image intensity in 3-D
K	Number of non-zero coefficients
l_x	Element width in x-direction
l_y	Element width in y-direction
M	Length of sub-sampled vector
N	Number of linear array elements
N_M	Number of matrix array elements
P	Pixel point
r	Receiving element
s	Sparse vector
S_{er}	A-scan signal from emitting-receiving pair
s_x	Pitch in x-direction

s_y	Pitch in y-direction
V	Wave propagation velocity
V_L	Longitudinal wave propagation velocity
V_s	Shear wave propagation velocity
x	Signal
y	Compressive measurement vector
Z	Acoustic impedance
Θ	Sensing matrix
θ_i	Incident angle
θ_{rl}	Refraction angle of longitudinal wave
θ_{rs}	Refraction angle of shear wave
λ	Wavelength
v	Poisson ratio
ρ	Medium density
Ψ	Basis matrix or transform basis
Φ	Measurement matrix

INTRODUCTION

Nondestructive testing (NDT) using ultrasonic methods has long been instrumental in the detection and characterization of flaws within engineering structures. The ability to assess the integrity of materials without causing any damage is an interesting tool in ensuring the safety and reliability of various industrial components, ranging from pipelines to aerospace structures. In this field, ultrasonic NDT plays an important role in identifying and evaluating defects, ensuring structural stability, and mitigating potential risks associated with material failures.

Over the past few decades, phased array ultrasonic testing (PAUT) has emerged as a prominant technique in NDT due to its unparalleled advantages over traditional ultrasonic testing (UT) such as reliability and flexible inspection capabilities. Multi-element probes, unlike conventional ultrasonic probes with a single active element, consist of an array of elements that can be controlled independently. This feature enables directing the incident ultrasonic field in a particular direction or measuring the reflected field simultaneously at multiple points. Consequently, associated imaging algorithms, digital signal processing, and control units have also been subject to extensive development and research. In particular, the total focusing method (TFM) algorithm has recently been gaining popularity due to its capacity to produce high-resolution images of the inspected medium. When applied to linear phased array probes, TFM generates 2-D images by synthetically focusing the array on every pixel, being a powerful tool regarding detecting and sizing flaws. Nonetheless, in some situations, the identification of defects is limited e.g. the random orientation of cracks. In this case, a 3-D image would be desirable to enable better insonification and identification of defects.

To generate volumetric images, a matrix phased array transducer also known as a 2-D phased array can be used. The arrangement of elements in a 2-D array enables the steering of the ultrasonic beam throughout space but also increases the number of piezoelectric elements to square power compared to linear probes. For instance, the equivalent in 2-D of a 1-D probe with

32 elements contains 1024 elements. Despite the immense potential and advantages offered by matrix phased arrays in ultrasonic imaging, their widespread adoption in industrial NDT applications remains constrained compared to their linear array counterparts. This limited utilization primarily arises from significant technical challenges, notably the complexities associated with connecting and driving the high number of elements, as well as the substantial hardware demands required for handling the vast amount of generated data essential for 3-D imaging.

This study addresses the growing interest in three-dimensional ultrasonic imaging within the NDT field, particularly concerning the challenges associated with matrix phased arrays in the TFM framework. Evident Industrial, previously known as Olympus NDT Canada, is the industrial collaborator in this project. The company specializes in designing inspection equipment as well as their integration into industrial settings. Volumetric imaging in real-time is an interesting and attractive modality of ultrasound inspection, as it provides more realistic representations of the defects within short inspection times. Today, this fast processing is restricted to the usage of high-end instruments, and thus, for various applications, the expense of high-end equipment is often not justifiable. In the coming years, advancements are anticipated to overcome volumetric imaging limitations in heavy hardware scanners, leading to increased availability at reduced costs. Presently, high-channel-count ultrasonic scanners are limited to fewer research facilities, and the transition toward more cost-efficient systems is still pending. Other research streams are focusing on the development of lighter hardware scanners that can deliver comparable performance to complex systems with fewer array elements. Therefore, the objective of this research focuses on the development of new ultrasonic acquisition and data processing strategies, based on the TFM method, applied to ultrasonic matrix phased arrays. The aim is to enhance 3-D TFM productivity and to enable the routine use of 2-D arrays.

This research project can, therefore, be divided into two major parts. The first one is related to the complexity associated with managing a high number of elements within ultrasonic matrix phased arrays. This segment of the research project concentrates on addressing this challenge through the exploration of element number reduction techniques. The primary objective is to determine feasible tradeoffs between the probe's active element count during transmission and its acoustic performance concerning a full array configuration. An efficient and cost-effective avenue to tackle this challenge involves the utilization of element selection strategies, prominently among them being the application of sparse arrays. Sparse arrays offer a promising solution not only to reduce acquisition times but also to mitigate the volume of data necessitated by 3-D TFM processing. These arrays strategically employ a subset of active elements within the overall array, thereby optimizing the balance between imaging quality and data acquisition efficiency. The second part is regarding the management of the huge volume of data generated during ultrasonic inspections, particularly from denser probes, which poses a significant industrial challenge. Transmitting, storing, and processing data from numerous inspections becomes increasingly arduous, demanding more sophisticated strategies to alleviate the data burden on inspection systems. This segment of the research project centers on investigating methodologies aimed at reducing the size of generated data required for volumetric imaging. Efforts are directed toward exploring innovative data compression techniques. In this context, emerging methods such as compressive sensing (CS) have gained considerable attention due to their potential efficiency in data compression. Unlike conventional compression methods found in contemporary devices, CS presents a promising alternative by exploiting the intrinsic sparsity of ultrasonic signals, allowing for efficient data reconstruction from significantly reduced datasets. Hence, the combination of these strategies should enable the development of lightweight scanners or, at the very least, offer the theoretical groundwork for their practical realization.

Therefore, the work conducted in this thesis was aimed to address these issues. The first chapter will offer a comprehensive review of the literature on the topic. The subsequent three chapters

will cover the published and submitted articles. Lastly, conclusions are drawn in the final chapter, supplemented by an appendix housing supplementary results for reference.

CHAPTER 1

LITERATURE REVIEW

This chapter presents the literature review of general ultrasonic science to gather several concepts related to ultrasonic testing, ultrasonic phased arrays, advanced imaging, and the integration of sparse arrays with compressive sensing (CS) for ultrasound inspection. It aims to provide essential concepts for understanding the research topic and present the current state of research on the subject.

1.1   Ultrasound inspection: from conventional to multi-element transducers

To understand the implications of using denser probes, this section provides a concise explanation of the operation of conventional and multi-element transducers. Additionally, it introduces the fundamental principles of ultrasound wave generation and propagation pertinent to this project.

1.1.1   Ultrasonic testing (UT) principles and physics

Ultrasonic science is a specific branch of acoustics that studies the energy-matter interactions, effects of propagation, and the applications of ultrasonic waves. This particular sound wave is a mechanical vibratory wave (stress wave) that propagates only through the matter (solid, liquid, and gases) with frequencies above the human hearing range (typically above 20 kHz), and that can be found applied in almost every field of engineering, medicine, and sciences in general (Ensminger & Bond, 2011). Nondestructive testing (NDT) groups together are often applied for the detection and characterization of defects in engineering components.

Ultrasonic testing (UT) belongs to the group of NDT techniques and is a method based on the propagation of ultrasonic waves. UT became a widespread technique for medical and industrial applications mainly because it represents an economic and safer approach (non-hazardous to operator and vicinity) regarding the assessment of the internal conditions of objects when compared to methods like radiography, which require more than one type of protection (Halmshaw, 1997). In industrial applications, UT has been used to detect all kinds of flaws

that materials like metals, ceramics, plastics, and composites might have, as well as to analyze the material properties and to measure thickness. During a UT inspection, ultrasonic waves are induced in an elastic medium (test piece) by using an ultrasonic transducer (probe) and propagate through the specimen under analysis (Olympus, 2004). When propagating through the medium and interacting with heterogeneities, some energy of the propagating wave is reflected. In this case, the back wall of the specimen will also reflect the wave. The so-called echoes (back-propagated waves) are then used to indicate which component from the test piece caused the reflection. These ultrasonic waves are typically generated by a piezoelectric material inside the probe excited by an electrical voltage. The opposite effect also exists for this material, converting ultrasound into electrical signals. The frequency range of ultrasonic waves is usually 0.1 MHz to 50 MHz but for most industrial applications this range is limited to between 0.5 MHZ and 15 MHz (Olympus, 2004). Applying an electric voltage makes the piezoelectric crystals change in shape and size, oscillating at the same frequency as they were excited and thus producing ultrasonic waves. Figure 1.1 depicts an example of a classic UT inspection of a solid sample containing a flaw. The probe generates a traveling wave, which is then captured as it interacts with a spherical reflector. The same probe is shown receiving the scattered waves from the reflector, demonstrating the dual role of the transducer in both wave generation and reception to subsequent data interpretation using a time amplitude representation.
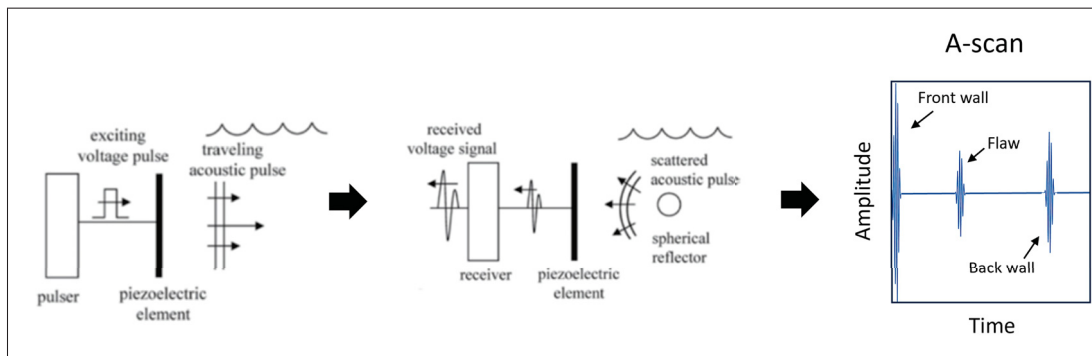
Figure 1.1   Schematic representation of a UT inspection and resulting time amplitude diagram (A-scan)
Adapted from Schmerr Jr (2014, p. 2)

For a classical UT measurement, monocrystal probes are usually used to generate and receive the mechanical pulses (Olympus, 2004). The echoes from the features converted into electrical signals are plotted in a graph of amplitude as a function of time known as A-scan (Figure 1.1). As the information about the intensity and arrival delay of the wave is contained in the diagram, it is possible to estimate the position of each feature based on the sound velocity of the test material and the known equation of motion from physics i.e. distance equals to velocity times the time interval. Therefore, this technique can be used not only for the detection of discontinuities contained in a part but also to estimate its position.

The physics related to ultrasonic testing involves mechanical wave propagation and the associated phenomena. By definition, a mechanical wave is a disturbance that travels through a medium, causing an oscillatory movement of particles that compose it. The oscillatory movement produces a wave that propagates at a certain propagation velocity. The particles can be picturized as elements connected through elastic springs, so their motion is influenced by the nearest neighboring motion (Ensminger & Bond, 2011). Thus, its velocity is dependent on the elastic properties of the medium as well as the nature of the excitation. The elastic waves that propagate through solids are known as bulk waves, the wave type that is the key focus of this work. These waves are divided into two types: longitudinal waves or pressure waves, and shear waves, also called transverse waves. The longitudinal and shear waves can be distinguished by their displacement direction. Longitudinal wave displacements are parallel to the propagation direction whereas shear wave displacements are perpendicular to the propagation direction. Furthermore, shear waves only propagate in solid bodies (Cheeke, 2012). Each wave has its wave propagation velocity: V_L for longitudinal waves and V_s for shear waves. The respective equations are the following for a homogeneous and isotropic solid (Cheeke, 2012):

$$V_L = \left[\frac{E(1-v)}{\rho(1+v)(1-2v)} \right]^{1/2},$$

(1.1)

$$V_s = \left[\frac{E}{2\rho(1+v)} \right]^{1/2}$$

(1.2)

where E is the Young's modulus, ρ, and v are the density and the Poisson ratio of the medium, respectively.

Ultrasound can be considered in many aspects analogous to electromagnetic waves or even light by the fact that it follows the general wave equation and wave motion (Ensminger & Bond, 2011). Regarding the light analogy, ultrasound can be reflected at surfaces, refracted when changing the medium, and diffracted around different obstructions, surfaces, or edges (Ensminger & Bond, 2011). When an ultrasound wave hits a boundary between two different materials, part of the incident energy will be reflected, and at the same time, the rest is transmitted into the material. In this case, Snell-Descartes law applies to the refraction at oblique wave incidence:

$$\frac{\sin \theta_i}{V_i} = \frac{\sin \theta_{rl}}{V_{rl}} = \frac{\sin \theta_{rs}}{V_{rs}} \qquad (1.3)$$

where θ_i is the incident angle, θ_{rl}, and θ_{rs} are the refraction angles of longitudinal wave and shear wave, respectively with their respective velocities V_i, V_{rl}, and V_{rs}. Figure 1.2 shows the interactions of the incident mechanical wave in a solid interface using a probe coupled to a wedge in an angle beam assembly. A mode conversion occurs at a boundary, denoted by the axis dashed line, resulting in refracted shear and longitudinal waves within the test piece. The figure includes the incident and refracted angles, accompanied by the corresponding shear and longitudinal wave displacements.

The property of acoustic impedance (Z) also governs the mechanism of wave reflection. This physical property describes the opposition that the ultrasound energy encounters as it passes through different mediums (Cheeke, 2012). Therefore, the propagation of an ultrasound wave from one medium to another relies on the difference in acoustic impedance between them. The acoustic impedance is then defined as the product of the medium density (ρ) and wave propagation velocity (V):

$$Z = \rho V. \qquad (1.4)$$
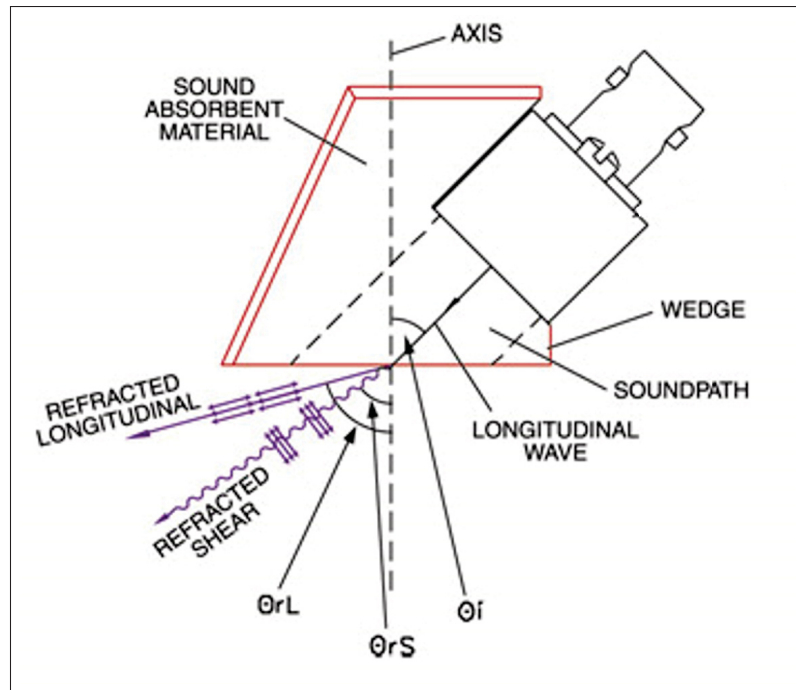
Figure 1.2   Interactions of the incident mechanical
wave in a solid interface using a wedge
Adapted from Olympus (2004, p. 126)

Thus, it is possible to quantify the amount of energy reflected and transmitted from the acoustic impedance of the two materials. A piece of more detailed information on this subject can be found in the literature of Cheeke (2012). The interactions at the boundary of two mediums and the refraction of ultrasound waves into longitudinal and transverse modes are crucial for defect detection and ultrasound imaging. This will be explained further in the following sections.

1.1.2   Phased array ultrasonic testing (PAUT)

In the last 30 years, the development of electronics resulted in an expansion of ultrasonic phased array systems in both medical ultrasound and NDT fields (Ensminger & Bond, 2011). Unlike the conventional single-element ultrasonic transducer described in section 1.1.1, the ultrasonic phased array probes consist of a single transducer containing several small individual elements that can be independently pulsed. This represents two benefits of the phased array ultrasonic testing (PAUT) over the traditional UT: (1) flexibility, as it becomes possible to make

a range of different inspections from a single location, and (2) easier interpretation of the results (Drinkwater & Wilcox, 2006; Felice & Fan, 2018). Phased array transducers contain 16 up to 256 elements, as 256 usually represents the maximum number of elements that can be connected and simultaneously driven by NDT transmit–receiver instruments (Drinkwater & Wilcox, 2006). However, certain transducers exhibit a notably higher element count, such as the 1024-element matrix array transducer (32 x 32). Operating such arrays may necessitate techniques like multiplexing, synchronization of multiple acquisition systems to accommodate the 1024 channels, or the use of expensive high-channel-count systems. The ability to modify the beam parameters via software such as angle and focal spot size increases the possibility of detecting randomly oriented defects like cracks, which single-element probes might miss when not perfectly aligned (Olympus, 2004). As a result, this technology allows for the reduction of errors and operator's dependence, increasing the reliability and quality of the inspection.

The term "phased array" comes from the multiple piezoelectric elements placed in an array pattern that can be phased in time to generate ultrasonic waves, scanning the medium. It is possible to perform a variety of inspections by controlling each element and thus generate different types and patterns of the ultrasonic wave. The ability to steer and focus at different depths and directions is one of the main features of ultrasonic phased arrays. Figure 1.3 illustrates the phased beam generation as well as the delays applied to steer the generated sound beam. To generate the phased beam with constructive interference, the acquisition unit sends a trigger signal to the phased array unit, which converts the signal into a high-voltage pulse with the defined delay law (Olympus, 2004). Then, each element of the array that received only one pulse becomes a point source and sends a cylindrical wave into the medium. The cylindrical waves are combined and form a wavefront upon interaction with a flaw is reflected. The echoes received into the phased array unit are time-shifted according to the focal law. After, they are summed and form a single signal that is sent to the acquisition unit. By changing the time delays, the phased array is able to steer the beam in different directions without any movement of the transducer.
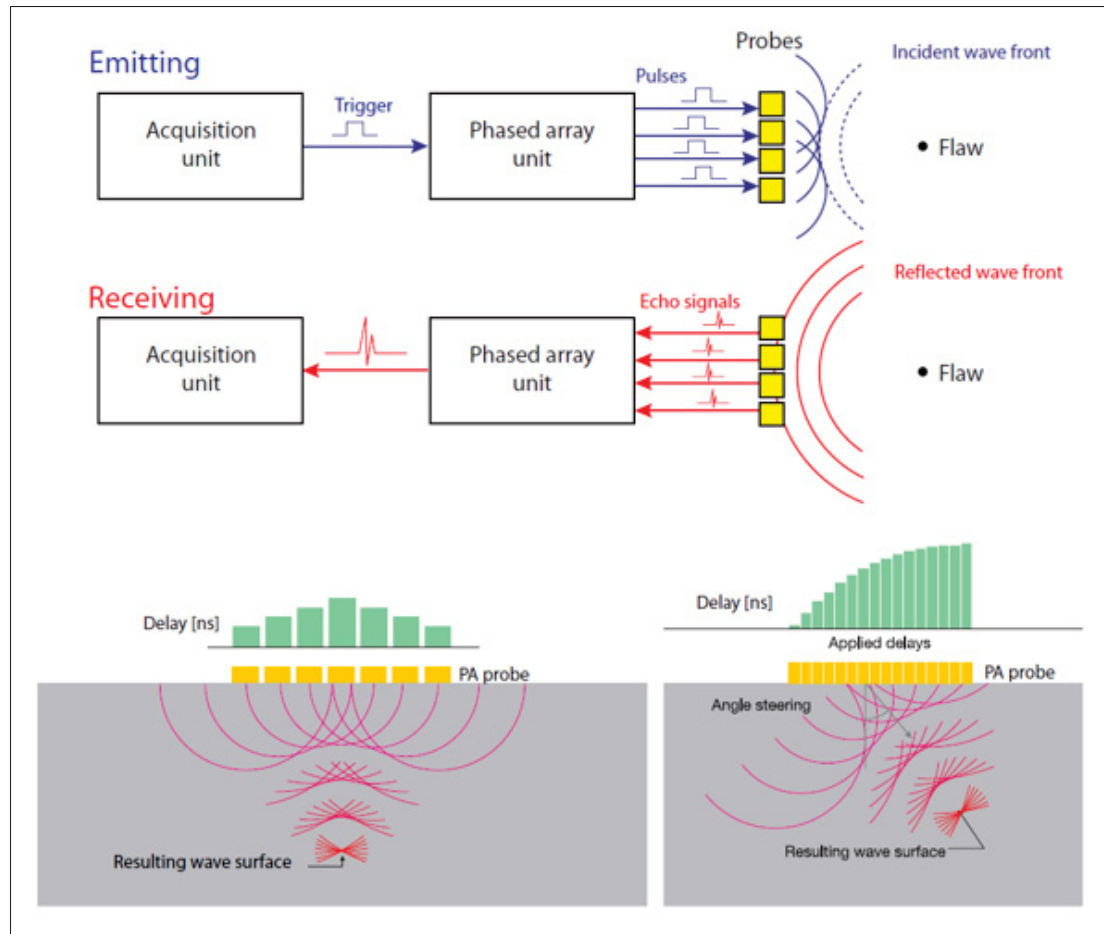
Figure 1.3   Beam forming and time delays of an ultrasonic phased array
Adapted from Olympus (2004, p. 11)

Different types of ultrasonic transducers can be used in industrial applications: one-dimensional (1-D), two-dimensional (2-D), or annular (Drinkwater & Wilcox, 2006). The 1-D linear array probe is by far the most common in the industry, mainly because its manufacturing is economically advantageous (Schmerr Jr, 2014). The elements of this probe have a rectangular shape and are placed next to each other along the x-direction in Figure 1.4. In the case of Figure 1.4, the elements are distributed along the x-direction with the length l_x smaller than the length l_y in the y-direction (passive aperture).

The elements are equally spaced in the x-direction with a specific gap length (g_x) also named kerf. The pitch (s_x) is the distance between the beginning of elements, which is given by the
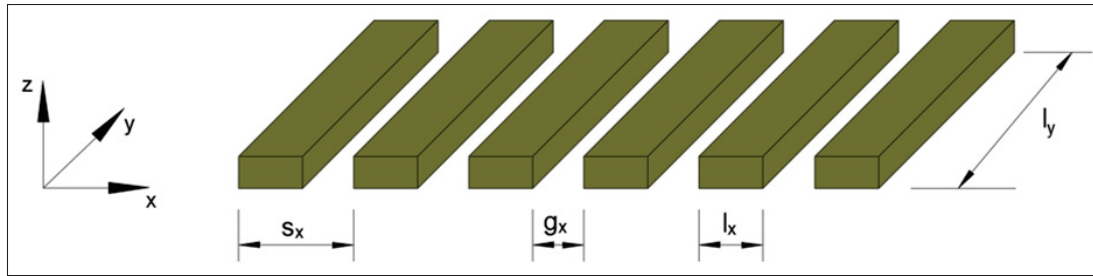
Figure 1.4   The elements and parameters of a linear array

sum of gap length g_x and element width l_x, and is an important parameter of the probe. In order to synthesize a wave field free of unwanted grating lobes, the element width l_x must be less than half a wavelength (λ) (Schmerr Jr, 2014). Furthermore, it is also recommended as a design rule to have a pitch smaller than 67% of lambda (Olympus, 2004). The total active probe length is named the active aperture and plays an important role in the beam-diffracted pattern and the beam width. Using ultrasonic phased array technology, it is possible to steer the beam in a region beyond the area below the probe (active aperture), and this capacity relies on these design parameters.

1.1.3   Matrix phased array (2-D array)

A matrix phased array or 2-D phased array has the potential to image in three dimensions. The ability of steering and focusing in 3 dimensions increases the set of angles and extends the coverage to a volumetric area, all this from a single probe position of the part inspected. This is an advantageous feature as real defects of engineering structures are three-dimensional, having an arbitrary shape and orientation. Defects like cracks and inclusions are examples of these types of flaws that, in some cases, may have a limited assessment using linear arrays. Regarding the measurement of discontinuities within a medium, a full 3-D image represents a better possibility of assessing the specific medical or engineering issue. Even though the matrix array has greater notoriety in the medical field, this technology is not yet widespread in NDT industrial applications (Drinkwater & Wilcox, 2006).

The first 2-D images were obtained using a single-element probe that was moved manually or by mechanical means. The 3-D image generation first happened in the same way but with the linear 1-D probe. To generate the 3-D ultrasonic images (3-D US) using a linear probe, experiments using position-tracked (Hughes *et al.*, 1996; Levine *et al.*, 1989) or motorized devices that applied rotations (Downey, Nicolle, Levin & Fenster, 1996; Nikolov, Jensen, Dufait & Schoisswohl, 2002) and translations (Dabrowski, Dunmore-Buyze, Cardinal & Fenster, 2001) or tilt of the probe (Gilja *et al.*, 1995) were done to inspect the entire volume. But in fact, the introduction of 1.25 D, 1.5D, and 1.75 D arrays enabled the development of the 2-D probes (Fernandez *et al.*, 2003; Wildes *et al.*, 1997). This represented a significant advance over the linear 1-D probe, considering some limitations related to this process and that moving the probe is a time-consuming procedure. Mono-element and one-dimensional ultrasonic phased array probes lack the focusing and steering abilities in different dimensions, which increases the probability of not detecting randomly oriented flaws. For measurements where the orientation of those flaws cannot be previously predicted, it is necessary to conduct a wider set of acquisitions at different orientations to avoid losing information (McKee *et al.*, 2019), which is impractical in reality.

On the other hand, matrix array probes differ from conventional linear probes as they extend in the elevation direction, creating a 2-D pattern of elements. Thanks to this feature, it is possible to focus and steer the beam in many ways, as the time delays can vary in both the x- and y-directions (Schmerr Jr, 2014). As a result, the entire volume is better inspected, providing a detailed view without moving the probe. Another consequence of this extension is the rising number of elements to the square power when compared to the linear probe, which also increases its sensitivity and the already cited focusing and steering capability. For instance, the equivalent in 2-D of a 1-D probe containing 32 elements would have 1024 elements. Figure 1.5 depicts examples of the linear and the 2-D matrix, showing the difference between the piezoelectric elements.

In a square matrix array probe, all the elements are lined up on a uniform grid, spaced out at the same distance (pitch) in both x- and y-directions. Like the linear phased array, the matrix probe design must follow the same pitch designing rules mentioned in section 1.1.2 to avoid the
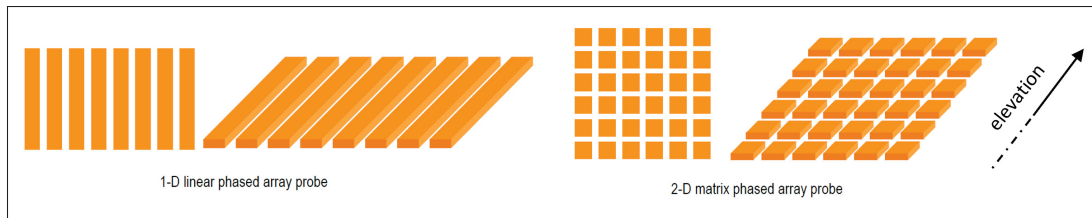
Figure 1.5   Typical ultrasonic phased array probes
Adapted from Olympus (2004, p. 103)

presence of grating lobes. These lobes are the spatial aliasing effect that causes some sidelobes to become considerably larger in amplitude, approaching the level of the main lobe where most of the ultrasonic energy is concentrated. Features like sidelobe levels (SLL), and grating lobe levels (GLL), along with the main lobe width (MLW) are linked to the 2-D image quality and must be considered to generate a satisfactory image in terms of resolution and contrast (Roux *et al.*, 2017). Figure 1.6 portrays an example of a two-dimensional array with elements of lengths l_x and l_y. The typical grid for 2-D arrays is either rectangular or square, where l_x and l_y will be the same in the latter case. The square element matrix probe in this case can be considered a clear extension of the linear probe, and as a consequence, is easier to model.
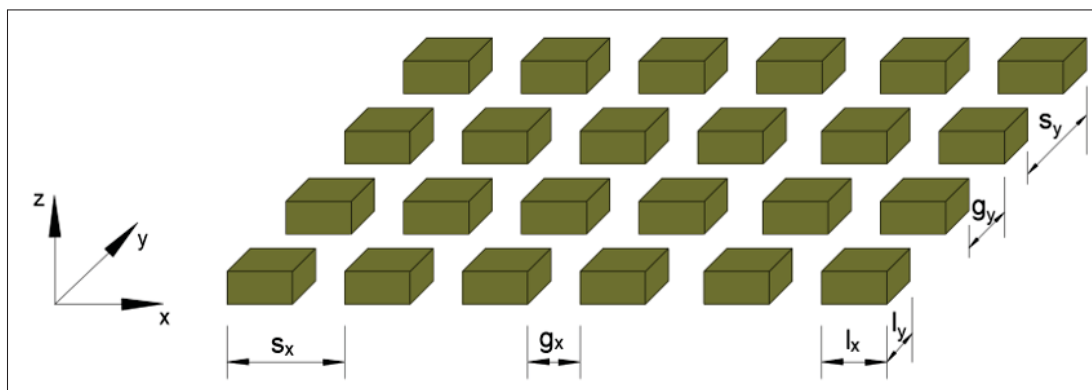
Figure 1.6   Parameters of a matrix array composed of square elements

Owing to the matrix array probe features, three-dimensional beam scanning and focusing can be done, which opens new possibilities towards NDT inspections. The potential to focus the beam at different depths in spherical, elliptical, or linear patterns as well as the capability to steer the ultrasonic beam in more than one plane can be accounted as the main advantages of this

technology (Olympus, 2004). Although 2-D array probes offer significant inspection potential, their adoption in industrial NDT applications has been limited compared to linear probes. This is primarily due to the complexity of managing a large number of elements and challenges in manufacturing denser probes. In the context of volumetric imaging and acquisition, there are additional limitations that prevent the broader adoption of this technology, which will be addressed in more detail. Various imaging techniques and data acquisitions have been suggested for industrial applications using ultrasonic phased arrays in the literature. The most pertinent for this study will be discussed in the following sections.

1.2 Scanning and advanced imaging methods

The expansion and development of ultrasonic phased array systems that enable both transmission and reception from all elements also led to the advancement of different acquisition strategies and imaging algorithms. In this section, the full matrix capture (FMC) acquisition and the total focusing method (TFM) are introduced and extended to the context of ultrasonic three-dimensional imaging. The operation of 3-D US TFM will be the research focus of this study. This literature review will also explore potential alternatives to make this approach practical for NDT industrial applications and to promote the broader use of volumetric imaging employing ultrasonic matrix phased array transducers.

1.2.1 Full matrix capture (FMC)

Multichannel acquisition methods are gaining popularity for their ability to enable high-resolution imaging by processing signals from ultrasonic phased array probes. Notably, FMC is becoming widely used due to its versatility, as it consists of collecting all the transmitter-receiver combinations. FMC measurement is made by transmitting sequentially one element at a time and recording all elements from the array. The first element fires the wave inside the part and the backpropagated wave is received by all elements, followed by the firing of the second element, and so on. Therefore, an array containing N elements realizes N emissions with N reception channels in each event, generating an $N \times N$ matrix of A-scans (FMC matrix).

Although the FMC store and process a huge amount of data, the advantage of acquiring all the information that any other method might obtain is the counterbalance of this technique. For a better understanding, Figure 1.7 illustrates the FMC sequence for a linear array containing N elements. The active elements in transmission and reception are colored while deactivated elements are shown in white.
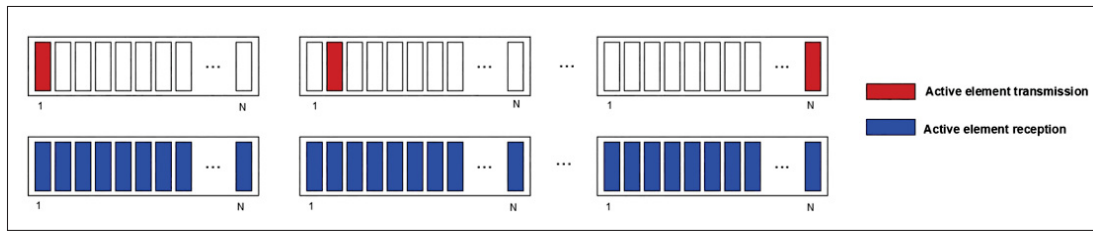
Figure 1.7   Full matrix capture representation

After its introduction by Holmes, Drinkwater & Wilcox (2005), the FMC method gained widespread acceptance, and currently, most commercial ultrasonic array controllers offer support for FMC acquisition. Following FMC acquisition, it is possible to insert delays synthetically to the acquired A-scan data in post-processing. This capability allows for the application of different post-processing techniques to create subsurface images of engineering components, including the implementation of linear time delays for plane wave imaging (PWI) (Le Jeune, Robert, Lopez Villaverde & Prada, 2016), or creating virtual sources by introducing delays to sub-apertures of the array (Hoyle, Sutcliffe, Charlton & Rees, 2018). Nonetheless, these techniques are variations of one notorious and commonly used delay-and-sum (DAS) algorithm, known as the total focusing method (TFM).

1.2.2   Total focusing method (TFM)

TFM imaging consists of applying delay functions to signals from an ultrasonic phased array to enable focusing on a specific region, enhancing local sensitivity and thereby increasing flaw detectability (Holmes *et al.*, 2005). This delay-and-sum algorithm receives the name of "total focusing" by synthetically focusing the array on each image pixel in the x-z plane. It is considered the gold standard in array imaging by generating the highest possible imaging

resolution from the interior regions of the part under inspection based on FMC information (Fan, Caleap, Pan & Drinkwater, 2014). TFM is today beginning to be diversely used in industrial applications (Lane, Dunhill, Drinkwater & Wilcox, 2010; Li, Pain, Wilcox & Drinkwater, 2013; Russell, Long, Duxbury & Cawley, 2012). The combination of FMC-TFM is also currently found available in most commercial ultrasound systems. Figure 1.8 depicts the TFM algorithm operation applied to a linear array containing N elements.
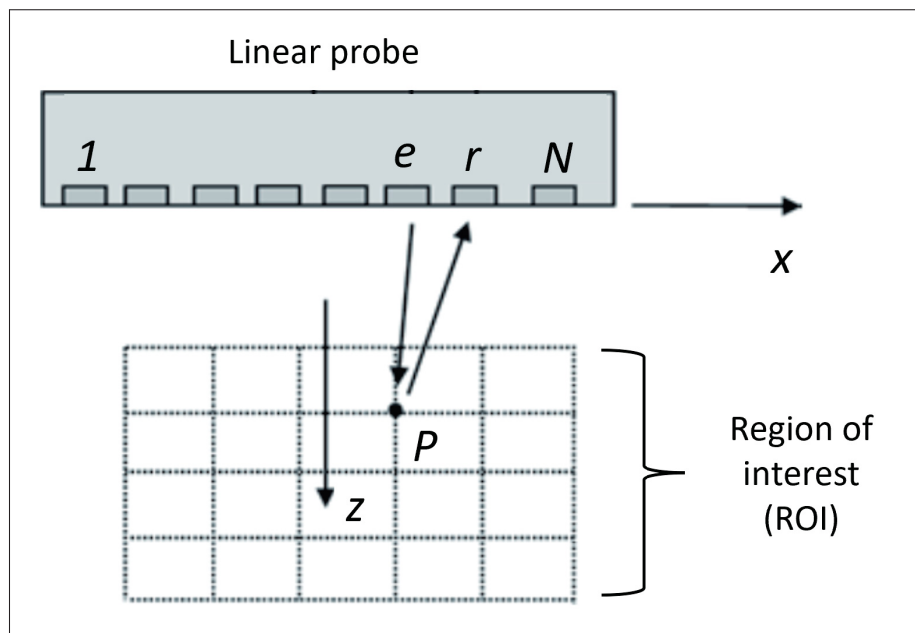
Figure 1.8   TFM imaging procedure using a linear transducer,
where the travel times to an image point P are computed for
different combinations of e and r
Adapted from Schmerr Jr (2014, p. 244)

First, the technique divides the region of interest (ROI) into a grid of pixels. Then, it calculates the distances between the emitting element (e) to a given pixel (P), and from the same pixel to a receiving element (r) to later compute the time of flight (TOF) using the wave propagation velocity. Thus, the image intensity $I(x, z)$ is given by a summation of each pixel intensity obtained by the time-domain amplitude of the signal at the computed TOF (Sutcliffe, Weston, Dutton, Charlton & Donne, 2012):

$$I(x, z) = \left| \sum_{e=1}^{N} \sum_{r=1}^{N} H\left(S_{er}\left(TOF\left(x, z\right)\right)\right) \right| \tag{1.5}$$

where H is the Hilbert transform and S_{er} denotes the time-amplitude signal from the corresponding emitting-receiving pair. By positioning the elements along one dimension ($x-$direction), the linear phased array can only steer in the x-z plane, therefore producing 2-D images from a single probe position. Hence, the result is a fully focused high-resolution 2-D image. Holmes *et al.* (2005) successfully applied the TFM approach for NDT applications in post-processing after a full matrix capture. The authors measured an aluminum block containing electrical discharge machining (EDM) notches as defects using the FMC-TFM strategy, and their results showed that the performance in signal-to-noise ratio (SNR) was better than the plane and focused B-scans. The SNR measures the ratio of the power of a signal to the power of background noise, and therefore a greater SNR indicates more signal than noise.

Matrix phased arrays can perform 3-D imaging thanks to their 2-D element arrangement, and therefore, it is possible to implement the concept of collecting and processing the FMC to generate accurate 3-D images using the TFM algorithm. The 3-D TFM precisely produces a volumetric image without stacking or stretching the two-dimensional planes. The region of interest now extends to an additional plane and is converted into a 3-D grid of pixels named volume of interest (VOI) instead of "region of interest", as described for 2-D TFM. Figure 1.9 shows the 3-D TFM imaging process for a square matrix array of N_M elements.

Likewise 2-D TFM imaging algorithm, the distances between the centroid of e to a given pixel P located in a cubic grid, and from the same pixel to the centroid of r are computed, then obtaining the TOF according to the wave propagation velocity in the medium. The image intensity $I(x, y, z)$ of a 2-D array that contains N_M elements is given by:

$$I(x, y, z) = \left| \sum_{e=1}^{N_M} \sum_{r=1}^{N_M} H\left(S_{er}\left(TOF\left(x, y, z\right)\right)\right) \right|. \tag{1.6}$$
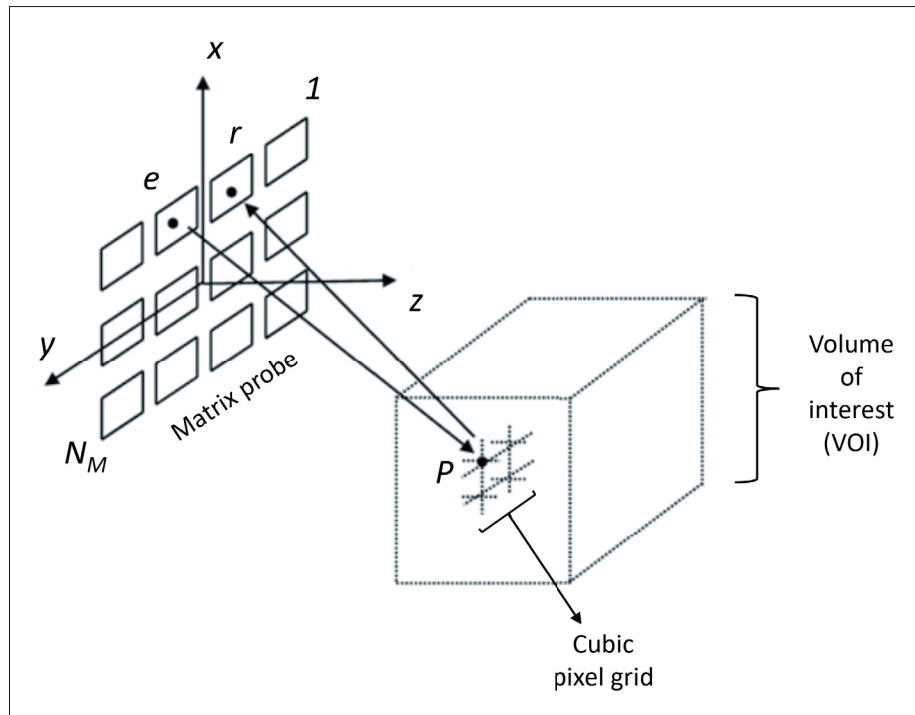
Figure 1.9   3-D TFM imaging process using a square matrix
array
Adapted from Schmerr Jr (2014, p. 245)

The result of the FMC-TFM applied to a matrix phased array can be seen in Figure 1.10. The three-dimensional view of the defects inside the part as well as the 2-D planes can be plotted, showing the potential of this technology regarding sizing randomly oriented flaws. Information about the length, depth, and orientation are displayed in the images, all this is accomplished by inspecting from a single point location.

In this case, one can see that using TFM for volumetric imaging requires significantly more computational power than its 2-D counterpart, as indicated by comparing Eqs.1.6 and 1.5. This is due to the larger amount of data involved in 3-D imaging, as matrix arrays have many more elements compared to linear arrays ($N_M >> N$). For instance, a denser matrix probe with 1024 elements (32 x 32 array) would produce a 1024 x 1024 matrix of A-scans. This is equivalent to the square of the number of A-scans collected by a 1-D probe with 32 elements using FMC.
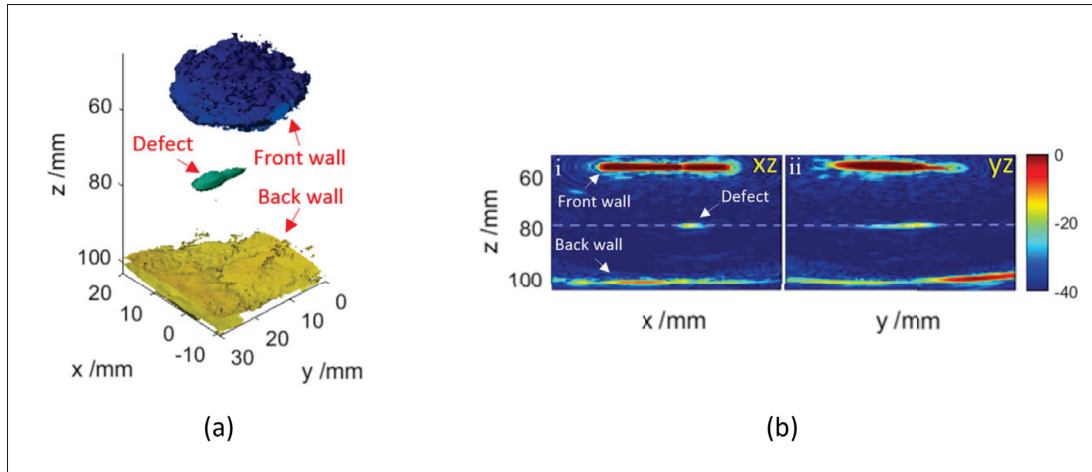
Figure 1.10   Reconstructed image of a defect: (a) 3-D TFM and (b) XZ and
YZ planes
Adapted from McKee *et al.* (2019, p. 6)

Also, the number of focal points in a 3-D image is much higher than in a 2-D image, which slows down the image formation process as well.

1.3   Concept and design of sparse arrays

Despite all the benefits and potential of ultrasonic matrix phased arrays, the broad use of this technology in industrial NDT applications has not been accomplished yet, especially when compared to the linear array (Drinkwater & Wilcox, 2006). The main reasons for this very little take-up stem from the following problems: (1) managing and driving a high number of elements is a technical challenge; (2) 3-D imaging requires a high hardware complexity to handle the large amount of generated data. In this way, different strategies have been suggested to overcome these limitations. It is expected that within the next years heavy hardware scanners that overcome these limitations will become more widespread and significantly cheaper. So far, large channel count ultrasonic scanners are restricted to a few research centers, to cite the systems in Denmark (Jensen *et al.*, 2013), France (Petrusca *et al.*, 2018), and from Provost *et al.* (2015). On the other hand, future directions are pointing to the implementation of lighter hardware scanners that could perform similarly to complex systems but using a reduced number of elements (Roux *et al.*,

2018). Approaches to designing and driving 2-D phased arrays are being explored, especially the ones that consider element number reduction, such as the sparse array (Austeng & Holm, 2002). This technique selects a reduced set of elements inside the matrix probe, allowing it to preserve fewer active elements without losing too much performance. In addition, the productivity of the 3-D TFM could be increased by using this method. One can notice that adopting this imaging algorithm using denser probes overloads both the TFM acquisition and computation time. This is a consequence of the time interval from consecutive firings events of the FMC acquisition combined with the time-consuming TFM computation related to the vast amount of FMC data generated, which limits its use in real-time measurements without high-end devices. Therefore, using a lower number of firing events would improve acquisition speed and reduce the data to be processed. Working with a sparse array corresponds to using a sparsely populated array in transmission, in which reception can be done whether in all elements or just using a couple of them (Bannouf, Robert, Casula & Prada, 2013; Moreau, Drinkwater & Wilcox, 2009).

Finding the ideal sparse configuration can be based on two well-established paths identified in previous works (Austeng & Holm, 2002; Roux *et al.*, 2017), even though none of them can be considered definitive: deterministic and non-deterministic approaches. Most of these approaches are based on narrowband array beam pattern (BP) simulations to reduce the computational load, as computing a realistic BP is a time-consuming and resource-heavy operation. Examples of deterministic approaches are regular and radially periodic arrays (Austeng & Holm, 2002; Brunke & Lockwood, 1997), and conformational arrays (Ramadas, Jackson, Dziewierz, O'Leary & Gachagan, 2014). The latest works are dealing with different spiral array configurations (Martínez-Graullera *et al.*, 2010; Ramalli, Boni, Savoia & Tortoli, 2015; Yoon & Song, 2020). When using the deterministic approach, knowing the layout geometry in advance allows a quick definition of the sparse array without greater computational work, and to perform simulation tests right after. However, depending on the approach used, the design flexibility is limited in this case, and its performance dependency on the set elements in transmission and reception is also an obstacle (Roux *et al.*, 2017). Figure 1.11 shows examples of regular, radially, and spiral periodic array layouts. The black dots represent the active elements.
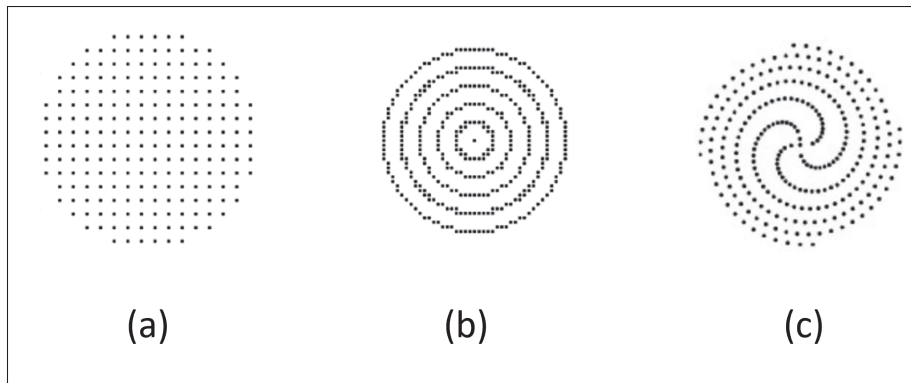
Figure 1.11   Periodic array layouts (a) regular, (b) radially
used by Austeng & Holm (2002), and (c) spiral proposed by
Martínez-Graullera *et al.* (2010)
Adapted from Austeng & Holm (2002, p. 1077) and
Martínez-Graullera *et al.* (2010, p. 281)

The non-deterministic random sparse array approach usually uses a predefined number of array configurations, where each one is obtained by randomly selecting the reduced desired number of active elements from the array. In this case, the configuration with the best performance is selected e.g. lowest side lobe level. Still, the reliability of the best configuration is limited by the fact that each random sparse array is independently made from the previously evaluated configuration and the narrow number of explorations (Roux *et al.*, 2017). On the other hand, non-deterministic approaches based on stochastic optimization consider these previously evaluated configurations and iteratively explore the best configuration. For cases like this, the simulated annealing (SA) algorithm has shown to be a better option over other stochastic approaches such as genetic algorithms (GA), which require more time and computation robustness, in addition to premature convergence in some cases (Adler, 1993; Hwang & He, 2006). Stochastic optimization, when compared to the "classical" non-deterministic random approach, has the advantage of controlling the process time duration (finite-time convergence property) and the convergence property to the global minimum (Roux *et al.*, 2018). Trucco (1999) was the first to apply SA to large 2-D sparse arrays, and since then this algorithm has been refined (Diarra, Liebgott, Tortoli & Cachard, 2011; Diarra, Liebgott, Robini, Tortoli & Cachard, 2012; Roux *et al.*, 2017).

The latest studies regarding volumetric imaging using sparse arrays were performed using a wideband array BP, which provides a more realistic analysis but requires increased computational resources (Sciallero & Trucco, 2015; Roux *et al.*, 2016). Typically, stochastic optimization methods are used to create wideband sparse arrays, with the SA algorithm being a popular choice for this purpose. In the work of Roux *et al.* (2018), 3-D US images were compared using three distinct array configurations. From a reduced number of 256 elements out of the reference array containing 1024, the authors design the best 2-D sparse array configuration based on wideband signals using the SA algorithm, comparing the echocardiography phantom images with the full reference array and a random layout of 256 elements. According to the results, the random selection performed better than the other scenarios in terms of lateral resolution using diverging waves. At the same time, the optimal layout based on SA presented a contrast-to-noise ratio (CNR) around just 4 dB worse than the full reference array, and 0.6 dB better than the random. For future directions, the authors suggest reducing the number of active elements down to 7% of the reference array. Figure 1.12 illustrates the 2-D phased array layouts used, and their respective 3-D phantom image slices containing the CNR values.

Recently, Sciallero & Trucco (2021) introduced a novel approach that involves optimizing a wideband 2-D sparse array alongside multiline reception. Their method is based on the beam patterns computed for various signal fractional bandwidths that are optimized through the SA algorithm. This approach led to improved volume rate imaging capabilities, however, the proposed method was only tested using phantom image simulations.

Stochastic optimization algorithms such as SA have been effectively applied to design diverse sparse arrays in narrow and wideband conditions, but their use can be complex and not easy to implement in practice. The SA method mirrors the annealing process in metals, and therefore using this algorithm involves frequent and continual movements at different temperatures. Thus, configuring the temperature and cooling schedule becomes complex, potentially causing improper movements and impacting the final solution. Additionally, precisely designing the communication mechanism for determining the probabilities for possible moves to generate a candidate solution, is crucial for the SA's performance. Because of that, recent works are also
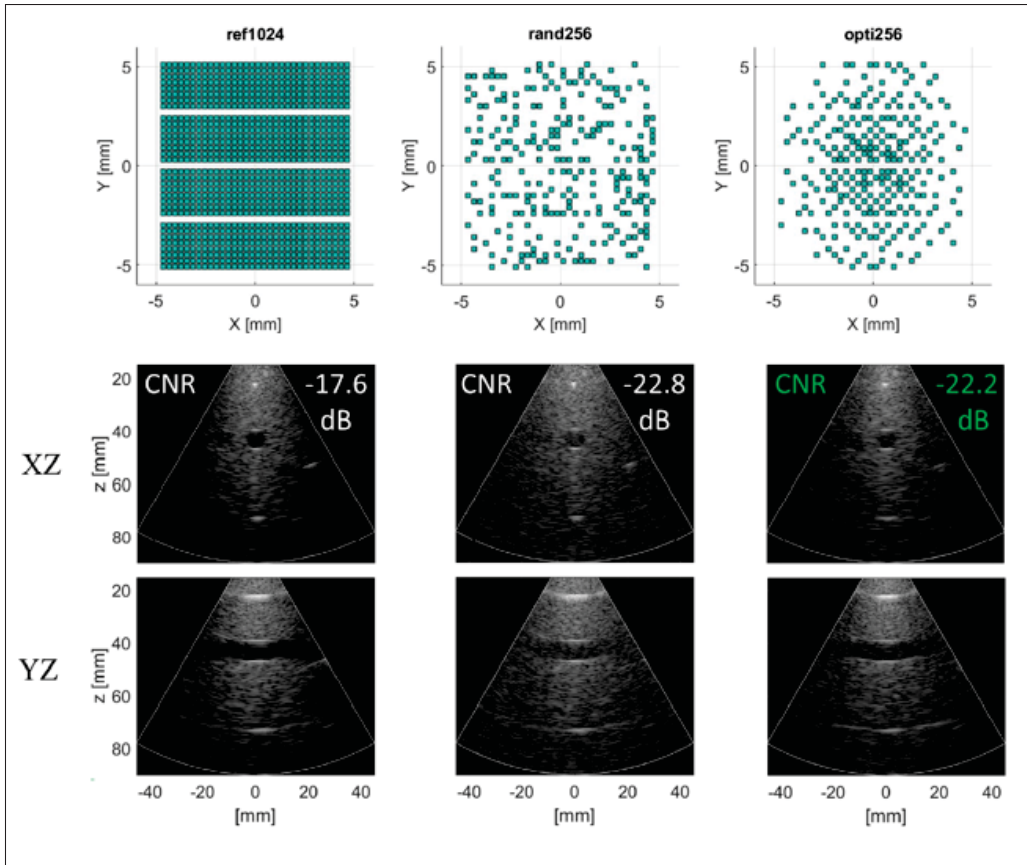
Figure 1.12   2-D phased array selected layouts: the reference array
(ref1024), the random array (rand256), and the optimized array (opti256)
and phantom image slices
Adapted from Roux *et al.* (2018, p. 5)

exploring alternatives other than refining the SA algorithm, for instance using other algorithms such as particle swarm optimization (Zhang, Bai, Zheng & Zhou, 2020). Moreover, due to the substantial computational resources and convergence issues associated with optimized sparse design methods, utilizing simplified search algorithms and exploring deterministic methods providing suboptimal array designs emerge as potential alternatives (Ramalli, Boni, Roux, Liebgott & Tortoli, 2022).

1.4   Overview of compressive sensing (CS)

The advance of ultrasonic array probes with an increasing number of elements over traditional testing with a monolithic probe has led to significant progress in NDT. On the other hand, this tendency to use transducers with high element count also leads to a significant increase in data collection and processing. Even reducing the number of elements, there is still a large amount of data generated that requires subsequent sampling and digital conversion, which leads to a considerable amount of data processing in real-time. These computational demands stem from the principles outlined in the Nyquist-Shannon theorem, which dictate that the sampling rate (SR) must be at least twice the maximum frequency present in the signal to prevent aliasing. The phenomenon of aliasing refers to distortions or misrepresentations of a signal that occurs when it is improperly sampled or digitized. Therefore, standard analog-to-digital converter (ADC) in the area of data conversion usually works with signals uniformly sampled at or above the Nyquist rate in some situations (Candes & Wakin, 2008). These signals are deemed compressible when represented in a transform basis like Fourier, indicating that a majority of coefficients are insignificant for reconstructing the original signal and can be discarded. In simpler terms, traditional compression methods operate on obtaining complete high-dimensional measurements to later discard (compress) most coefficients and inverse-transform the relevant ones to generate a faithful representation of the acquired signal (Achim, Buxton, Tzagkarakis & Tsakalides, 2010). Despite the significant success of transform domain compression in practical applications, this process is inefficient because most of the output from the ADC conversion is discarded. Extending this to a matrix array probe that might contain thousands of elements, and thus generate a huge amount of data, would be even more ineffective. Therefore, finding an effective compression method that can be successfully performed using denser arrays would be of great interest.

The recent advent of compressive sensing (CS) completely changed the traditional compression paradigm (Donoho, 2006; Candes & Wakin, 2008). According to the CS theory, it is possible to recover signals from fewer random measurements when compared to traditional methods that use high-dimensional uniform sampling. In this case, instead of having sampling followed by

compression, the CS proposes just acquiring the relevant signal information. In other words, CS uses a simple and efficient approach to measure the useful information embedded in sparse signals. Hence, this approach is interesting for PAUT, especially for matrix phased arrays in the context of 3-D TFM acquisition and processing. The concept of compressive sensing is straightforward to express mathematically, but determining the sparsest vector solution that matches the random measurements is still considered a non-polynomial (NP) hard problem. It was only in the last 18 years that advances in applied mathematics and statistics have led to the development of efficient algorithms to solve the CS undetermined inverse problem in identifying with high probability the corresponding sparse vector (Candes & Tao, 2005, 2006; Tropp & Gilbert, 2007).

The CS theory asserts that it is possible to recover the information under two conditions: sparsity and incoherence. Sparsity is related to the signal, which requires to be sparse in some domain (e.g., Fourier, discrete cosine transform (DCT), wavelet, etc.), and incoherence is related to the sensing modality (Candes & Wakin, 2008). Considering a signal x, which can be visualized as a column vector $N \times 1$ containing elements $x[n]$, with $n = 1, 2, ..., N$, it is possible to represent this signal in terms of an orthogonal basis of $N \times 1$ vectors $\{\psi_{i=1}^N\}$. Then, taking the $N \times N$ basis matrix Ψ containing vectors $\{\psi_i\}$ as columns, with $i = 1, 2, ..., N$, the signal x is written as a linear combination (Baraniuk, 2007):

$$x = \sum_{i=1}^{N} s_i \psi_i \quad \text{or} \quad x = \Psi s \tag{1.7}$$

where s is the column vector $N \times 1$ of weighting coefficients also named as the sparse vector if the vector presents a sufficient level of sparsity in a transform base. In this case, x in the time domain and s in the Ψ domain are equivalent representations. It was shown by Candes, Romberg & Tao (2006) and Donoho (2006) that is possible to recover a signal that is sparse on one transform basis Ψ from a second measurement basis, Φ, which is incoherent with Ψ. In this case, the signal x is said to be $K-$sparse in a proper basis Ψ only if a small number K of coefficients are non-zero. Thus, the CS mathematical model is:

$$y = \Phi x \qquad (1.8)$$

where y is the $M \times 1$ compressive measurement vector, measured using the $M \times N$ matrix Φ containing random variables, with $M \ll N$ representing a drastic subsampling (Achim *et al.*, 2010). Then, Eq.1.8 can be rewritten as:

$$y = \Phi x = \Phi \Psi s = \Theta s \qquad (1.9)$$

where Θ is a matrix $M \times N$, and where the matrix Ψ is fixed as it doesn't depend on x. The matrix Θ and the vector y are known components, and thus, the solution consists of finding s, which can finally be inverse-transformed to obtain x using Eq.1.7. To better illustrate the process, Figure 1.13 depicts a CS measurement process using a measurement matrix Φ composed of Gaussian random distributed numbers, and with Ψ represented by a discrete cosine transform matrix and a sparse vector s with $K = 4$.
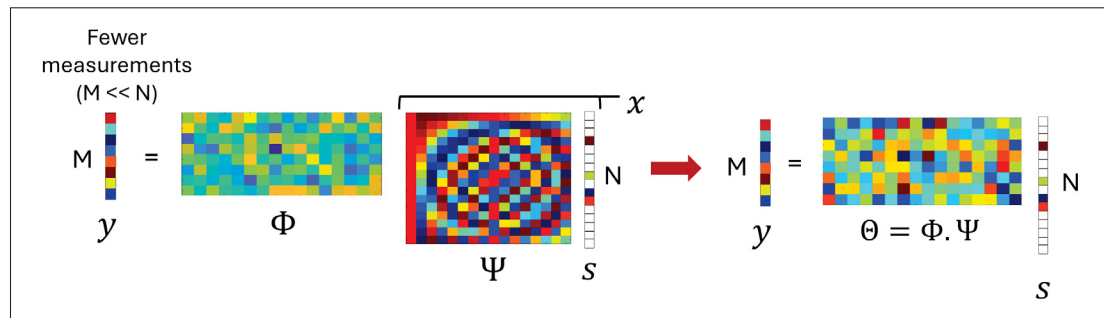
Figure 1.13   Compressive sensing measurement process using the Gaussian random measurement matrix and DCT

Considering the promising advancements in digital signal processing offered by a successful subsampling recovery, there has been a rapid increase in the adoption of CS across engineering and applied sciences in recent decades. However, it's important to note that signal recovery through CS is not entirely guaranteed in all cases, as most natural signals are never exactly sparse, but instead, CS recovery is achievable with high probability under certain conditions. Consequently,

numerous academic papers have explored the theoretical feasibility of implementing CS in a variety of fields (Bao, Li, Sun, Yu & Ou, 2013; Brunelli & Caione, 2015; Kruizinga *et al.*, 2017; Zhang *et al.*, 2022). The forthcoming efforts are directed toward practically implementing CS on acquisition devices, which is currently an obstacle and is at the development stage (Yoo *et al.*, 2012; Candès & Becker, 2013; Silva *et al.*, 2020; Park, Zhao, Park, Sun & Chae, 2021).

In NDT, the CS approach can be found applied to ultrasonic guided waves (Perelli, Di Ianni, Marzani, De Marchi & Masetti, 2013; Perelli, De Marchi, Flamigni, Marzani & Masetti, 2015), but so far just a few works have been conducted on PAUT (Bai *et al.*, 2018b; Pérez, Kirchhof, Krieg & Römer, 2020; Xu *et al.*, 2023). The current state-of-the-art of CS in NDT suggests that achieving experimental signal recovery at sub-Nyquist rates has not yet been accomplished. Despite achieving interesting results of CS applied to PAUT using linear arrays in simulations, the works from Bai, Chen, Jia & Zeng (2017), Bai *et al.* (2018b), and Xu *et al.* (2023) were not able to successfully implement the recovery of experimental data at the sub-Nyquist rate as they did in a simulation environment. In other recent work, Xu, Wang, Yao & Li (2021) also proposed a method for recovering FMC data from a 5-MHz linear phased array that was sampled at 62.5 MHz employing a CS framework. Satisfactory recovery accuracy was, however, only possible when applying just 60% of compression rate (CR), which is not sufficient to overcome the Nyquist limitation in this case. The poor success of these works in the sparse recovery of experimental FMC data acquired at a sub-Nyquist SR may be attributed to the use of inappropriate transform bases in the reconstruction framework or the neglect of incoherence in the sampling scheme. The challenge of implementing CS mainly relies on designing an efficient measurement matrix Φ in a proper transform basis Ψ, so that the information of any $K-$sparse signal does not pass by distortions or losses due to the dimensionality reduction depicted in Figure 1.13. This aspect hasn't been addressed in the existing NDT literature utilizing CS. Ultrasonic signals are typically not inherently sparse, as they often contain a wide range of frequencies, reflections, and other characteristics (front and back walls, mode-converted waves, noise, etc.), leading to a dense representation due to the rich information carried within the signal. Therefore, relying solely on signal sparsity cannot ensure a successful CS recovery. Moreover, there is a noticeable gap

in research addressing the time-consuming nature of recovering the entire FMC dataset from denser probes. In this case, the combination of CS and sparse array approaches is advantageous, as it can significantly enhance the data acquisition and simultaneously reduce the generated data size. The reduction of the collected A-scans achieved using sparse array configurations can increase the CS recovery time. At the same time, when properly designed, sparse arrays can maintain sufficient TFM accuracy. Therefore, this reinforces the need for further investigation of combining sparse array techniques and CS on the use of 3-D TFM ultrasonic imaging using matrix phased arrays.

1.5   Outlining research objectives and article presentation

This literature review chapter presented the recent advancements in ultrasonic inspection and imaging techniques, highlighting the evolution from monolithic to denser array transducers and the transition of research-exclusive methods like FMC-TFM to commercial viability. It also discussed the potential of 2-D array probes for improved inspections through a three-dimensional view and enhanced resolution, particularly evident in their application within the TFM framework. Despite their potential, the adoption of these high-count element probes encounters obstacles in the field of NDT. This research project's scope intends to overcome the existing limitations of ultrasonic matrix phased arrays, aiming to bridge the gaps preventing the widespread industrial adoption of volumetric imaging. After recognizing the sparse array technique and compressive sensing as the most promising alternatives, this project investigates the combination of these techniques to improve TFM productivity. The main objective of this study is the development of an innovative CS strategy applied to ultrasonic sparse arrays for lightweight and faster 3-D TFM imaging. To achieve this, the following specific objectives are:

• To obtain the minimum number of active elements that effectively perform as the full reference array through innovative sparse array designs.

• To develop an efficient compressive sensing (CS) framework capable of recovering FMC ultrasonic signals using sampling rates under the Nyquist theorem limit.

• To analyze the efficiency of CS combined with the sparse array concept in the generation of TFM ultrasonic images.

Three articles addressing the objectives are presented in the course of this thesis. The first article, presented in Chapter 2, introduces a simplified and straightforward approach to designing the optimal sparse array layout of linear ultrasonic transducers based on array BP simulations, without using complex stochastic optimization algorithms. This approach aimed to enhance TFM productivity by minimizing the number of firing events necessary to replicate full array performance, addressing limitations associated with real-time measurements. The method was compared with the full array (FMC) and PWI, an emerging acquisition strategy aimed at improving frame rate while keeping high image quality. Additionally, this study introduced a periodic sparse array design as an alternative method for sparse-TFM imaging.

The second article, presented in Chapter 3, refines and adapts the method from the first article to design 2-D sparse arrays. The method was then based on pulse-echo 3-D point spread function (PSF) simulations, where an intermediate step was introduced that included removing symmetrical arrangements and adding more spatial limitations to decrease the computational load of this analysis. Based on the observed trend in optimal layouts with varying firing events, the study also demonstrated the feasibility of creating suboptimal 2-D sparse arrays without undergoing any exploration process, which is attractive for designing other sparse 2-D probes that can feature high-count elements (e.g., ranging from 256 to 1024).

Finally, the third article in Chapter 4 combined compressive sensing and sparse array approaches. An efficient CS framework based on sparsity and incoherence concepts was proposed for an optimal CS matrix selection and to enable FMC signal recovery at the sub-Nyquist rate. Then, the signal recovery was performed according to a sparse array arrangement designed to act as the full array obtained from the previous studies. The method was tested on experimental data, estimating signal recovery accuracy, and evaluating how data reduction affected image quality and defect sizing. TFM image formation and CS reconstruction times were also assessed, comparing CS-FMC and sparse CS datasets.

CHAPTER 2

MINIMUM TRANSMISSION EVENTS FOR FAST ULTRASONIC TFM IMAGING: A COMPARATIVE STUDY

Lucas Pereira Piedade[1] , Guillaume Painchaud-April[2] , Alain Le Duff[2] , Pierre Bélanger[1]

[1] PULETS, Department of Mechanical Engineering, École de Technologie Supérieure,
1100 Notre-Dame Ouest, Montréal, Québec, Canada H3C 1K3
[2] Evident Industrial, 3415 Rue Pierre-Ardouin, Québec, Québec, Canada G1P 0B3

2.1   Abstract

High-quality images can be achieved via the total focusing method (TFM), an imaging algorithm used in ultrasonic nondestructive testing (NDT), which post-processes data from full matrix captures (FMC). However, real-time TFM is resource-heavy and only feasible with high-end instruments, which limits its wider use in industrial applications. In this work, a sparse array approach was investigated to increase TFM productivity by reducing the number of transmission events. Therefore, a comparison was made between two sparse layouts and plane wave imaging (PWI) in terms of contrast-to-noise ratio (CNR) and the array performance indicator (API). The aim was to find a trade-off between image quality and the number of firing events required. The comparison showed that the sparse array outperforms PWI when more than 3 firing events are used. Results indicate that the proposed sparse-TFM can in fact increase TFM productivity without compromising the CNR and API levels.

2.2   Introduction

In the last decades, phased array ultrasonic testing (PAUT) became a widely used technique in the nondestructive testing (NDT) of materials and structures, owing to its benefits over traditional ultrasonic testing (UT), such as flexibility and reliability (Felice & Fan, 2018). Unlike conventional single element ultrasonic transducers, ultrasonic phased array probes comprise several small individual piezoelectric elements that can be independently pulsed. This allows to

perform several types of inspection by controlling each element, and thus insonifying parts using various patterns. Consequently, this technology has also led to different imaging algorithms for defect characterization and data interpretation. The advent of data acquisition systems allowing the transmission and reception of all elements resulted in a data acquisition scheme called the full matrix capture (FMC). In FMC, a pulse is transmitted sequentially to one element at a time, and received signals are recorded by all elements of the array. Therefore, a linear probe containing N elements will make N emissions with N receptions in each event, generating a complete $N \times N$ matrix of data. The FMC concept was introduced by Holmes *et al.* (2005), along with the total focusing method (TFM) algorithm. This imaging algorithm synthetically focuses the array on each pixel from the grid of subsurface regions through the post-processing of FMC, therefore generating superior image resolution relative to conventional PAUT imaging methods (Fan *et al.*, 2014). Today, TFM is beginning to be used in different industrial segments (Lane *et al.*, 2010; Russell *et al.*, 2012; Li *et al.*, 2013; Mansur Rodrigues Filho & Bélanger, 2021). However, real-time processing of FMC-TFM can be limited for some industrial applications, such as railroad rail flaw detection (Clark, 2004), which require high-speed detection. This limitation is due to two major factors: the first is the time required to acquire the FMC; there is a time interval between the FMC firing events that leads to slow data collection. The second is the amount of data to be post-processed, which makes TFM imaging computation significantly time-consuming. There are also other applications for which the cost of the high-end equipment required to perform FMC-TFM is simply not justifiable.

Alternatively, sparse array techniques provide an effective solution to some of these shortcomings (Austeng & Holm, 2002; Moreau *et al.*, 2009). When using this approach, a few elements from the array are selected in transmission while all or just some are used in reception, reducing the acquisition time and the amount of data to be processed. Even though sparse array methods have been extensively studied in the medical field since the 1990s (Lockwood, Li, O'Donnell & Foster, 1996; Lockwood, Talman & Brunke, 1998), and were later introduced in NDT (Moreau *et al.*, 2009), sparse array design is still very dynamic as a research focus. The search for the best sparse array configuration can be carried out using different approaches. For instance, the

standard random sparse method (Moreau *et al.*, 2009; Davidsen, Jensen & Smith, 1994) uses a predefined number of configurations that are randomly generated from a portion of the full array. Then, the best configuration is chosen in terms of the beam pattern (BP) features, such as the sidelobe level (SLL) and the grating lobe level (GLL). However, all the possible configurations are not explored in this method. Other random approaches based on stochastic optimization, including simulated annealing (SA) (Roux *et al.*, 2018; Trucco, 1999) and genetic algorithm (GA) (Austeng, Holm, Weber, Aakvaag & Iranpour, 1997), are usually preferred when the optimal configuration is explored on a small scale. These random optimization algorithms present interesting features such as finite time exploration and a convergence property to the global minimum, using previously evaluated configurations instead of suggesting a pure random solution (Diarra *et al.*, 2016; Roux *et al.*, 2017). Nonetheless, the GA requires more time and computation robustness than the SA for larger optimization schemes, and presents premature convergence in some cases (Adler, 1993; Hwang & He, 2006). Moreover, when using the SA, a precise design of the communication mechanism, which provides the probabilities of the possible moves needed to generate a candidate solution, might be critical to the performance of this approach. Recent research papers have applied GA in dual-layer media (Hu, Du, Xu, Jeong & Wang, 2017), and have also used particle swarm optimization (Zhang *et al.*, 2020). Hu *et al.* (2017) achieved an error of 5.1% over TFM when using 8 firings with their sparse approach, whereas Zhang *et al.* (2020) optimized a sparse layout of around 80% of the full array, obtaining a small gain in image quality in simulations.

In this paper, the sparse array technique using the minimum number of transmission events is investigated as an alternative to increase TFM productivity. In a context where a limited number of transmission events is used, the narrow number of possible combinations makes the computation of the BP and the exploration of the entire set of array layouts viable. This opens the possibility to design the best layout adopting a simplified and straightforward approach without using complex stochastic optimization algorithms such as SA and GA. The SA algorithm emulates the annealing process of metals, adopting frequent and constant movements concerning the varying temperature. Therefore, setting the temperature and the cooling schedule is quite

complex as could lead to inappropriate movements and affect the final solution. The GA on the other hand, is an evolutionary algorithm that often requires a precise design of the objective function and fails to manage large populations of possible solutions, making it also complex to handle. The proposed method is assessed experimentally, and a comparative study is done with another technique known as plane wave imaging (PWI), which also generates image using a restricted amount of data. The comparison is made by testing the same number of transmission events. The images generated are quantitatively analyzed to find a trade-off between image quality and the number of firing events.

2.3   Materials and methods

2.3.1   Experiments

Experiments were carried out using an Olympus linear ultrasonic phased array 5L64 (5 MHz center frequency, 0.60 mm pitch, and 64 elements) connected to a Verasonics Vantage-64 LE. The probe was placed in contact with an aluminum block, with ultrasonic speed measured at 6354 m/s, containing five 1 mm side drill holes (SDH) drilled at different depths. Measurements were performed for two different orientations of the block, vertical and horizontal, to verify the capacity of the sparse array technique to resolve SDH distributed axially and laterally. Henceforth in the present work, the vertical and horizontal positions of the block will be named VPO and HPO, respectively. The FMC acquisition was done for each position at a sampling rate of 62.5 MHz, and the experimental data was imported to the MATLAB environment to generate images using the TFM algorithm. Fig. 2.1 shows a schematic of the block along with the region of interest of each position. The imaging area measured 140×40 mm for VPO and 70×70 mm for HPO, with a square pixel resolution of 0.10 mm.

2.3.1.1   Total focusing method (TFM)

In the FMC acquisition scheme, each piezoelectric element from an array containing N elements is excited sequentially, while all the elements receive the back-propagated waves. The received

a) Schematic of the aluminum block

b) Vertical position (VPO)

c) Horizontal position (HPO)
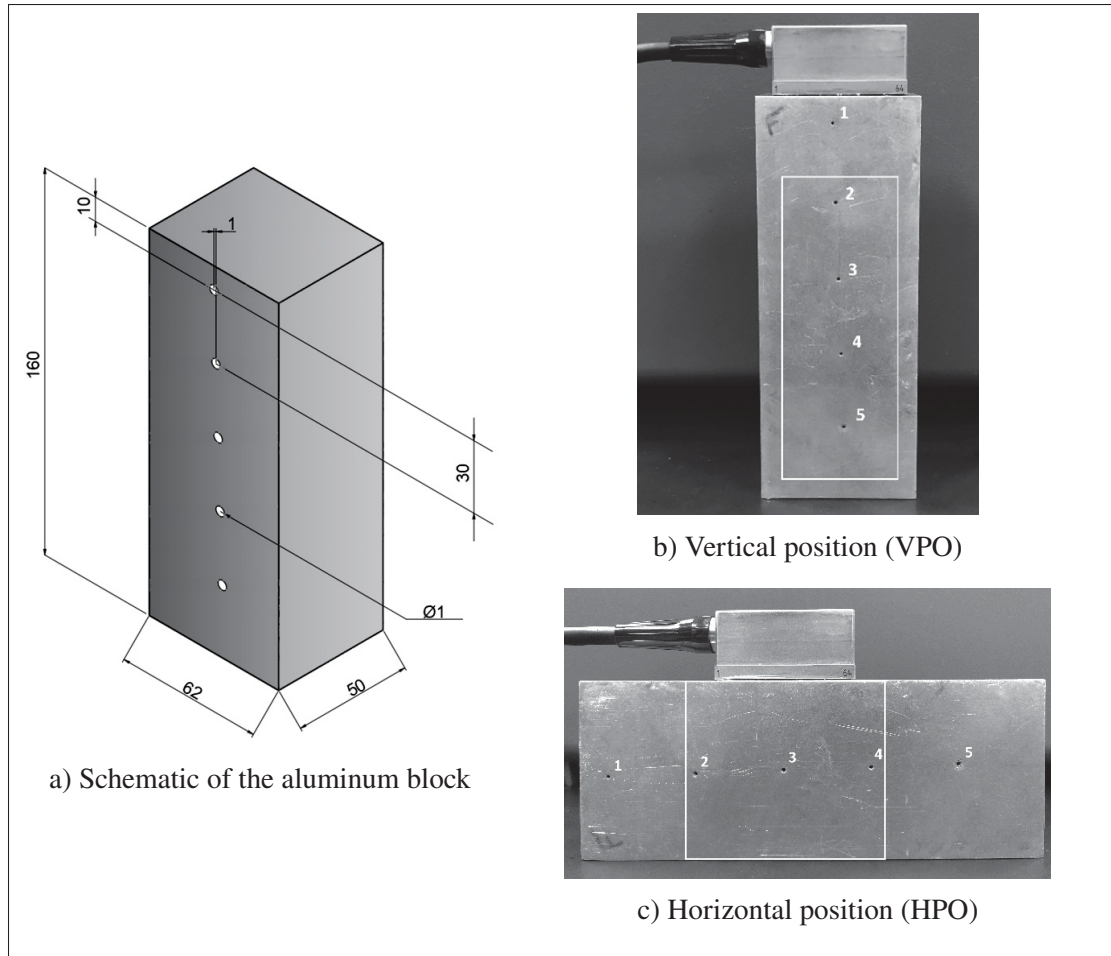
Figure 2.1   (a) Schematic of the aluminum block and measurement positions (b and c)

signals are then stored down to the Nth element $(S_{11(t)}, S_{12(t)}, \cdots, S_{1N(t)}, S_{21(t)}, S_{22(t)}, \cdots, S_{2N(t)} \cdots S_{NN(t)})$ obtaining the complete set of data. After the acquisition using the FMC, the data can be post-processed in the MATLAB environment. The TFM imaging algorithm can then be employed to generate the images. In this technique, a region of interest is first discretized in a grid of pixels, and then the signals S_{nm} at every point are coherently summed according to the following equation:

$$I(x, y) = \left| H \left(\sum_{n=1}^{N} \sum_{m=1}^{N} S_{nm} (t_{nm}) \right) \right| \tag{2.1}$$

where $I(x, z)$ is the image intensity, H is the Hilbert transform, and t_{nm} is the time-of-flight (TOF) of the ultrasonic wave propagation from the emitter (e) to the pixel P location, and back to the receiver (r). The TFM is schematized in Fig. 2.2 using the OXZ coordinate system. The origin O is the center of the array, with the X-axis oriented to the right, and the Z-axis perpendicular to the array. The array elements are distributed in the X-direction.
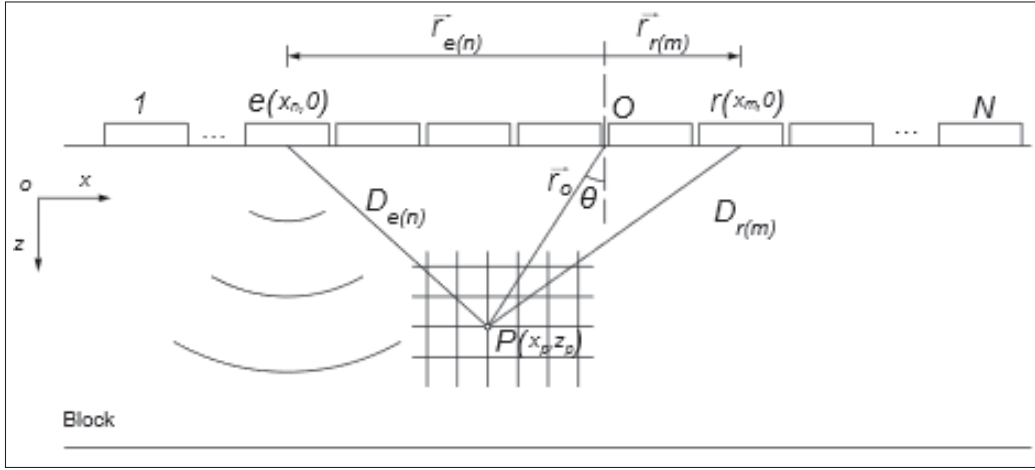
Figure 2.2   Schematic of the FMC-TFM

The path taken by the ultrasonic wave is the path traveled with the least time, following Fermat's principle, and can be found with simple geometric relationships. Thus, t_{nm} is calculated using the speed of sound of the inspected medium. Eq. 2.1 can therefore be rewritten as follows:

$$I(x, y) = \left| H \left(\sum_{n=1}^{N} \sum_{m=1}^{N} S_{nm} \left(\frac{\sqrt{(x_p - x_n)^2 + z_p^2} + \sqrt{(x_p - x_m)^2 + z_p^2}}{v_L} \right) \right) \right| \tag{2.2}$$

where x_n and x_m are the position in the x-direction of the nth emitter (e) and the mth receiver (r), respectively, (x_p, z_p) is the location of pixel P, and v_L is the longitudinal sound velocity of the medium. Despite the benefits of high resolution achieved by the TFM algorithm, one can see that TFM demands a considerable number of calculations. However, using a sparsely populated array in transmission would improve TFM speed as well as reduce the amount of collected data. Hence, sparse array techniques have the potential to increase TFM productivity. In this study,

the sparse array is synthetically assembled using the FMC. According to the desired number of active elements (N_e) in transmission (e. g., 5 out of 64 elements), a sparse matrix of data is selected, with all elements in reception. In this case, the $N \times N$ FMC matrix is turned into an $N_e \times N$ matrix. For the calculation of TFM, only the FMC columns corresponding to N_e are used in Eq. 2.2. Therefore, in this paper, a sparse-TFM corresponds to an image generated with a subset of the FMC.

2.3.1.2 Design of sparse array

The proposed design procedure consists in comparing the two-way radiation pattern (also known as the array beam pattern (BP)) of the sparse array against the one from the FMC. The beam pattern expresses the array angular impulse response, and therefore represents the imaging capabilities of the system (Moreau *et al.*, 2009). Thus, the sparse array layout can be designed based on the characteristics of the BP, as the contrast relies on sidelobes, and the main lobe resolves the lateral resolution. Taking Eq. 2.1 and expressing it in the frequency domain (Bannouf *et al.*, 2013), it follows that:

$$I(x, y) = \sum_{\omega} \sum_{nm} S_{nm}(\omega) \, e^{jk \left(D_{e(n)} + D_{r(m)} \right)} \tag{2.3}$$

where $S_{nm}(\omega)$ is the frequency spectrum of array signals, and $D_{e(n)}$ and $D_{r(m)}$ are the distances between the emitter and receiver to the point P, respectively. From Fig. 2.2, using the law of cosines (Schmerr Jr, 2014), we have:

$$D_{e(n)} = \sqrt{r_o^2 + (x_n)^2 - 2x_n r_o \sin \theta}. \tag{2.4}$$

Considering that the defects are in the far-field of the array i.e., $x_n/r_o \ll 1$ and $x_m/r_o \ll 1$, and expanding Eq. 2.4 to only the first order as (Schmerr Jr, 2014):

$$D_{e(n)} = r_o - x_n \sin \theta \tag{2.5}$$

and

$$D_{r(m)} = r_o - x_m \sin \theta \tag{2.6}$$

In this case, $x_n = \overrightarrow{r_{e(n)}} = np$ and $x_m = \overrightarrow{r_{r(m)}} = mp$, with p corresponding to the pitch. Thus, adopting this approximation, Eq. 2.3 can be written as:

$$I(x, y) = \sum_{\omega} \sum_{nm} e^{jk2r_o} S_{nm}(\omega) e^{-jknp \sin \theta} e^{-jkmp \sin \theta}. \tag{2.7}$$

In Eq. 2.7, the two latter terms are related to the angular resolution aspect, whereas the others are related to the radial resolution. Hence, considering the emission and reception events separately, the beam pattern (BP) of the array is found:

$$BP = \sum_{n=1}^{N} w_n^e(\omega) e^{-jknp \sin \theta} \sum_{m=1}^{N} w_m^r(\omega) e^{-jkmp \sin \theta} \tag{2.8}$$

where w_n^e and w_m^r are the weighting functions in emission and reception, respectively. The proposed exploration algorithm was thus executed in the MATLAB environment. After the trials, the best layout was used experimentally. The algorithm works as follows: first, all the possible combinations from a given reduced sparse array set (e.g., 3 out of 64 elements in transmission) are computed and stored. For that, an equation that computes the number of possible combinations or the so-called binomial coefficient is initially used, given by:

$$C_{i,j} = \binom{i}{j} = \frac{i!}{j!(i-j)!}. \tag{2.9}$$

Eq. 2.9 provides the number of combinations without repetition of i units taken j at a time, where a matrix $C_{i,j}$ with j columns and i rows, containing the subsets, is formed inside MATLAB.

Then, the layouts are applied in transmission with the full array in reception, and the BP is obtained using Eq. 2.8. In this case, no weighting functions are applied either in transmission or reception, where the values of w_n^e and w_m^r are set to 1. The configuration of the active elements should provide the desired imaging feature, such as the contrast or resolution. Those image quality parameters rely on the main lobe width, the levels of the sidelobes, and grating lobes from the BP. Hence, the main lobe width (MLW) at half-maximum (-6 dB) and the sidelobe level (SLL) are used as criteria for selecting the best sparse layout. The MLW corresponds to the distance between two points ($x_2 - x_1$) at half maximum (-6 dB). On the other hand, the SLL is measured by a peak search method and corresponds to the highest peak value after the main lobe. Fig. 2.3 illustrates how the MLW, and SLL are set.
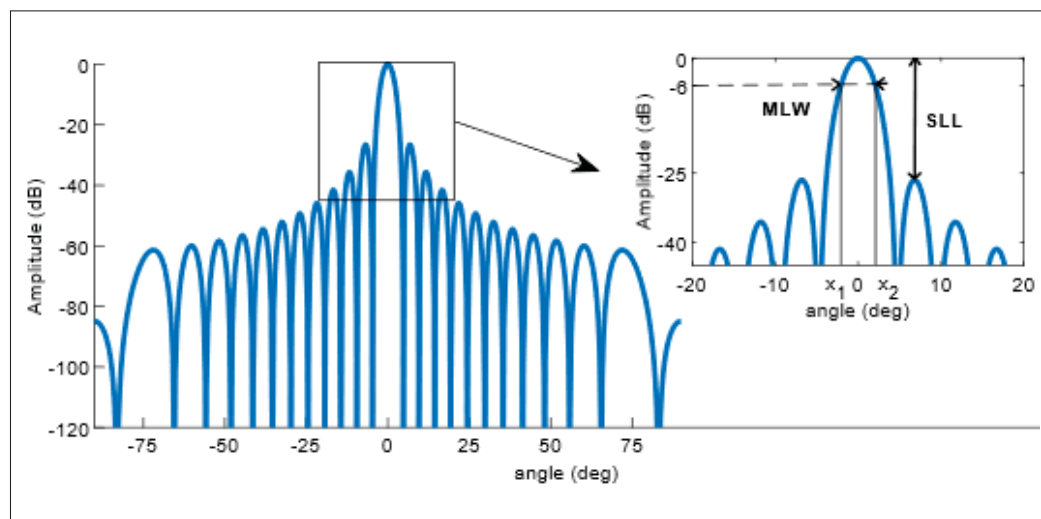
Figure 2.3   Rectangular radiation plot of a theoretical ultrasonic phased array showing the MLW and SLL measurement

These two features are computed, passing through two thresholds $T1$ and $T2$. The first one ($T1$) refers to the MLW acceptance threshold and the other ($T2$) is related to the SLL, both being based on the BP of the full array. For this algorithm, $T1$ was set to be 1.15 times the reference array MLW. $T2$ was chosen to be the maximum sidelobe level allowed and was equal to the reference array SLL plus 6 dB. $T1$ and $T2$ were set arbitrarily so as to maintain an acceptable lateral resolution and artifacts in the image. If the solution is accepted, the result is stored, and the algorithm continues to run. Otherwise, the solution is not considered, and the algorithm selects

the next layout. When all combinations are explored, the algorithm ends, and the best layout is selected according to the narrowest MLW and the lowest SLL, or in this case, the solution that is closest to the full array in these terms. Fig. 2.4 presents the schematized algorithm workflow:
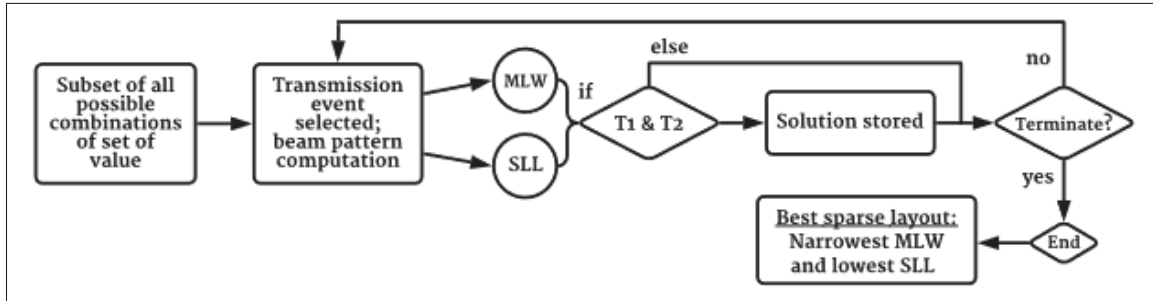
Figure 2.4   Proposed algorithm to find the best sparse array layout

2.3.1.3   Plane wave imaging (PWI) and comparative study

Another data acquisition strategy derived from medical ultrasound, named PWI, was recently proposed in NDT to improve TFM productivity (Le Jeune *et al.*, 2016). In this method, all the elements are activated in transmission, creating a coherent planar wavefront according to a delay law defined by the angle β relative to the propagation axis. The backpropagated wave is then received by all the elements. Different from the FMC acquisition, in which an $N \times N$ matrix of data is collected, PWI leads to a $P_a \times N$ matrix of data, where P_a is the number of angles used in transmission, while N is the number of receiving elements. It has already been demonstrated that a low number of transmission events can be used while maintaining a satisfactory image resolution (Tiran *et al.*, 2015; Montaldo, Tanter, Bercoff, Benech & Fink, 2009). A comparative study was therefore performed between the proposed sparse array and PWI. The number of active elements in transmission was chosen to be 1, 3, 5, and 7 for VPO, and 3, 5, and 7 for HPO, leading to a sparse-FMC matrix of $N_e \times N$. Likewise, for PWI, the number of angles P_a was set equal to Ne to compare the images generated from the same size data set. In addition to these two approaches, another sparse strategy using equally distributed elements was assessed. In the equally distributed layout, the edge elements were not used in transmission (Diarra, Robini, Tortoli, Cachard & Liebgott, 2013). In this case, the first and

the last 5 elements of the array were not considered (i.e., elements 1 to 5, and 59 to 64 for a linear probe containing 64 elements), while the others were placed in a periodic arrangement according to N_e. The study was therefore done using the FMC-TFM as the benchmark, and compared the PWI method with the best sparse array layout following the method described in section 2.3.1.2 and the regular periodic sparse array with edge elements deactivation. For better identification, the sparse array technique using the minimum transmission events is named MTE, and the term EQS is used for the equally spaced approach with edge elements deactivation. The aim is to find a trade-off between image quality and the number of firing events. To generate plane waves with the same number of firings used for the sparse array, the angle step is changed while maintaining the same sweep angle. For example, a sweep angle of $-30° - 30°$ with an angle step of 30° results in 3 firing events. This means that the PWI angles consist of $-30°$, 0°, and 30°. Likewise, the $-30° - 30°$ range with a 15° step is used for 5 firing events, and so on. In order to maintain a symmetrical pattern, only odd numbers were chosen in transmission events. Considering that plane waves are spatially restricted by the probe aperture, the sweeping angle must be defined to guarantee that most image reconstruction points are insonified by the incident wave. The area defined by the sweep angle is known as the effective area (Le Jeune *et al.*, 2016). Fig. 2.5 schematizes the concepts of effective area and PWI sweep angle.

The region of interest (ROI) is different when changing the block position (see Fig. 2.1), and therefore, the sweep angle was adapted to cover all the defects within the area. In this case, the angle range was set to $-3° - 3°$ for VPO, and $-30° - 30°$ for HPO to cover the ROI. Because the position of SDH 2 and 4 are outside the probe aperture for HPO (see Fig. 2.5), a single plane wave is not sufficient to generate the image of all the three defects simultaneously. Hence, for this case, only 3, 5, and 7 emission events were considered.

2.3.2   Metrics for image evaluation

Two metrics were selected for image evaluation: the contrast-tonoise ratio (CNR) and the array performance indicator (API). As mentioned in section 2.3.1.2, the sidelobe level might degrade the image contrast. The presence of high sidelobes results in strong image artifacts that can lead
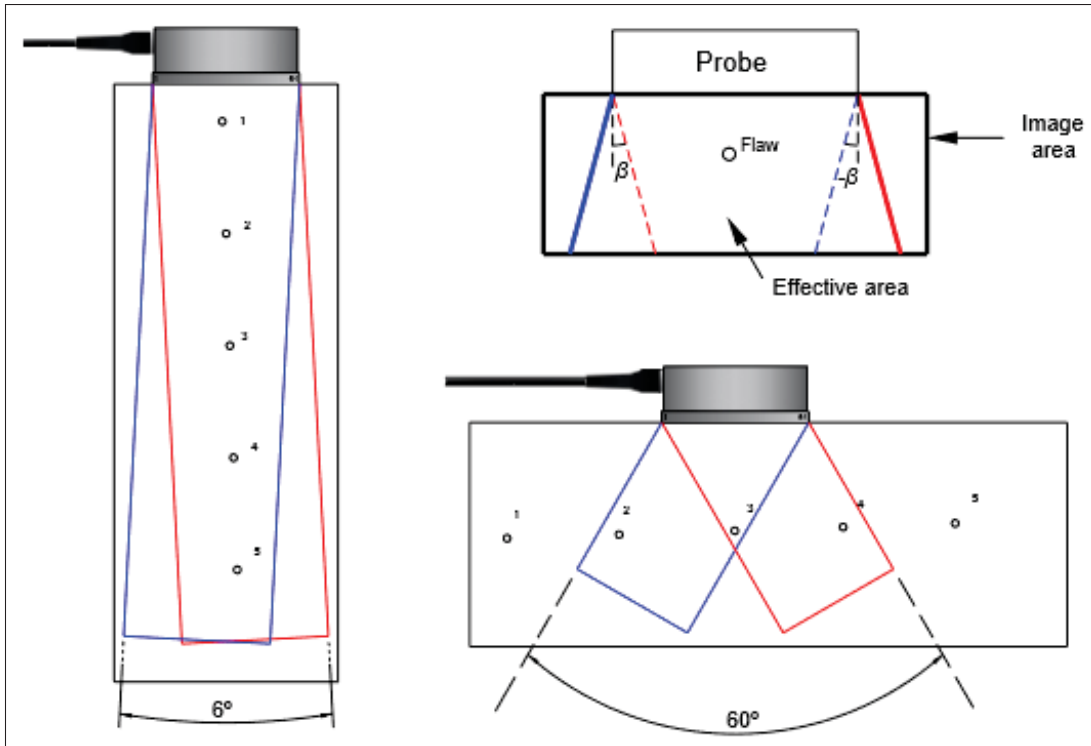
Figure 2.5   Sweep angles used for PWI according to block position and their
respective effective area

to a misinterpretation of results. The CNR metric was therefore used to measure the amplitude

of the reflection relative to the background noise. Each defect was evaluated separately, dividing

the image into equal sub-image rectangles of 30×40 mm in VPO and 23×34 mm for HPO. For

the CNR measurement, the image area was divided into signal and noise pixels portions. The

pixels with intensities ranging the maximum and down to -6 dB below the maximum intensity

($I_{max} - 6dB \leq I_{-6dB} \leq I_{max}$) were set as the signal (I_{-6dB}), where these pixels represent the

reflector area in the image (A_{-6dB}). The remaining pixels in the area are considered as noise

(I_{noise}). For each defect in the sub-image rectangle, the root mean square of I_{-6dB} divided by the

root mean square of Inoise displayed on a decibel scale yields the CNR value. Therefore, the

CNR is given by Eq. 2.10:

$$CNR = 20 \log_{10} \left(\frac{\sqrt{< I^2_{-6dB} >}}{\sqrt{< I^2_{noise} >}} \right). \tag{2.10}$$

One way to quantitatively verify the performance of the TFM imaging in terms of its ability to image a reflector is by using the array performance indicator (API). Essentially, the API is used to measure the area of the image target (Fan *et al.*, 2014). The API metric considers changes in the defect size on the images relative to the wavelength of a given material. To compute the API, Eq. 2.11 is used:

$$API = \frac{(A_{-6dB})}{\lambda^2_{Al}} \tag{2.11}$$

where A_{-6dB} is the area and λ^2_{Al} is the square of the wavelength of aluminum. The area A_{-6dB} is calculated by taking all the pixels with intensities ranging from the maximum down to -6 dB below the maximum intensity ($I_{max} - 6dB \leq I_{-6dB} \leq I_{max}$) and multiplying them by the image resolution of 0.10×0.10 mm. Thus, for each defect, this ratio is calculated.

2.4   Results and discussion

The BP of the reference array was computed according to Eq. 2.8, and the value of MLW at half-maximum, and the SLL were extracted before starting the trials. The design was done while approximating the MLW and SLL of the sparse layouts to those from the reference array. The trials using the given N_e were done for all possible combinations. Table 2.1 presents all the numerical results of the design algorithm for the N_e values used, along with the best sparse layout solution.

As N_e increases, the BP features of the best sparse layout get closer to the full array (see Table 1). After the 3-emission event, a sidelobe suppression presented by the best layout can be noted. Despite the considerable number of combinations explored for $N_e = 7$, no greater improvement

Table 2.1   Numerical results of the proposed optimization algorithm and best sparse layout for each N_e value

Number of active elements (N_e)	Number of combinations	Best sparse layout	MLW (°)	SLL (dB)
3	41,664	[16 37 52]	1.85	-21.85
5	7,624,512	[12 20 34 42 56]	1.81	-26.64
7	621,216,192	[7 18 23 34 39 50 55]	1.79	-26.97
FMC	-	-	1.68	-26.51

in MLW and SLL was observed as compared to N_e = 5. The beam patterns of the FMC and the best sparse layout with N_e = 5 are plotted in Fig. 2.6:

a)   b)
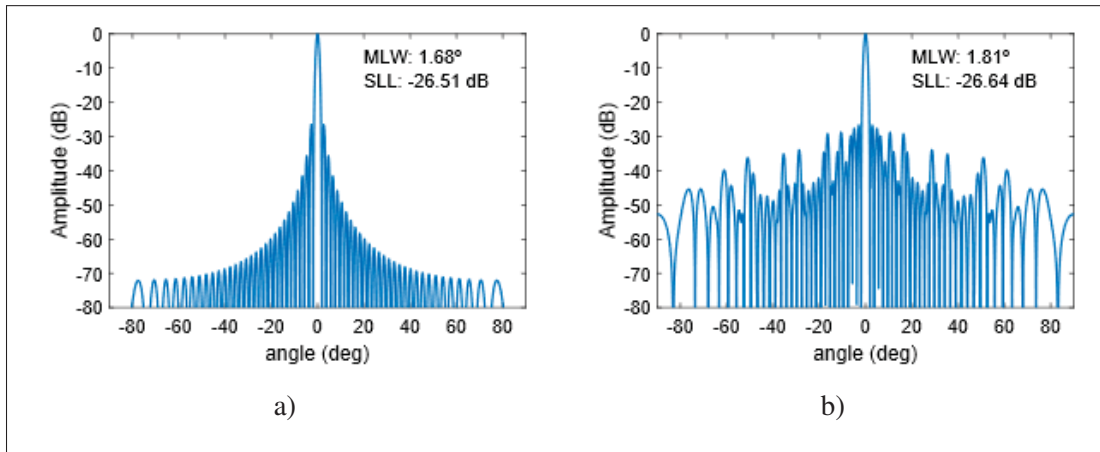
Figure 2.6   Beam pattern diagram: (a) 64-element array (FMC) and (b) best sparse layout (N_e = 5)

It can be seen in the BP diagram of the 64-element full array (Fig. 2.6 (a)) that substantial sidelobes are neighboring the main lobe. The SLL and the MLW at half-maximum for this case are −26.51 dB and 1.68°, respectively. For the sparse array layout design with N_e = 5, the MLW is 1.81° and SLL is −26.64 dB, with an MLW slightly widened when compared to the full reference array, and SLL decreased by around 0.1 dB (Fig. 2.6 (b)). In this case, the number of active elements from the array in transmission was reduced by 92.2%, which can significantly improve the TFM efficiency. The FMC-TFM images for the defined positions, VPO and HPO, used as a benchmark in this study, are displayed in Fig. 2.7.
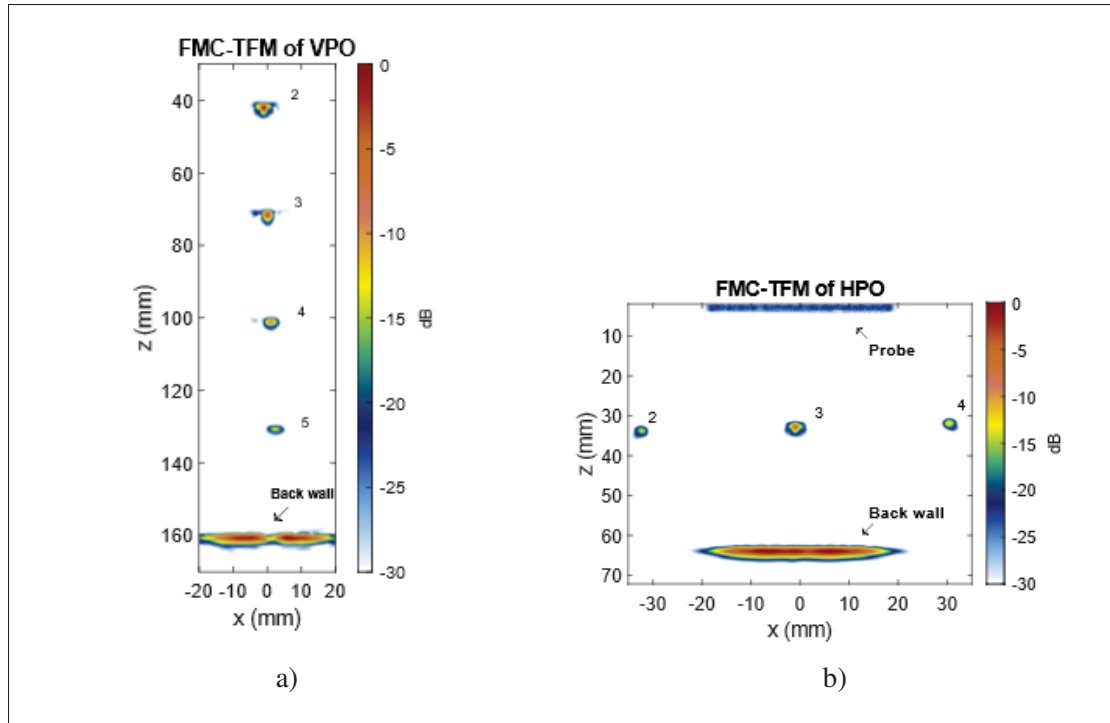
Figure 2.7   Experimental FMC-TFM defect image reconstruction: (a) VPO
and (b) HPO

From VPO (Fig. 2.7 (a)), one can see that the amplitude of the defects starts to decrease due to attenuation (SDH 2 to 5). Among all three defects in Fig. 2.7 (b), SDH 3 presents the highest amplitude, being under the probe's aperture and receiving most of the ultrasonic energy, while SDH 4 presents a higher amplitude than SDH 2. The difference in this case can be attributed to the variation of energy transmitted in those areas. The back wall and the probe position are also visible in Fig. 2.7 (b). The results of the comparative study begin with VPO. The N_e was set at 1, 3, 5, and 7 for the MTE and EQS, and using $-3° - 3°$ as the angle range for PWI with a step variable to achieve the same number of firings. The images were generated through the TFM algorithm and compared in terms of CNR and API. For better visualization, the metrics are plotted against the SDH index. Fig. 2.8 shows the ultrasonic images obtained, while Figs. 2.9 and 2.10 display the results of CNR and API for the SDHs of VPO, respectively.

Because of attenuation, the CNR graph presents a descending behavior (Fig. 2.9). The results show that for the single emission event, PWI presents a better CNR as compared to the
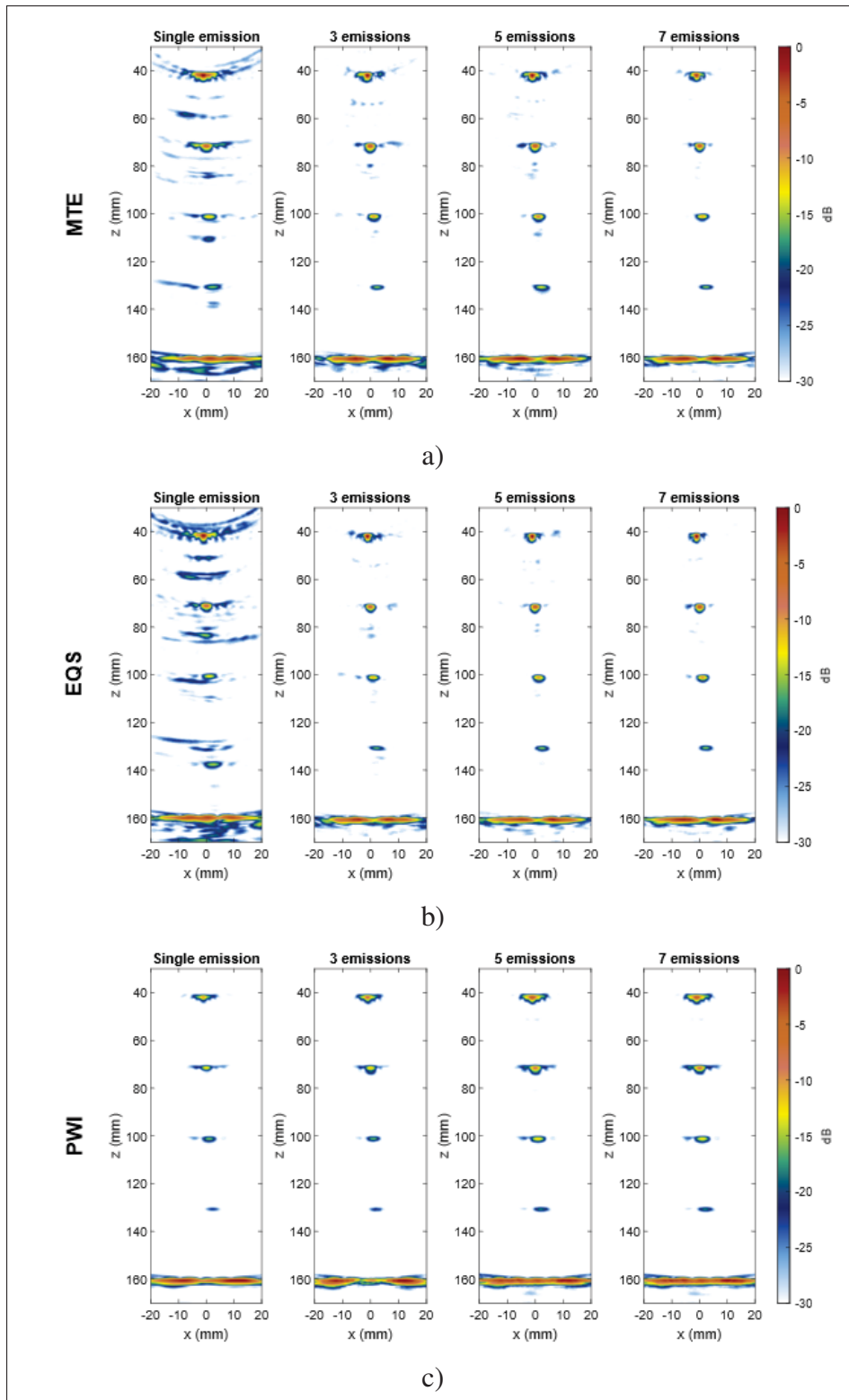
Figure 2.8   Experimental ultrasonic images of VPO
according to emission events: (a) MTE, (b) EQS, and (c) PWI
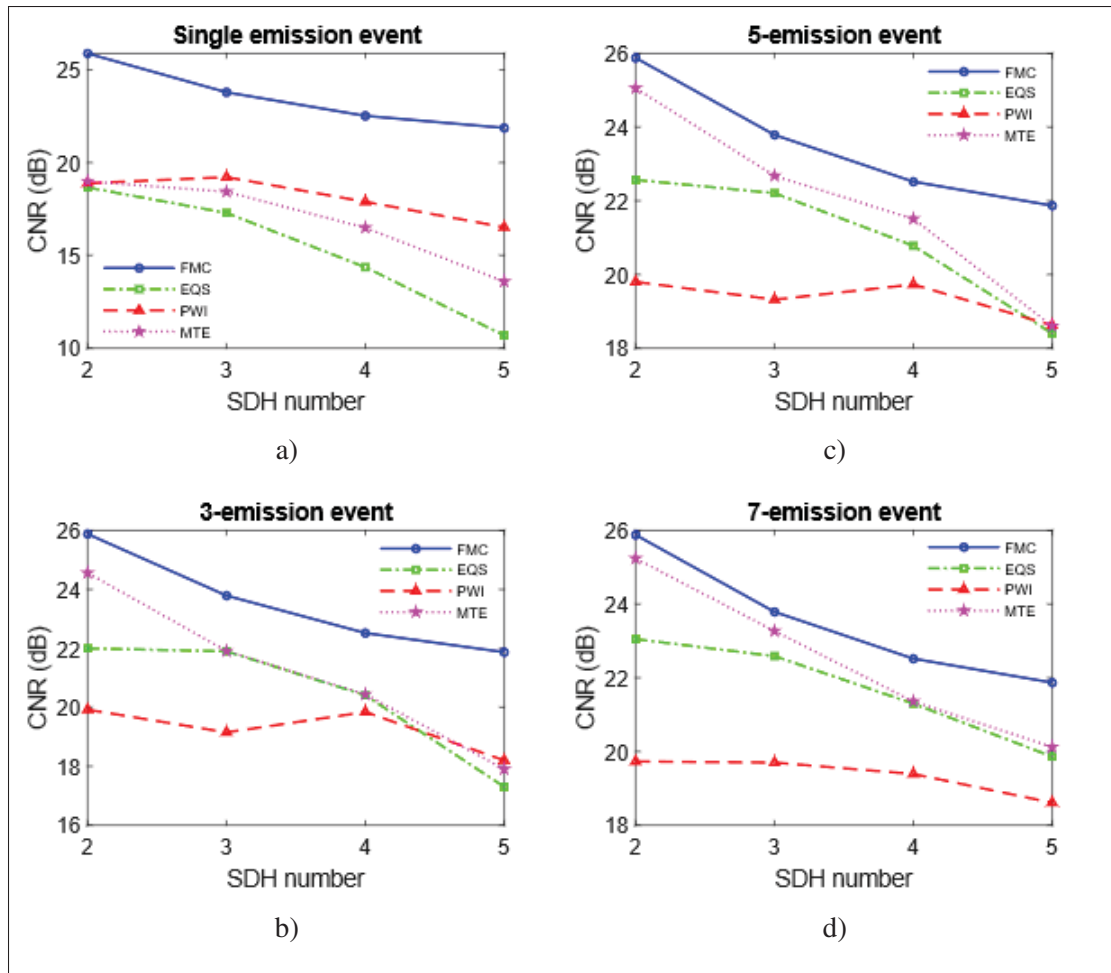
Figure 2.9   CNR curves for VPO comparing FMC, EQS, PWI and MTE for
emission events equal to: (a) $N_e = 1$, (b) $N_e = 3$, (c) $N_e = 5$ and (d) $N_e = 7$

single-element excitation from the other sparse approaches. This is a result of the difference in power that a single cylindrical wave sends inside the part in relation to the plane wave emission, which is composed of all the elements triggering according to the delay law to generate the plane wavefront. Consequently, PWI shows a CNR value 0.9 dB greater than EQS for SDH 5 in the 3-emission event. The difference was reduced to 0.17 dB for SDH 5 in the 5-emission event. The same behavior can be observed for the MTE, but the difference in CNR is smaller in this case. For the 3-emission event, the CNR of PWI for SDH 5 is 0.3 dB higher, and for the 5-emission event, showed the same CNR. However, as N_e increases, both EQS and MTE start to present CNR values close to the FMC, with MTE having the best performance. The
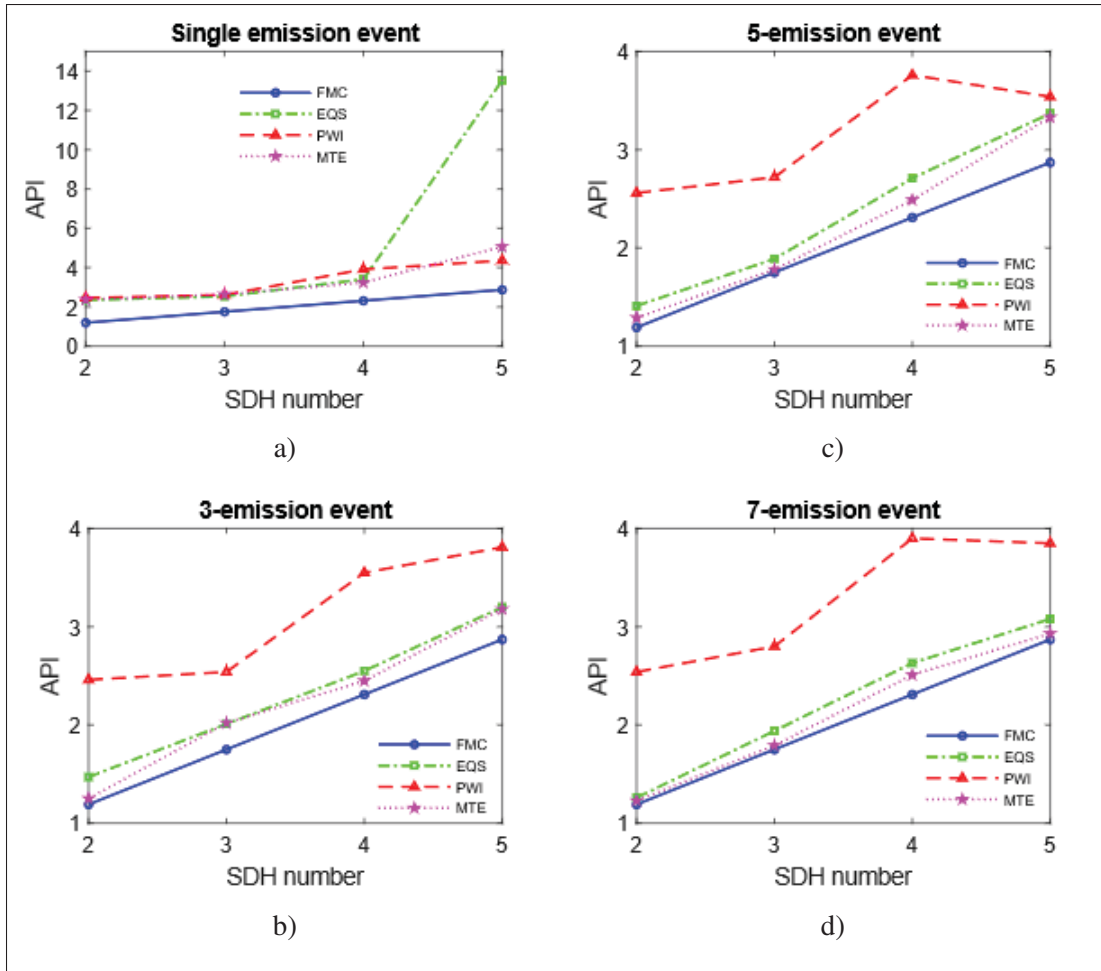
Figure 2.10   API curves for VPO comparing FMC, EQS, PWI and MTE for emission events equal to: (a) $N_e = 1$, (b) $N_e = 3$, (c) $N_e = 5$ and (d) $N_e = 7$

same behavior cannot be observed in relation to the API (Fig. 2.10). In this case, the MTE showed a better performance for all scenarios, with exception of the single emission, where it presented similar values as PWI, up to SDH 4 (see Fig. 2.10 (a)). Small API values indicate a small change in the reflector image size relative to the wavelength. The API quantifies the imaging resolution of the array, and therefore, a small API indicates a better resolution. For the HPO analysis, N_e was set to 3, 5, and 7 for the MTE, EQS, and using the angles for PWI going from $-30°$ to $30°$ to cover the entire ROI. The ultrasonic images obtained can be seen in Fig. 2.11. Unlike with the VPO, for the HPO, the sparse approach performed better than PWI for all scenarios (Figs. 2.12 and 2.13).
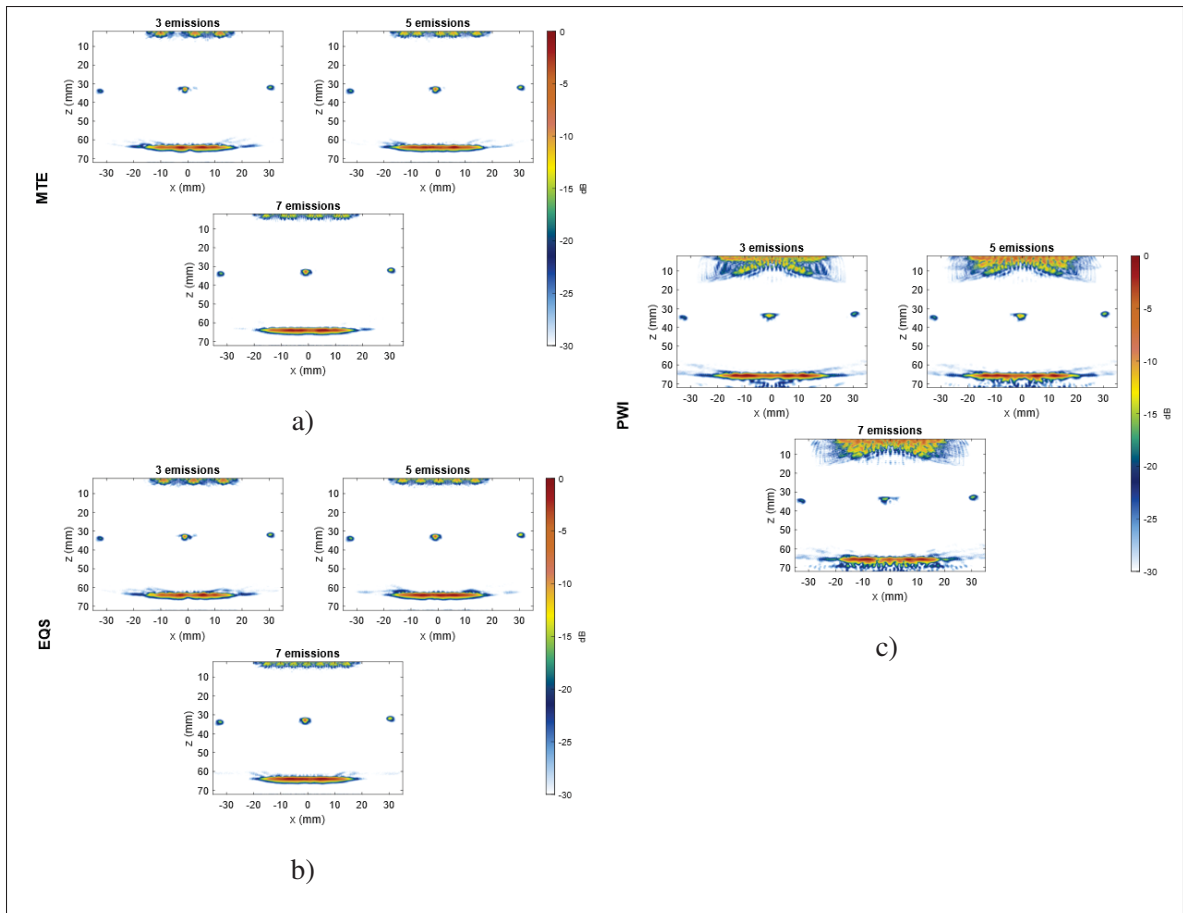
Figure 2.11   Experimental ultrasonic images of HPO according to emission
events: (a) MTE, (b) EQS, and (c) PWI

The MTE on this occasion also yielded a performance closer to FMC. The graphs present a triangular shape, with the center defect showing a higher amplitude, and therefore, a higher CNR. The SDH 4 also has a higher CNR as compared to SDH 2, due to the difference in ultrasonic energy transmitted in their respective location. Also, the resolution of SDH 3 is greater than that of the other two SDHs analyzed, presenting the smallest API value. The defects in HPO are located at a maximum depth of 29 mm, and thus are in perfect agreement with VPO results. For VPO, the defects closer to the surface presented better CNR and API performances (see Figs. 2.9 and 2.10). In that case, both the CNR and API are better for all cases over 3 firing events, when comparing the sparse approaches with PWI.
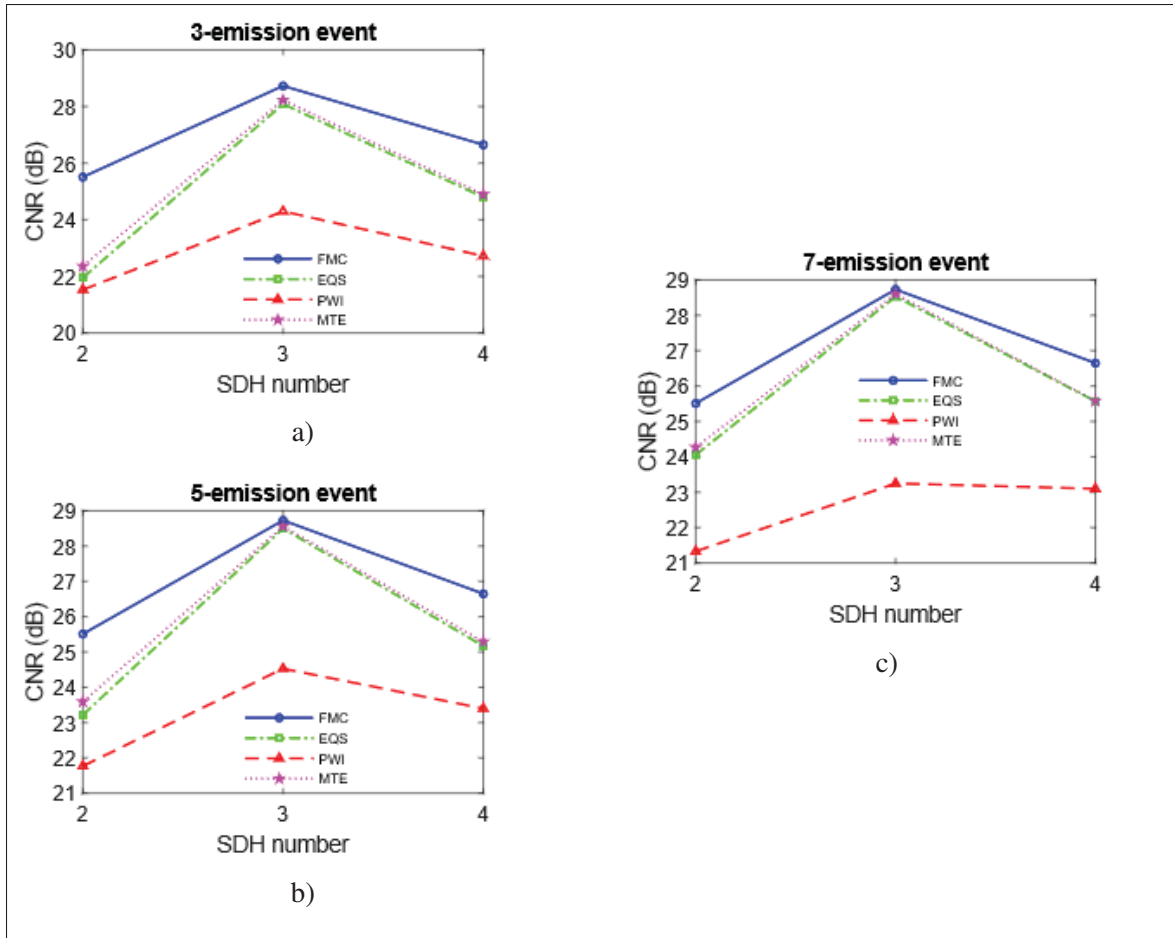
Figure 2.12   CNR curves HPO comparing FMC, EQS, PWI and MTE for emission events equal to: (a) $N_e = 3$, (b) $N_e = 5$ and (c) $N_e = 7$

Following the comparison, it can be seen that the proposed sparse- TFM approach (MTE) yields an overall better performance than the PWI. The SLL of PWI is high and its main lobe width is considerably wider, as reported in previous work (Guo, Wang, Wu & Yu, 2018). Furthermore, non-uniform piezo elements happen to introduce more noise than expected if the plane wavefront is not the ideal or the elements are not transmitting at the same amplitude. Thus, the difference shown in this study could be also explained with the non-uniformity of the piezo elements inside the probe. According to the results presented for VPO and HPO, increasing N_e brings the MTE performance closer to that of the FMC-TFM in terms of both CNR and API, but significantly fewer data. This can be attributed to the fact that the FMC presents some redundancy in data
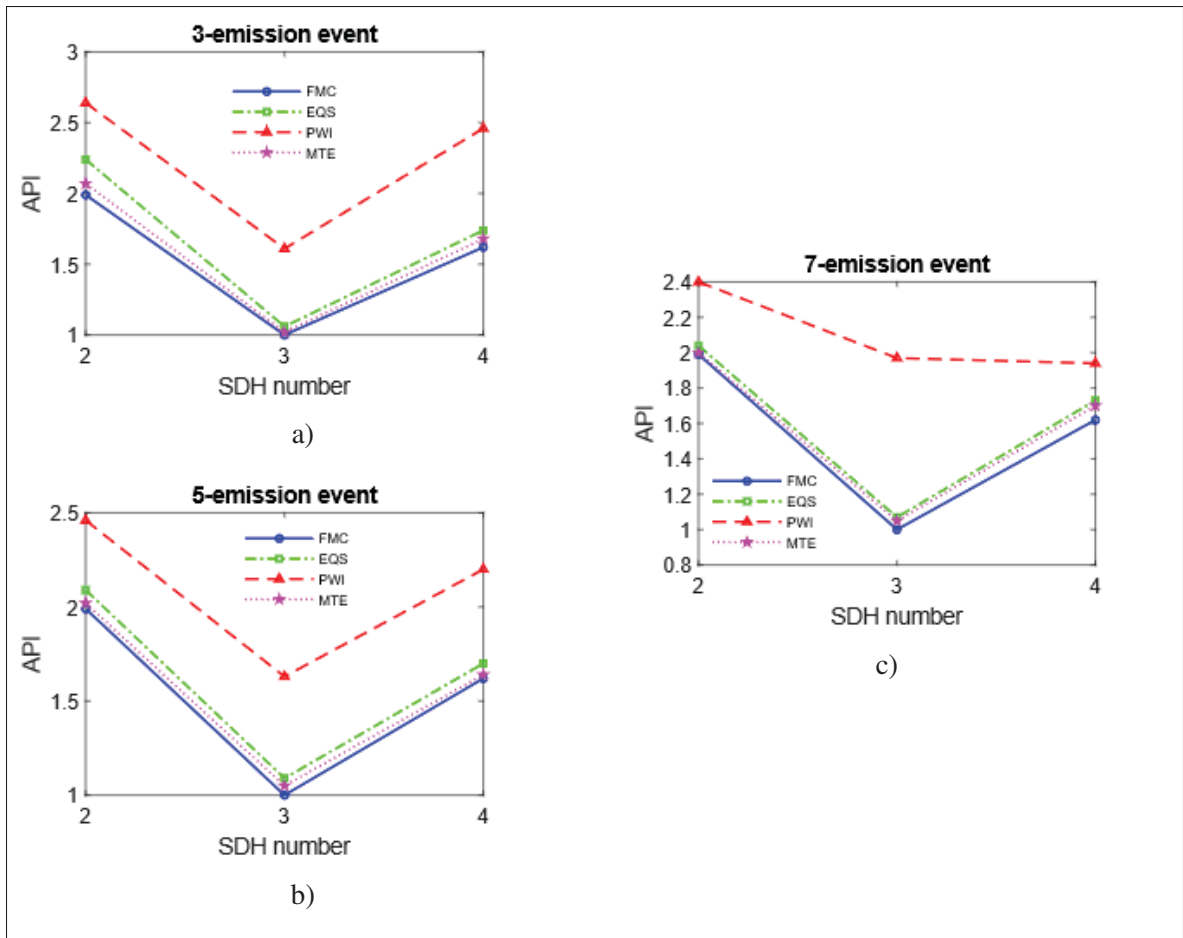
Figure 2.13   API curves HPO comparing FMC, EQS, PWI and MTE for emission events equal to: (a) $N_e = 3$, (b) $N_e = 5$ and (c) $N_e = 7$

(Karaman, Wygant, Oralkan & Khuri−Yakub, 2009). The small difference between the results of the sparse approaches can be explained by verifying the MLW and SLL from their BP. Table 2.2 contains the EQS MLW and SLL results.

Table 2.2   EQS (periodic sparse layout) results of MLW and SLL for each N_e value

Number of active elements (N_e)	Periodic sparse layout	MLW (°)	SLL (dB)
3	[18 36 54]	1.86	-20.80
5	[11 22 33 44 55]	1.82	-25.57
7	[8 16 24 32 40 48 56]	1.80	-26.78

For instance, the periodic sparse layout of 5 emission-events presents almost the same MLW as MTE (see Table 2.1), and an SLL around 1 dB higher. This is reflected in the imaging performance, as it makes the API and CNR results to be very close. In some cases, there is a difference of only 0.1 dB in CNR, but nevertheless, MTE overcomes the periodic layout in all scenarios.

In order to analyze the acceleration of the ultrasonic imaging process when using fewer emissions, the computation times of the methods used were measured and compared. The time required for the FMC-TFM imaging is used as the standard for each block position. Then, a variation is calculated to estimate the time reduction. The computation time variation (Δt) of the three acquisition methods used concerning the number of emissions and block position is found listed in Table 2.3.

Table 2.3   Variations of the computation time of MTE, EQS, and PWI compared to FMC according to the number of emissions used for each block position

| Number of emissions | Computation time variation Δt (%) | | | | | |
| | VPO | | | HPO | | |
	MTE	EQS	PWI	MTE	EQS	PWI
1	91	90	94	-	-	-
3	88	88	88	91	91	90
5	85	83	83	89	89	86
7	82	81	77	87	87	81

As shown in Table 2.3, reducing the number of emissions to 7 or fewer leads to an average reduction of 86% of the imaging time compared to the FMC. This means that the MTE with 5 emission events would take only 1.51 s to image the same ROI of an FMC-TFM with 10 s of computation time (85% of reduction, see Table 2.3). The Δt values of MTE for both block orientations showed a higher percentage reduction compared to EQS and PWI, except for the single emission event of VPO. The Δt of EQS, however, presented the same variation in some cases or only a small difference of 1 or 2% against the MTE. Nevertheless, the MTE granted a faster imaging process compared to the others.

The percentage variance (Δ%) between MTE and the FMC can be used as a tool to find a compromise between image quality and the number of firings. To calculate Δ%, the following equation is applied:

$$\Delta\% = \frac{P_{MTE} - P_{FMC}}{P_{FMC}} \tag{2.12}$$

where P_{MTE} and P_{FMC} are the values of API or CNR parameters from MTE and FMC, respectively. Thus, Δ% is computed for all SDHs analyzed herein. For the sake of brevity, only the percentage variance of SDH 3 for both VPO and HPO are displayed in Figs. 2.14 and 2.15. It can be seen that the difference between the percentual values going beyond the 5-emission event was not bigger. For VPO, the difference was around 2% for CNR and 1% for API (Fig. 2.14 (a) and (b)). The HPO presented a difference of 0.3% for CNR, and 3% for API (Fig. 2.15 (a) and (b). Also, the amount of data to be processed, as well as the number of combinations to be explored using the MTE approach for 7 emissions must be considered. Therefore, $N_e = 5$ can be said to represent a better trade-off over the other scenarios. In this case, it allows working with reduced data (just 7.8% of the FMC) while maintaining a satisfactory performance.
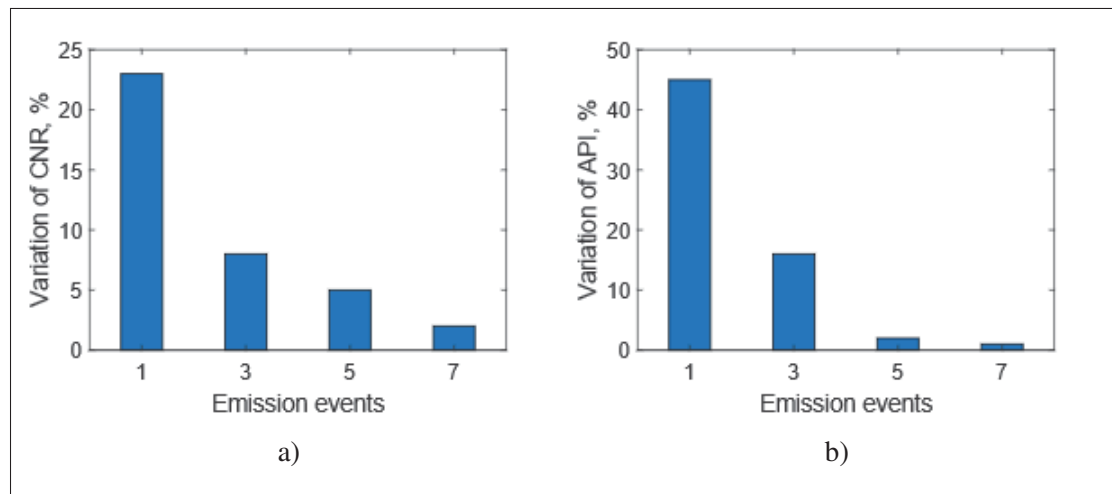
Figure 2.14   Percentual variance between FMC and MTE for VPO in terms of (a) CNR and (b) API
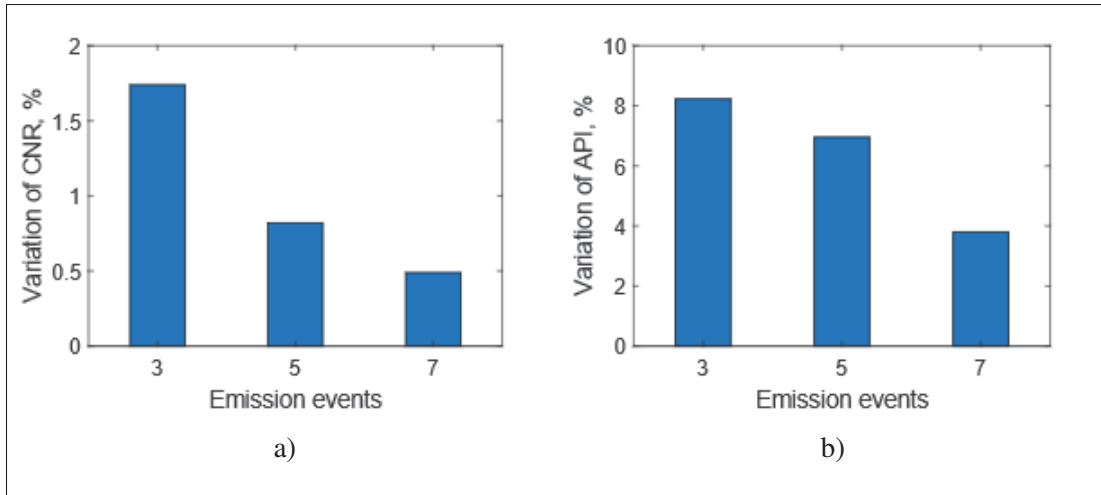
Figure 2.15   Percentual variance between FMC and MTE for HPO in terms
of (a) CNR and (b) API

Another quantitative evaluation is done regarding the position and size accuracy of the SDHs for the proposed sparse approach in contrast to the FMC, and the actual block inspected. Each SDH was evaluated separately and according to the block orientation (VPO and HPO). Assuming that the SDH behaves like a perfect rounded reflector, the echoes reflecting on the top of the SDH corresponds to the maximum intensity pixel on the images and therefore were used for positioning estimation. When sizing, the direction parallel to the ultrasonic beam is not considered as it relates the dimension of the defect to the pulse width instead of its size (Felice & Fan, 2018). Thus, only the perpendicular direction was used for flaw sizing with the 6 dB drop method. Fig. 2.16 (a) and (b) shows the transverse distribution of the SDH 3 in VPO for FMC and MTE images, respectively. The pixel interval is 0.01 mm.

A percentage variance was also computed in this case, comparing MTE with the FMC image and the actual block measurements. Table 2.4 contains the percentage variance values for VPO and Table 2.5 present the ones for HPO. The suffixes x, z, and s represent the defect position in the x-axis, the defect position in the z-axis, and the size, respectively.

Despite the considerable reduction of emission events, there was no significant variance in flaw position (see Δx and Δz values in Tables 2.4 and 2.5). The values compared to FMC did not
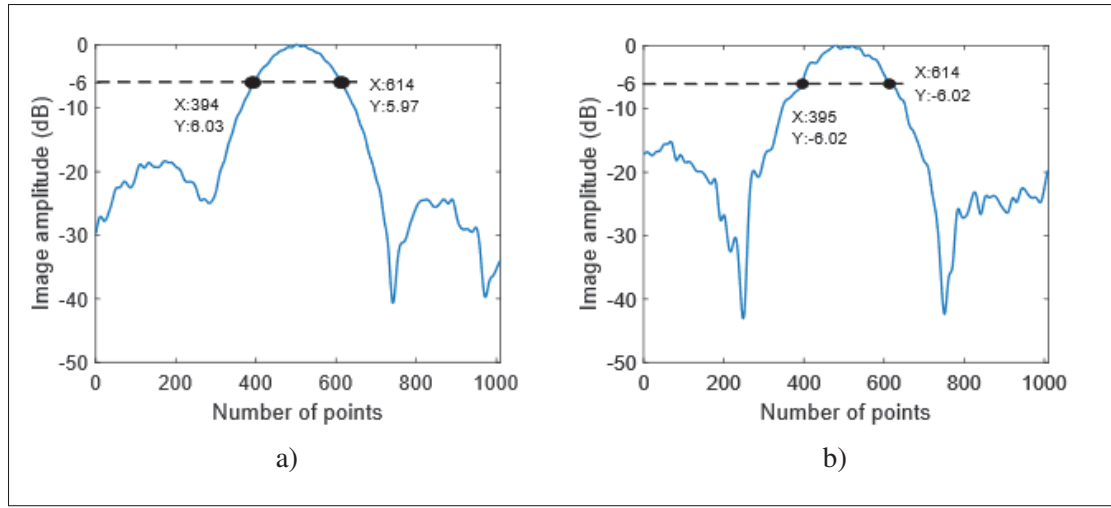
Figure 2.16   Percentual variance between FMC and MTE for HPO in terms
of (a) CNR and (b) API

Table 2.4   Percentage variance of MTE with respect to FMC
and the block for each SDH of VPO

| | Values of Δ (Δx, Δz and Δs) for VPO | | | | | |
| | MTE/FMC | | | MTE/Actual Block | | |
SDH number	Δx (%)	Δz (%)	Δs (%)	Δx (%)	Δz (%)	Δs (%)
2	1	0	7	1	5	71
3	1	0	0	1	3	119
4	0	0	5	0	1	211
5	0	0	4	1	1	268

Table 2.5   Percentage variance of MTE with respect to FMC
and the block for each SDH of HPO

| | Values of Δ (Δx, Δz and Δs) for HPO | | | | | |
| | MTE/FMC | | | MTE/Actual Block | | |
SDH number	Δx (%)	Δz (%)	Δs (%)	Δx (%)	Δz (%)	Δs (%)
2	0	0	14	5	5	147
3	0	1	8	1	4	25
4	0	0	17	2	5	160

exceed 1% and were not greater than 5% for the actual block in both orientations. For sizing, the actual diameter of the defect (1 mm) was used as standard, and the diameter of the image flaw was estimated using the 6 dB drop method. Therefore, when Δs is equal to 71% as the case of SDH 2 in VPO, means that the size of the flaw is 1.58 mm in the image. As expected, the effects of the ultrasonic wave spreading are causing the image defect to stretch, degrading the lateral resolution. This is more apparent with increasing depth. Therefore, Δs starts to increase (see Table 2.4). This effect can be observed even for FMC-TFM. However, the variation for the MTE approach was not significant. In comparison with the FMC, the sizing variation was within 7% for VPO. On the other hand, the SDH 3 in the HPO showed smaller size variation about SDH 2 and 3 by being under the probe's aperture. The same effect was observed for HPO comparing SDH 2, 3, and 4 with the actual block.

Figs. 2.17 and 2.18 display the results for MTE and EQS with $N_e = 5$ for visual comparison. The sparse configuration of the elements from the probe is also shown in a schematic (Fig. 2.17 (a) and 2.18 (a)). It can be seen that a marginal gain is achieved by using the optimal layout (MTE), as compared to the equally spaced sparse array for both VPO and HPO. The EQS, however, does not require running the algorithm to provide similar results (around 9% of the MTE for VPO, and 4% for HPO). Moreover, the MTE layout appears similar to that of the EQS, with a random change of ± 1 or 2 elements. Therefore, breaking the symmetry of the EQS layout leads to marginal gains.

2.5   Conclusion

This work presented a simplified approach to design the optimal sparse layout of an array in the context of reduced transmission events. A comparative study between two different sparse array layouts and PWI was done in terms of CNR and API. The proposed method for designing the best sparse array from section 2.3.1.2 (MTE) presented an overall better performance as compared to PWI and the periodic sparse array for axial and lateral defects. This was explained by comparing the beam pattern features of PWI, and by the non-uniformity of the plane wavefront that the probe might generate in the case of the PWI. The outperformance of the MTE in comparison

to the sparse periodic arrangement (EQS) was due to a difference of 1 dB in SLL. Based on the percentage variance, it was found that the MTE approach using $N_e = 5$ (92.2% reduction in firing events) represents a good trade-off over the other emission events. In this case, the images produced are comparable to those of the FMC-TFM in terms of CNR and API but obtained using just 7.8% of FMC data. On the other hand, an equally spaced layout with 5 firings produced results within 9% of the optimal layout without requiring computations. Therefore, the method presented herein has been demonstrated to be an effective way to improve TFM productivity and can be extended to industrial applications of ultrasonic phased arrays.
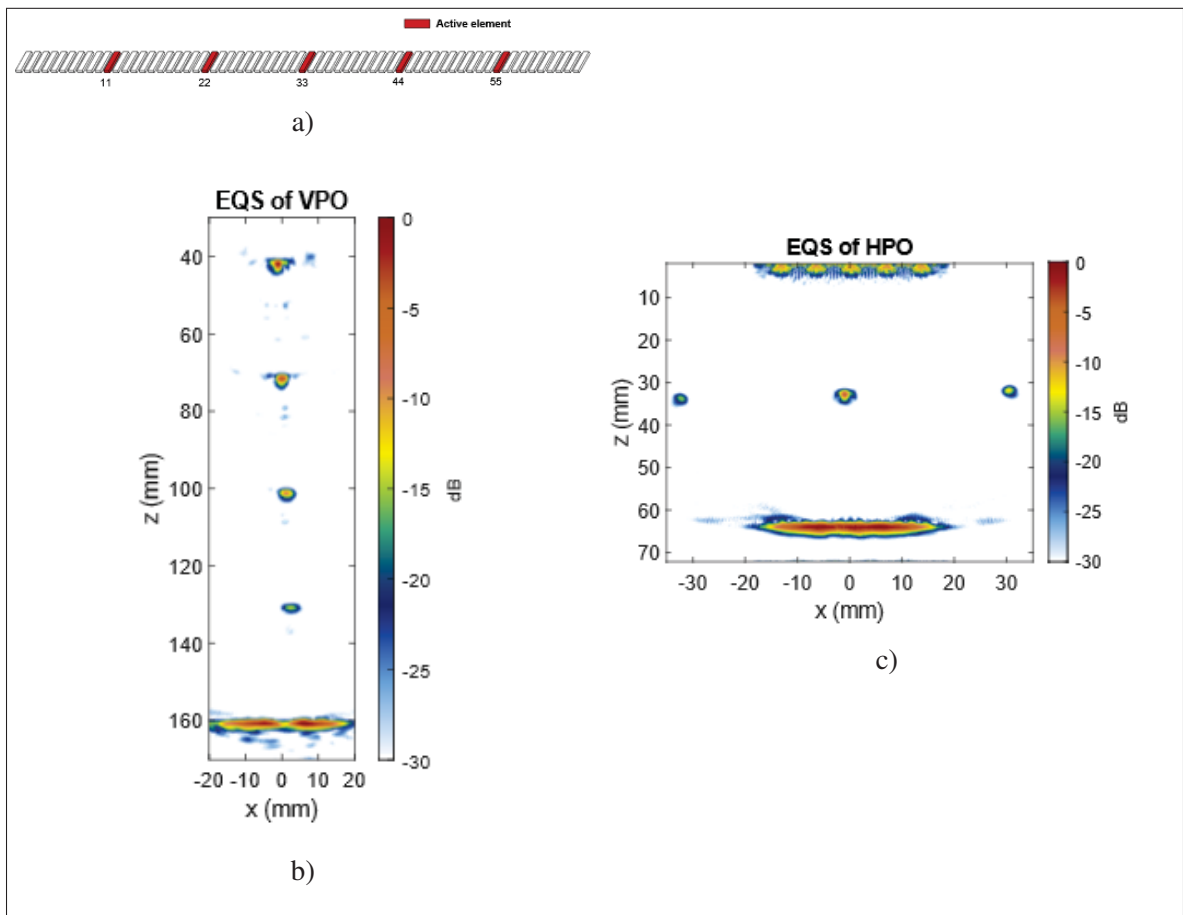
Figure 2.17   EQS experimental results: (a) Equally spaced elements with edge element deactivation layout, and EQS image with $N_e = 5$ for (b) VPO and (c) HPO
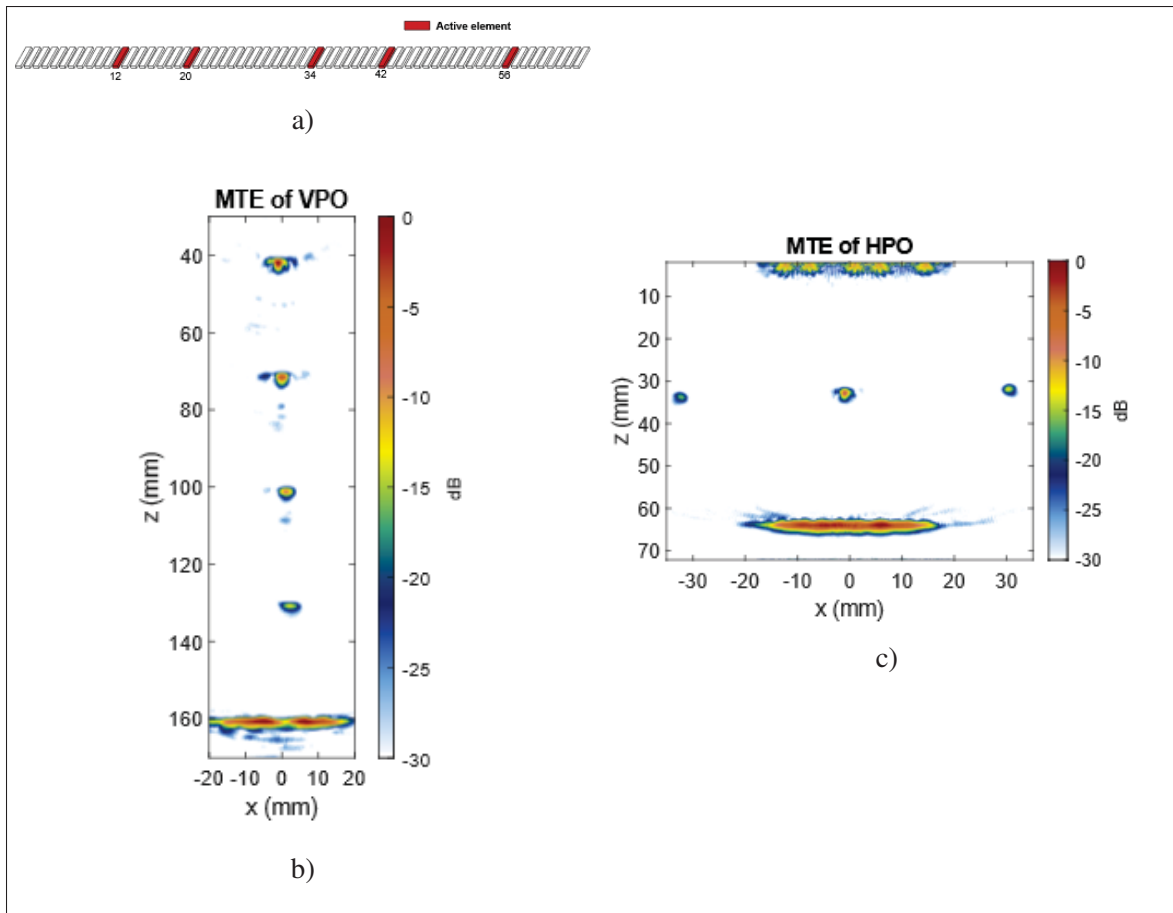
Figure 2.18   Best sparse array experimental results: (a) MTE approach element layout, and MTE image with $N_e = 5$ for (b) VPO and (c) HPO

CHAPTER 3

FAST 3-D TFM ULTRASONIC IMAGING USING WIDEBAND 2-D SPARSE ARRAY OPTIMIZATION

Lucas Pereira Piedade[1] , Guillaume Painchaud-April[2] , Alain Le Duff[2] , Pierre Bélanger[1]

[1] PULETS, Department of Mechanical Engineering, École de Technologie Supérieure,
1100 Notre-Dame Ouest, Montréal, Québec, Canada H3C 1K3
[2] Evident Industrial, 3415 Rue Pierre-Ardouin, Québec, Québec, Canada G1P 0B3

3.1 Abstract

Three-dimensional ultrasonic imaging using a matrix phased array is of increasing interest in the nondestructive testing (NDT) field due to its capacity to provide volumetric information of the inspected medium. However, industrial adoption of this technology is limited compared to linear arrays due to challenges such as substantial data collection and the complexity caused by the numerous piezoelectric elements. Full matrix captures (FMC) become prohibitive and implementing the volumetric total focusing method (TFM) imaging necessitates increased calculations, rendering real-time applications impractical without high-end instruments. This paper presents the minimum firing event method as an efficient way to design 2-D sparse arrays under wideband conditions for fast 3-D TFM. This approach aims to operate with a limited number of firing events while maintaining image quality and high volume rates. The process involves establishing a simplified algorithm for designing wideband 2-D sparse arrays. Different configurations with varying active elements in transmission are tested to find the optimized sparse array pattern. In the end, the optimal sparse layout balances acoustic performance and firing events. The proposed method was tested experimentally using samples containing artificial flaws with an 11×11 matrix array centered at 3 MHz. The images were then compared in terms of contrast-to-noise ratio (CNR) and the measured defect sizes. It was shown that the 2-D sparse array approach was able to improve 3-D TFM productivity by 9.8 times without a significant loss of image quality or defect size accuracy, offering a promising solution for practical implementation in industrial NDT applications.

3.2   Introduction

The advent of ultrasonic matrix phased arrays (2-D arrays) capable of providing volumetric information of the inspected medium has opened new possibilities for nondestructive testing (NDT) inspections. A volumetric image represents a better possibility to assess actual defects of engineering structures, especially those with arbitrary shapes and orientations (Felice & Fan, 2018). Despite the clear imaging potential, there has been minimal industrial adoption of 2-D arrays in NDT applications in contrast with conventional one-dimensional (1-D) linear probes and associated 2-D imaging methods (Drinkwater & Wilcox, 2006). Imaging operations using linear arrays frequently utilize full matrix captures (FMC) in conjunction with delay-and-sum (DAS) imaging algorithms, such as the total focusing method (TFM) (Holmes *et al.*, 2005). This approach is commonly chosen due to its superior image quality for defect assessment, as noted in (Fan *et al.*, 2014; Zhang, Drinkwater & Wilcox, 2013), and is readily accessible on various commercial phased array controllers. Furthermore, real-time processing of this operation with linear arrays is also feasible (Lewandowski, Walczak, Witek, Rozbicki & Steifer, 2018; Sutcliffe *et al.*, 2012). On the other hand, matrix phased array transducers are usually denser, as the piezoelectric elements follow a 2-D pattern. This leads to a high number of channels and therefore a considerable amount of collected data. The utilization of FMC becomes impractical due to the associated time constraints, and implementing volumetric TFM imaging becomes extremely heavy. The number of focal points in the volume of interest (VOI), and the large amount of data to be processed are currently obstacles to faster 3-D TFM imaging. This restricts real-time usage to high-end instruments. Hence, addressing these challenges is vital for enhancing the widespread use of three-dimensional ultrasonic imaging using 2-D arrays.

To tackle these limitations, sparse array techniques can be implemented (Austeng & Holm, 2002; Moreau *et al.*, 2009). The sparse array approach consists of using only a few active elements in transmission, while the entire array is used in reception. Therefore, the sparsity of the 2-D array contributes to reducing data collection and processing times. There are also other acquisition strategies, such as plane wave imaging (PWI) (Le Jeune *et al.*, 2016), that have been suggested as an alternative to improve efficiency. PWI offers the potential to enhance frame rates by

reducing the required number of firings. However, utilizing PWI demands compounding several plane waves to achieve resolutions comparable to those of TFM images (Couture, Fink & Tanter, 2012; Montaldo *et al.*, 2009), consequently decreasing frame rates. More recently, Marmonier et al.(Marmonier, Robert, Laurent & Prada, 2022) implemented TFM in the Fourier domain for real-time 3-D imaging, named k-TFM, and were able to achieve a frame rate 4 times higher compared to time-domain TFM. Nevertheless, sparse arrays still represent a relatively cheap and efficient approach for fast 3-D imaging, and their design remains an actively evolving research area.

Most sparse array approaches are based on optimization using stochastic algorithms under narrowband conditions (Trucco, 1999; Austeng & Holm, 2002; Diarra *et al.*, 2013; Hu *et al.*, 2017). In this condition, the array beam pattern (BP) can be approximated to a narrowband BP in the far field, where the elements are reduced to point sources transmitting monochromatic waves at the transducer central frequency. Then, stochastic optimization methods such as genetic algorithms (GA) (Austeng *et al.*, 1997; Hu *et al.*, 2017) or simulated annealing (SA) (Trucco, 1999; Roux *et al.*, 2018) are used in the search for the optimal sparse layout. The design is chosen based on BP characteristics for imaging, i.e., reduced side lobe levels (SLL) and a narrow main lobe width (MLW). Alternatively, wideband signals can provide a more realistic analysis but at a higher computational cost. Because of that, this approach is scarcely reported in the ultrasound literature (Roux *et al.*, 2017; Sciallero & Trucco, 2021), and notably, this avenue remains unexplored in NDT research. In (Roux *et al.*, 2017), Roux et al. introduced a wideband sparse array optimization process using SA combined with multi-depth energy functions and were able to reduce 75% of the active elements. Additionally, Sciallero and Trucco (Sciallero & Trucco, 2021) recently proposed a method involving wideband 2-D sparse array optimization along with multiline reception, achieving enhanced volume rate imaging. Even though stochastic optimization algorithms were successfully implemented for both narrow and wideband conditions, using such algorithms is complex due to the challenge of appropriately setting parameters and designing precise objective functions.

This study introduces an original 2-D sparse array method with the objective of enhancing the productivity of 3-D TFM by minimizing firing events. The proposed approach termed the "minimum firing event method", was initially presented by the authors in (Piedade, Painchaud-April, Le Duff & Bélanger, 2022) for designing sparse linear arrays using narrowband BP. This design approach involved exhaustive exploration of all possible array combinations, computed from a predefined minimum number of active elements. In this paper, we expand and refine this method to effectively design 2-D sparse arrays using wideband simulation. Various numbers of active elements are tested, with configurations corresponding to less than 5% of the complete array. Still, the exploration of the entire combination set becomes a large-scale problem for the case of 2-D arrays, and thus, managing the amount of candidate solutions incurs significant computation time and memory requirements. To mitigate this, an intermediary step was implemented, involving the elimination of symmetrical layouts and the incorporation of additional spatial constraints to further reduce combinations without affecting the final solution. This modification aims to reduce the computation load and make this approach viable for wideband analysis. By reducing the number of available combinations, the exploration time was managed effectively, eliminating the need for sophisticated optimization algorithms and enabling the utilization of a streamlined approach. The optimal array layout represents the best acoustic performance with the full array as a reference. An experimental evaluation was conducted on the suggested method, quantitatively comparing the TFM image quality from the sparse array approach and FMC, as well as their corresponding image formation times. The influence of the sparsification on defect sizing was also assessed.

The paper is organized as follows. Section 3.3 provides a comprehensive overview of the materials and methods used, including the experimental setups, the fundamentals of the 3-D TFM imaging algorithm, the adopted 2-D sparse array approach, and the evaluation metrics used. Section 3.4 contains the presentation of the experimental findings and a corresponding discussion. Concluding remarks are provided in Section 3.5.

3.3   Materials and methods

3.3.1   Experimental setups

Experiments were conducted using two distinct experimental setups to evaluate the proposed sparse array method. The first setup consisted of side-drilled holes (SDHs) positioned at varying depths within an aluminum block. In contrast, the second setup involved a low-carbon steel part with several electrical discharge machined (EDM) notches. It should be noted that these setups were designed with a high level of generality, enabling the findings from this study to be extrapolated to encompass other materials and types of flaws. Measurements were executed using an EVIDENT ultrasonic matrix phased array probe 3M11X11-I (manufactured by EVIDENT Industrial, State College, PA, USA). This probe comprises an array of 11×11 square elements operating at a central frequency of 3 MHz, arranged with a pitch of 1 mm along both the x- and y-directions. In the first setup, this matrix probe was positioned in direct contact with the top face of the aluminum block. Fig. 3.1 illustrates the inspection setup, the delineation of the VOI, and the block's dimensions. The longitudinal sound velocity measured in the block was 6354 m/s. For the second setup, a 19.05-mm-thick plate specimen made of low-carbon steel was used, featuring EDM notches with a width of 0.3 mm. These notches were positioned at various angles, either centered within the plate or as a surface-breaking profile at its back wall (Fig. 3.2). This article exclusively presents the results related to notches B1 (90°) and C3 (70°). The measurements were performed using the same matrix array probe utilized in the first setup, mounted on a rexolite wedge (EVIDENT SA32-N55S). The probe was placed on the side of each notch, simulating a weld bevel scanning orientation. The measured values of longitudinal and shear sound velocity in this plate were 5953 m/s and 3243 m/s, respectively. In both experimental configurations, the matrix probe was interfaced with a Verasonics Vantage-64 LE acquisition system, and an FMC acquisition was executed for each case with a sampling rate of 62.5 MHz. Subsequently, the acquired data were subjected to post-processing in MATLAB using the DAS method to generate volumetric TFM images, with a cubic pixel grid of 0.10 mm.
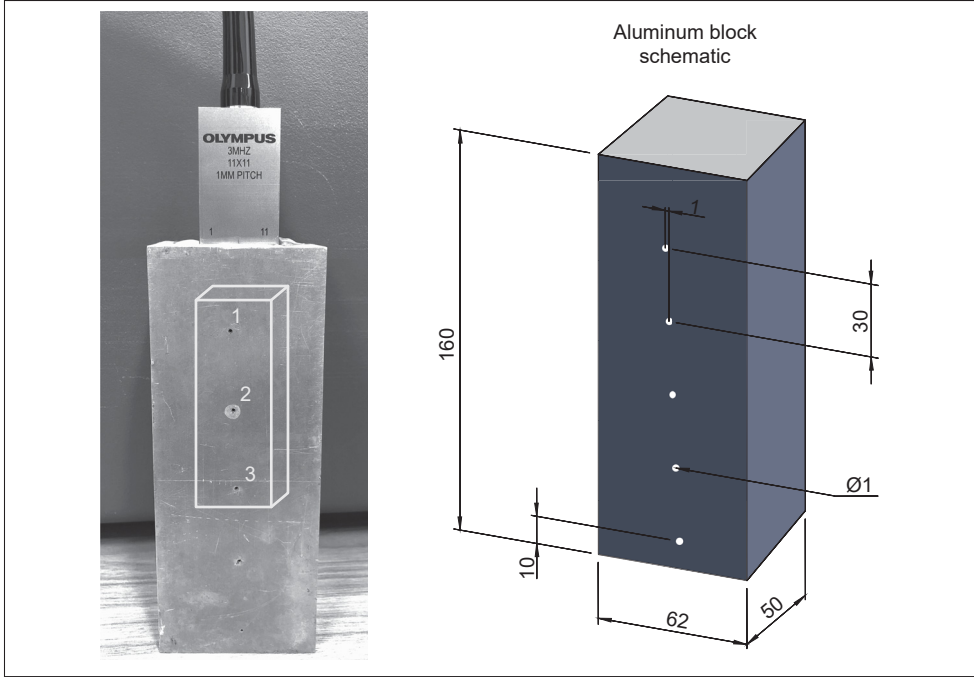
Figure 3.1   Experimental Setup 1: 3M11X11-I ultrasonic matrix probe placed in contact and the VOI used encompassing SDHs 1 to 3. Dimensions of the block are provided in the schematic

3.3.2   3-D Total focusing method (TFM)

FMC data collection using ultrasonic phased array transducers consists of individual elements sequentially transmitting while the full aperture receives. Post-processing this resulting data with the 3-D TFM imaging algorithm enables the creation of high-resolution 3-D images. This is achieved by considering individual time-of-flight (TOF) delays for each array element at every point within the VOI and coherently summing the delayed signals. Therefore, the resulting volumetric image intensity $I(x, y, z)$ can be computed as follows:

$$I(x, y, z) = \left| \sum_{T=1}^{N_M} \sum_{R=1}^{N_M} H\left(S_{TR}\left(t_{TR}\left(x, y, z\right)\right)\right) \right| \tag{3.1}$$

where N_M represents the total count of matrix array elements, t_{TR} is the TOF, corresponding to the time it takes for the ultrasonic wave to travel from the transmitter (T) to the desired voxel
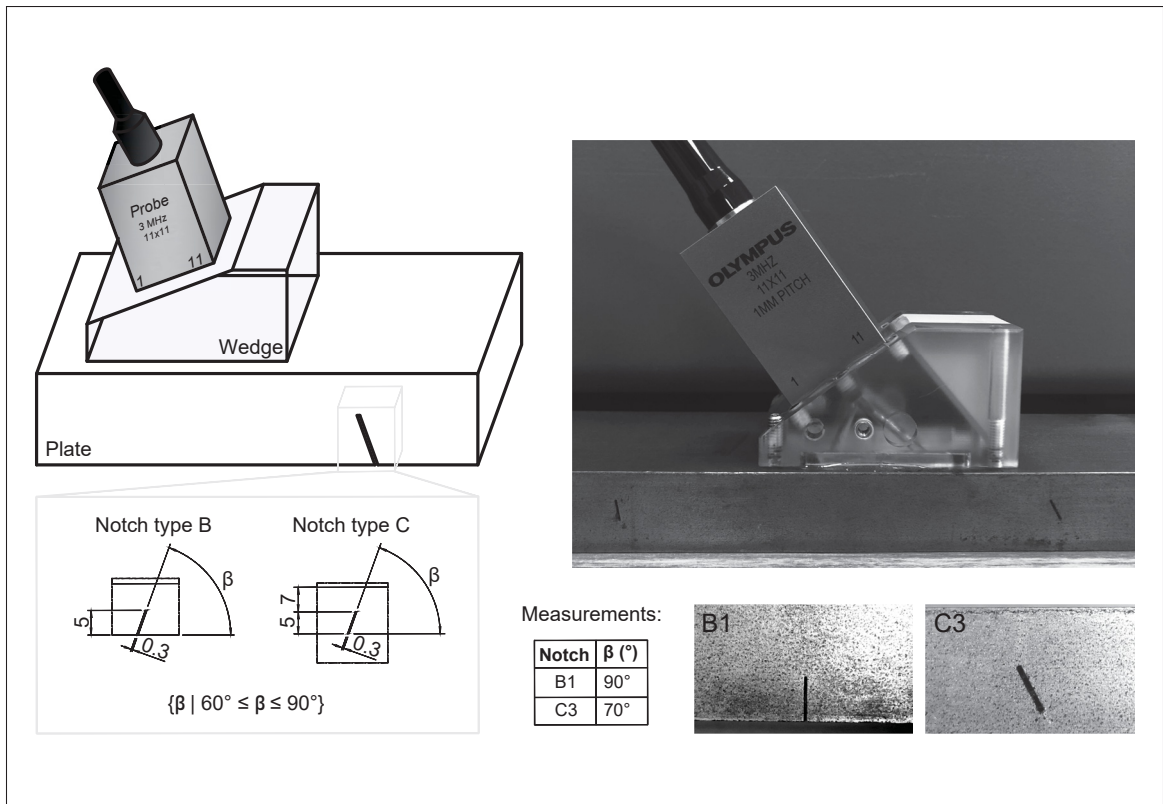
Figure 3.2   Experimental Setup 2: 3M11X11-I ultrasonic matrix probe mounted on a wedge. Schematics for the notch profiles are shown. The experimental setup and the notches considered in this study (B1 and C3) are presented in the pictures

point (P) and then to return to the receiver (R), S_{TR} denotes the time-amplitude signal from the matched transmitter-receiver pair, and H stands for the Hilbert transform. In the case of imaging a single medium, determining t_{TR} is a straightforward procedure using elementary trigonometric principles and the medium longitudinal sound velocity, according to:

$$I(x, y, z) = \left| \sum_{T=1}^{N_M} \sum_{R=1}^{N_M} H \left(S_{TR} \left(\frac{\|E_T - P\| + \|E_R - P\|}{c_2} \right) \right) \right| \tag{3.2}$$

where c_2 is the longitudinal sound velocity of the medium and $\|\cdot\|$ represents the Euclidian norm. An example ray's path within a single medium is depicted in Fig. 3.3, traveling from the transmitting element (E_T) to the image voxel point (P) and then to the receiving element (E_R). This path comprises two distinct routes, each representing a section of the ray's trajectory

between two points. In this process, only c_2 is necessary to compute the TOF, and the points E_T, P, and E_R represent position vectors in this computation.
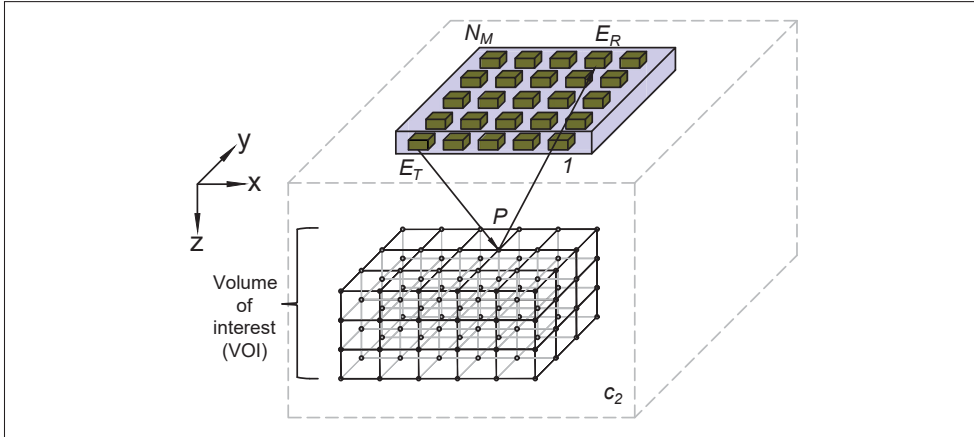
Figure 3.3   Illustration of the 3-D TFM imaging procedure for a ray path in a single medium. The ultrasonic wave travels between the points E_T, P, and E_R, which are position vectors in the image according to the XYZ coordinate system
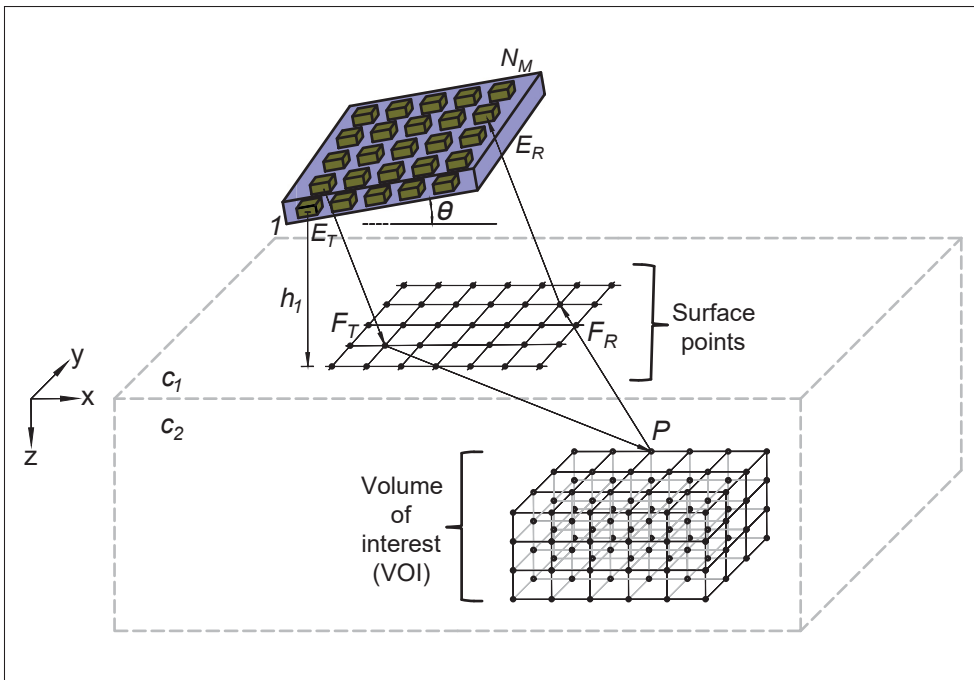
Figure 3.4   3-D TFM in dual media showing a ray path correspondent to the minimum TOF between E_T, P, and E_R and the respective surface-crossing points

While TFM provides exceptional imaging capabilities, using this algorithm for volumetric imaging comes at the cost of increased computational requirements, as can be seen in Eq. 3.2. 3-D imaging involves a larger amount of data compared to 2-D imaging, as the element count of matrix arrays is usually much greater than in linear arrays, N_L ($N_M >> N_L$). The number of focal points present in the 3-D image volume is also notably higher than in its 2-D counterpart, often exceeding it by 2 degrees of magnitude. Moreover, attempting a direct extension of FMC to matrix arrays is not realistic due to the excessive number of required firing events, and consequently low volume rate. In situations involving dual media inspections (McKee, Bevan, Wilcox & Malkin, 2020; Cosarinsky, Cruza, Muñoz & Camacho, 2023), such as immersion and phased array wedge testing, the need for extra ultrasound paths and the increased complexity of TOF calculations further restrict the practical application of volumetric TFM. Fig. 3.4 shows a matrix phased array inspection in dual media. The probe is inclined at an angle, θ, relative to the x-axis, with the first column of the array raised to a certain height, h_1, resembling setup 2 with a wedge. To simplify visualization, the schematic omits the wedge, assuming uniform properties above the dashed line. In this case, the computation of TOF is more complicated, and the solution consists of applying Fermat's principle, which identifies the two surface-crossing points that result in the lowest TOF between the pair of elements and each point in the image. This path is shown in Fig. 3.4 and now the ultrasonic wave velocity in the first medium, c_1, must also be considered. Hence, the TOF computation is expressed as:

$$t_{TR}(x, y, z) = \frac{\|E_T - F_T\| + \|F_R - E_R\|}{c_1} + \frac{\|F_T - P\| + \|P - F_R\|}{c_2} \tag{3.3}$$

where F_T and F_R are the surface-crossing point locations in transmission and reception, respectively. One can see that, in this context, the application of volumetric TFM imaging is further complicated and also time-consuming.

A potential solution involves the use of sparse array techniques, aiming to reduce the firing event count while maintaining similar imaging performance to the full array. In this work, FMC data was collected and post-processed to create synthetic sparse array data. The choice of sparse

active firing elements (N_S), e.g., 4 out of 121 elements with all elements used in reception, leads to the selection of a sparse data matrix, which corresponds to a subset of the original FMC. This subset employs the $N_S \times N_M$ dataset instead of the $N_M \times N_M$ FMC matrix, therefore resulting in faster data collection and postprocessing. A detailed explanation of the procedure for designing a 2-D sparse array is provided in the next section.

3.3.3 2-D sparse array designing method

To obtain the ideal 2-D sparse array configuration, the minimum firing event method based on pulse-echo 3-D point spread function (PSF) simulations is proposed. This two-way PSF characterizes how the array responds to a point reflector, essentially indicating the array's imaging capabilities (Drinkwater & Wilcox, 2006; Mansur Rodrigues Filho & Bélanger, 2021; Li & Chi, 2018), and was therefore the approach chosen as an assessment tool in sparse array design. The PSF calculation was carried out using time-domain signals, modeling the ultrasonic matrix phased array from section 3.3.1 placed in direct contact for simplification. For every combination of E_T and E_R in the ultrasonic array, the response of the signal induced by an internal point reflector can be predicted. This point was positioned at the array's center and lies in the middle of a 20 mm cubic VOI placed 30 mm deep under the probe. Then, a 5-cycle Hann windowed toneburst centered at 3 MHz, representing the ultrasonic signal, $s_{TR}(t)$, is delayed by the TOFs computed as described in section 3.3.2. The PSF formulation is done in the frequency domain, and therefore, the frequency spectrum, $\widehat{s}_{TR}(\omega)$, from the ultrasonic signal is then obtained using the Fourier transform. Subsequently, to address the energy loss due to both beam spreading and attenuation, $\widehat{s}_{TR}(\omega)$ undergoes multiplication by the geometric attenuation and element directivity coefficients as follows (Schmerr Jr, 2014):

$$\widehat{S}_{TR}(\omega) = \widehat{s}_{TR}(\omega) \cdot A_T \cdot D_T \cdot A_R \cdot D_R \tag{3.4}$$

where $\widehat{S}_{TR}(\omega)$ is the estimated spectrum, A_T and A_R denote the geometric attenuation, and D_T and D_R are the element directivities, where the subscripts T and R refer to the transmit and

receive elements, respectively. Considering the reciprocity of the transmitting and receiving processes, only one "leg" is required to be computed in this process. Therefore, the attenuation coefficient, A_i, can be estimated by:

$$A_i = \frac{1}{\|E_i - P\|}.$$

(3.5)

The element directivity is:

$$D_i = \text{sinc}\left(\frac{\pi a \ \sin\theta_i \ \cos\phi_i}{\lambda}\right) \text{sinc}\left(\frac{\pi a \ \sin\theta_i \ \sin\phi_i}{\lambda}\right)$$

(3.6)

where λ is the wavelength of the ultrasonic wave in the medium, a is the width of the square piezo element, and θ and ϕ are the elevation and azimuth angles respectively. In both Eq. 3.5 and 3.6, the subscript i represents the transmitting or the receiving process. Following this initial processing, the subsequent step involves applying the complex Hilbert transform to $\widehat{S}_{TR}(\omega)$ obtaining the resulting time-domain signal, denoted as $H_{TR}(t)$, as indicated in ref. (Holmes *et al.*, 2005). Hence, after completing this procedure for all the transmitter-receiver pairs, a synthetic $N_M \times N_M$ FMC matrix is created. This FMC matrix is then used to obtain a 3-D TFM image, or in this case, the PSF of the imaging system:

$$PSF(x, y, z) = \left|\sum_{T=1}^{N_M} \sum_{R=1}^{N_M} H_{TR}\left(\frac{\|E_T - P\| + \|E_R - P\|}{c_2}\right)\right|.$$

(3.7)

The 3-D PSF analysis consists of selecting the maximum voxel intensity, from which the 2-D image slices of the XZ and YZ planes are used to extract SLL and MLW values using peak search methods. The proposed 3-D PSF analysis was thus executed in the MATLAB environment, and the complete simulation procedure is displayed in the schematic of Fig. 3.5.

The use of the minimum firing event method implies finding the least number of sparse elements and their configuration that can replicate the performance of the complete array. In this case,
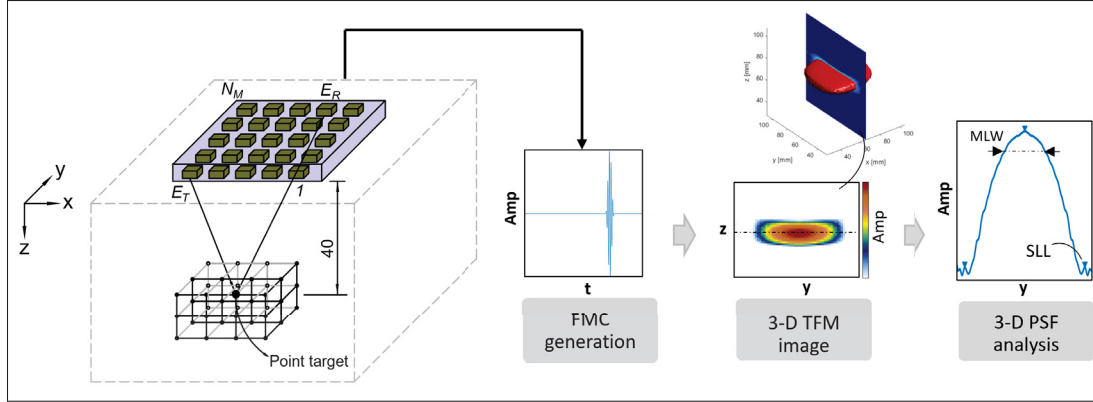
Figure 3.5   3-D PSF simulation schematic

the solution consists of approximating the MLW and SLL levels to the ones from the full array, exploring all potential combinations within a specified reduced sparse array set, such as using 5 out of 64 linear array elements in transmission. However, applying this method to wideband 2-D arrays is not feasible due to the massive iterations required and the significant time it takes to compute the pulse-echo 3-D PSF for all scenarios. To overcome this, a refinement stage prior to the search is introduced, aiming to drastically reduce the available combinations while maintaining the solution's integrity. Therefore, the suggested approach involves a two-step algorithm: the first step is a reduction of the number of combinations to be explored, while the second step executes the actual search. The suggested improvement step works as follows: initially, the number of potential combinations is computed inside MATLAB using the binomial coefficient, according to:

$$_nC_k = \binom{n}{k} = \frac{n!}{k!(n-k)!} \tag{3.8}$$

where $_nC_k$ is the binomial coefficient "n choose k" that returns a matrix containing the possible choices of n array units taken k at a time. This resulting matrix consists of k columns and $m!/k!(m-k)!$ rows, with m representing the length of vector n. After, the combinatorial set is subject to three different refinement layers. The first one consists of deactivating the array edge elements in transmission. This technique has proven to be a simple and effective way of

directly reducing the number of elements by approximately 30-35% (Diarra *et al.*, 2013; Piedade, Painchaud-April, Le Duff & Bélanger, 2023). Given that this reduction alone is insufficient, the method must be complemented. Therefore, for layer 2, symmetry in the 2-D sparse layouts was imposed. Symmetries can significantly reduce the number of potential configurations in 2-D layouts, as multiple patterns under certain symmetry operations generate equivalent PSF and thus represent repetitions in the search. For instance, a pattern that is symmetric under reflection across the vertical axis of the grid can be transformed into another pattern that is symmetric under reflection across the horizontal axis. In this case, the two patterns are considered equivalent, and only one counts as a unique pattern. To account for symmetrical layouts, group theory based on Burnside's lemma can be applied (Rotman, 1995):

$$N_{\text{pattern}} = \frac{1}{|G|} \sum_{g \in G} |X^g| \tag{3.9}$$

where G represents the symmetry operations applied in a set of combinations, X. For each symmetry operation element $g \in G$, X^g denotes the set of elements of X that remain invariant under g (i.e., $X^g = x \in X \mid g \cdot x = x$), and therefore the number of distinct patterns, N_{pattern}, can be computed. Hence, the first step is to determine the size of group G, which was set in this work to account for the horizontal and vertical reflections, main and secondary diagonals, 90, 180, and 270-degree rotations, and the identity element. The size of group G was therefore 8. Lastly, the symmetric layouts can be removed from the combinatorial set, preserving only the unique patterns. In layer 3, a minimum separation between elements was enforced, ensuring that they cannot occupy the same row, column, or diagonal. This measure is taken to prevent the PSF solution from favoring a specific direction and to prevent image distortions. Finally, a reduced set of combinations can be obtained. Fig. 3.6 displays a flowchart outlining the suggested initial refinement step, which is aimed at enabling wideband analysis through the incorporation of three refinement layers.

With the drastic reduction of available combinations, the exploration process in step 2 becomes more efficient, allowing the use of an exhaustive search for the optimal 2-D sparse layout. This

algorithm is shown in Fig. 3.7. The first row corresponds to the PSF procedure: definition of all input parameters, TOF computation, and FMC estimation. Then, a firing event was selected with the full array in reception, obtaining the volumetric PSF translated from the TFM algorithm using Eq. 3.7. From the resulting 2-D image slices in the XZ and YZ planes, main lobe width (MLW) at −6 dB and side lobe level (SLL) features were extracted. These two features are subject to three selection criteria ($C1$, $C2$, and $C3$). $C1$ requires the MLW to be the same in both directions, as it is crucial for imaging, given that the targets can be located anywhere. $C2$ and $C3$ were arbitrarily set at 1.15 times the FMC MLW and the SLL from FMC plus 9 dB, respectively. This is to uphold an acceptable lateral resolution and minimize artifacts in the image. If the solution met these criteria, the layout was stored, and the algorithm continued. If not, the solution was disregarded, and the algorithm proceeded to the next layout from the reduced set of combinations calculated in the initial step. Once the reduced set was fully explored, the algorithm concluded. The best layout was determined based on its proximity to the full array's acoustic performance regarding MLW and SLL. The pre-computation of TOFs for the PSF, along with the manageable number of combinations, allows for an efficient execution of this process. The proposed exploration algorithm is implemented in MATLAB, with N_s varying from 2 to 6 in the sparse evaluation. Ultimately, the optimal sparse layout is a compromise between image quality parameters and the number of firing events.

3.3.4   Metrics for imaging and sizing performance

The chosen metric for the quantitative assessment of TFM image quality was the contrast-to-noise ratio (CNR). This parameter was computed on the XZ slice images from setups 1 and 2. In the case of setup 1, where multiple defects were present, specific image subsets containing each defect were chosen for assessment. These subsets were standardized to 20×30 mm. This process did not apply to setup 2, where the entire image slice was evaluated. The pixels exhibiting a −6-dB drop were identified as the defect portion, while the remaining pixels were considered background noise. As a result, the CNR can be calculated as follows:
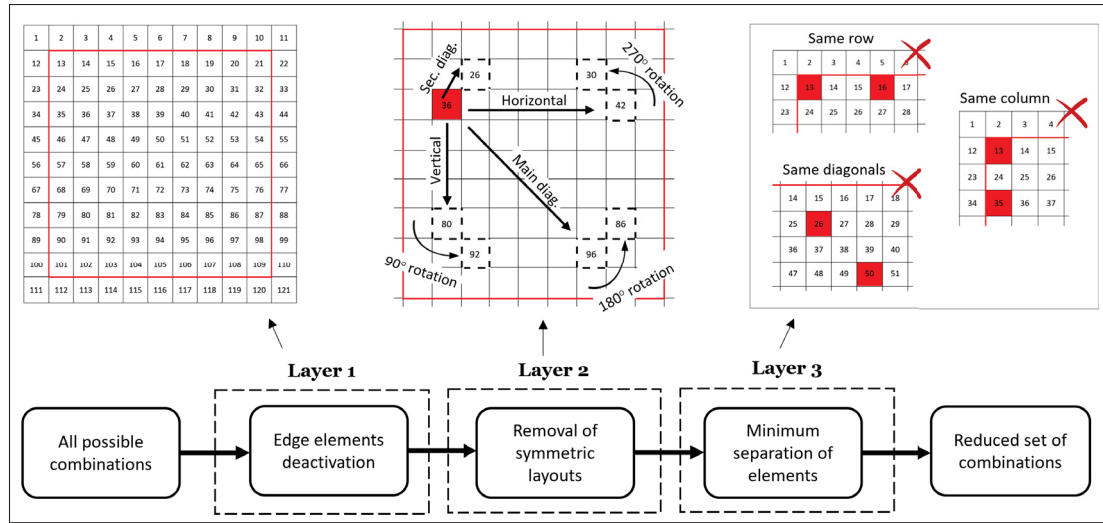
Figure 3.6   Refinement algorithm (step 1): incorporation of three distinct layers to significantly reduce the numerous potential combinations
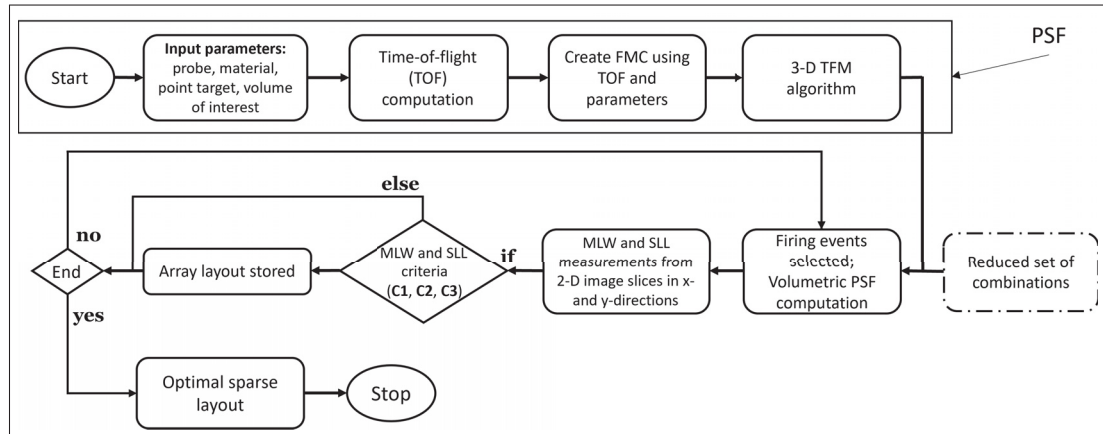
Figure 3.7   Minimum firing events algorithm flowchart (step 2) for determining optimal 2-D sparse array layouts. Prior calculation of TOFs coupled with the reasonable number of combinations enables effective execution of this process in wideband conditions

$$CNR = 20 \log_{10} \left(\frac{\left| \mu_{df(-6\,dB)} - \tilde{m}_{bg} \right|}{\sigma_{bg}} \right). \tag{3.10}$$

Here, $\mu_{df(-6\,dB)}$ represents the mean value of pixels with a -6-dB drop, which indicates the defect. $\tilde{m}_{bg}$ stands for the median of the background, calculated from the entire window excluding the -6-dB drop pixels. σ_{bg} denotes the standard deviation of the background.

Defect size accuracy was also examined, comparing each image defect from FMC with the ones generated using the sparse array method. Therefore, sizing was performed using the -6-dB drop method (Felice & Fan, 2018), measuring the transverse defect distribution at the maximum intensity pixel location. The maximum intensity in the images represents the reflections from the top of the hole for SDH and the incident face of the notch for crack-like flaws. For notch C3, trigonometry was used, while for notch B1, the longitudinal distribution up to -6 dB represented its size.

3.4   Results and discussion

In pursuit of a 2-D sparse array design under wideband conditions, a preliminary improvement step was introduced in this study. Before the search, this step strategically reduced the available combinations by incorporating symmetry and other spatial constraints. Table 1 contains the results from this procedure. It can be seen that the proposed refinement algorithm significantly reduced the number of combinations, especially for N_s greater than 3. The reduction was substantial, going from millions or billions of layouts to just a few thousand. In the case of N_s=6, the spatial constraints introduced in layer 3 explain the lower number of combinations after refinement compared to other scenarios, as fewer available positions within the array can accommodate the layouts after imposing this restriction. The required time to perform the search can thus be better controlled by setting the number of iterations in advance, therefore allowing the replacement of complex stochastic algorithms for the simplified algorithm used in step 2. The exploration time in this case was improved by approximately 98% on average.

After the trials using the minimum firing events algorithm, the best 2-D sparse layouts for each N_s were determined. The reduced candidate solutions, free of repetitions and ineffective layout options, were derived from all possible combinations. Consequently, the sparse solutions

Table 3.1   Numerical results of the proposed refinement algorithm
(step 1) for all N_s values

Sparse active firing elements (N_s)	Total number of combinations	Combinations after refinement	Reduction (%)
2	7,260	276	96.2
3	287,980	3,087	98.9
4	8,495,410	13,437	99.8
5	198,792,594	17,009	99.9
6	3,843,323,484	4,929	99.9

identified here are notably robust and closely approximate the full array, surpassing all candidate possibilities. To find the better trade-off among all N_s analyzed, the imaging parameters from the best solutions are compared. In Fig. 3.8, MLW and SLL results from those layouts are depicted, with MLW expressed in terms of wavelength. It is evident that with an increase in firing events, the MLW and SLL values become progressively closer to those of the FMC. Odd and even layouts exhibit similar performance, and the difference between them decreases with more firing events. The bar graphs demonstrate that after N_s=5, the values tend to be stabilized around the FMC. Testing for 7,8 or 9 firing events was not feasible due to substantial memory requirements for storing all possible combinations. Moreover, the results trend suggests that transitioning from 6 to 7 firing events may not yield a substantial difference, and the computation of a large number of combinations would be necessary. Considering the analyzed scenarios, N_s=6 offers the best trade-off. Therefore, this array configuration was selected as the optimal 2-D sparse layout to be used, henceforth referred to as Opt6 in this manuscript. Further exploration using alternative optimization methods could extend the investigation beyond N_s=6.

The array configurations that were implemented in this study are shown in Fig. 3.9. The FMC is the full 121×121 reference array, while Opt6 signifies the achieved optimal 2-D sparse array for 6 firing events. It can be seen that the Opt6 sparse layout exhibits a stair-stepped pattern caused by the spatial restrictions in place (preventing elements from sharing the same row, column, and diagonals). This layout represents a notable 95% reduction in the number of active elements used for transmission. Such a sparse array reflects positively on reducing data and processing times in volumetric imaging.
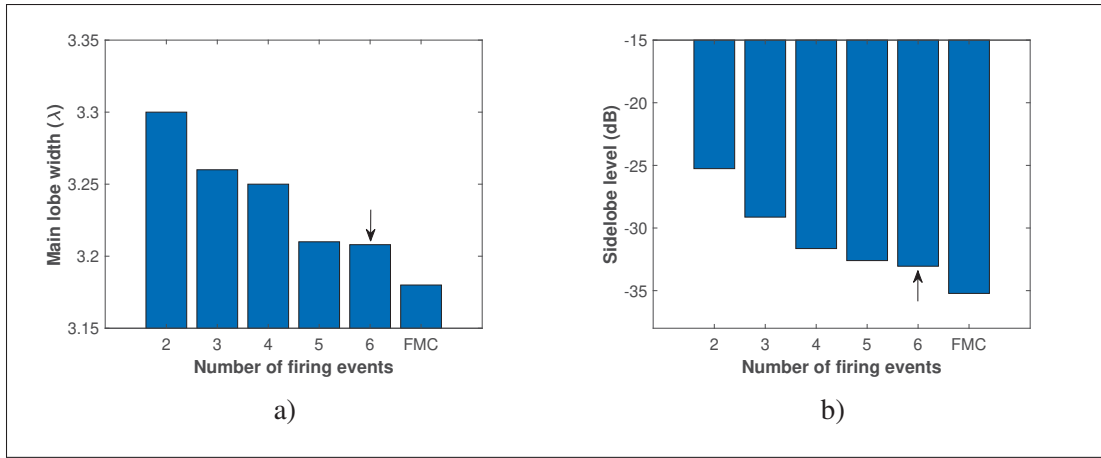
Figure 3.8   3-D PSF results regarding (a) MLW and (b) SLL from the best
sparse layouts relative to the firings events used. The arrow points to the
solution that was chosen as optimal by its proximity with FMC
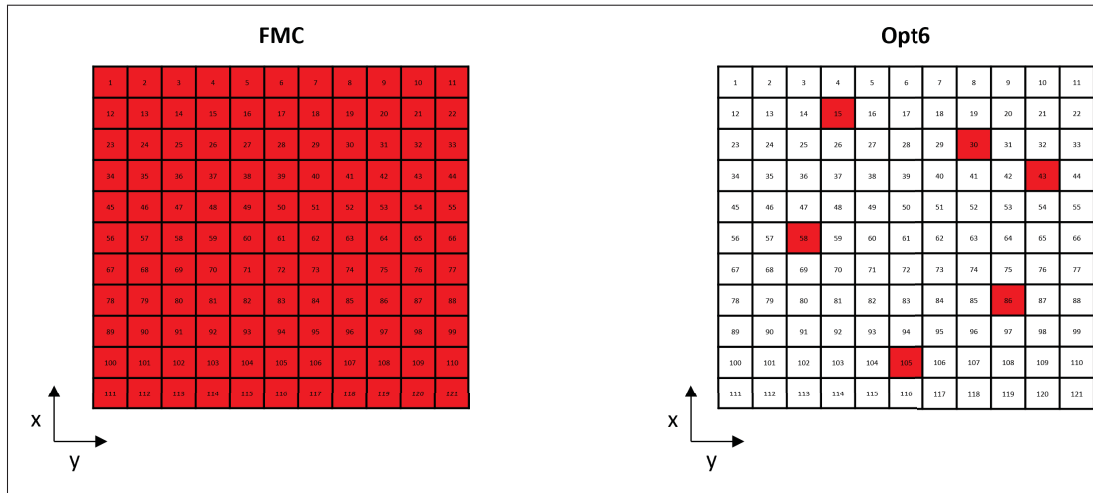
Figure 3.9   Illustration of the array layouts used, with active elements in red
and deactivated elements in white: reference array (FMC) and optimal array
for N_s=6 (Opt6)

The images generated using the 3-D TFM algorithm for FMC and Opt6 from experimental setup
1 are shown in Fig. 3.10 along with corresponding CNR results. The acquisition was carried out
from a single probe position, resulting in image indications representing reflections from the
top of the SDHs. This can be observed in the 3-D FMC image shown as an isosurface in Fig.
3.10(a), plotted at -26 dB for a better overview. SDHs 1 to 3 are visible, with the amplitude

of the defects decreasing with varying depth due to attenuation. Also, it can be seen that the spreading of the ultrasonic wave is causing the apparent length of the defect in the image to increase with increasing depth as a consequence of the relatively narrow apertures of the probe. The image slices plotted from the XZ and YZ planes correspond to the ones from the middle of the VOI. The YZ view appears more elongated compared to the XZ view, as it captures the length direction of the SDH, while XZ represents the cross-sectional aspect of the defect. Fig. 3.10(b) was generated using the same VOI and the sparse data from Opt6 to be compared with FMC. One can see that despite a significant reduction of data and firing events, Opt6 provides image quality results close to those of FMC. Due to the redundancy of data in the FMC (Karaman *et al.*, 2009), an appropriate selection of sparse elements, like the layouts employed in this study, can yield comparable TFM results with significantly fewer firing events. The CNR variation was more pronounced for low-amplitude reflectors, such as SDH 3. Employing a sparse configuration leads to fewer signals contributing to each point in the image. This effect is particularly notable for weaker indications approaching the noise level, resulting in a higher CNR variation as seen in Fig. 3.10. On the other hand, the CNR variation for SDH 1 and 2 was minimal.

Similar behavior can be noticed for setup 2 volumetric imaging results. Figs. 3.11 and 3.12 display TFM images from setup 2. The 3-D images are displayed as an isosurface at -26 dB along with corresponding 2-D slices. The chosen ray paths correspond to the transversal mode due to the wedge configuration, enabling shear wave insonification in the VOI. Hence, half skip (TT-T) and full skip (TT-TT) modes were utilized for notch B1 and C3, respectively, with this selection based on their heightened sensitivity to specular reflections using such wave paths. The proposed 2-D sparse array when used with a wedge for dual media, also demonstrated its effectiveness. In both cases, Opt6 closely resembled the reference image (FMC). The CNR presented a similar trend to setup 1, with minimal variation for the high-amplitude indications. Sparse array images exhibited some artifacts, but these did not impact the interpretation of the results or notch detection.

To assess the acceleration in ultrasonic volumetric imaging using the proposed 2-D sparse array method, the computation times of FMC and Opt6 were measured and a variation was
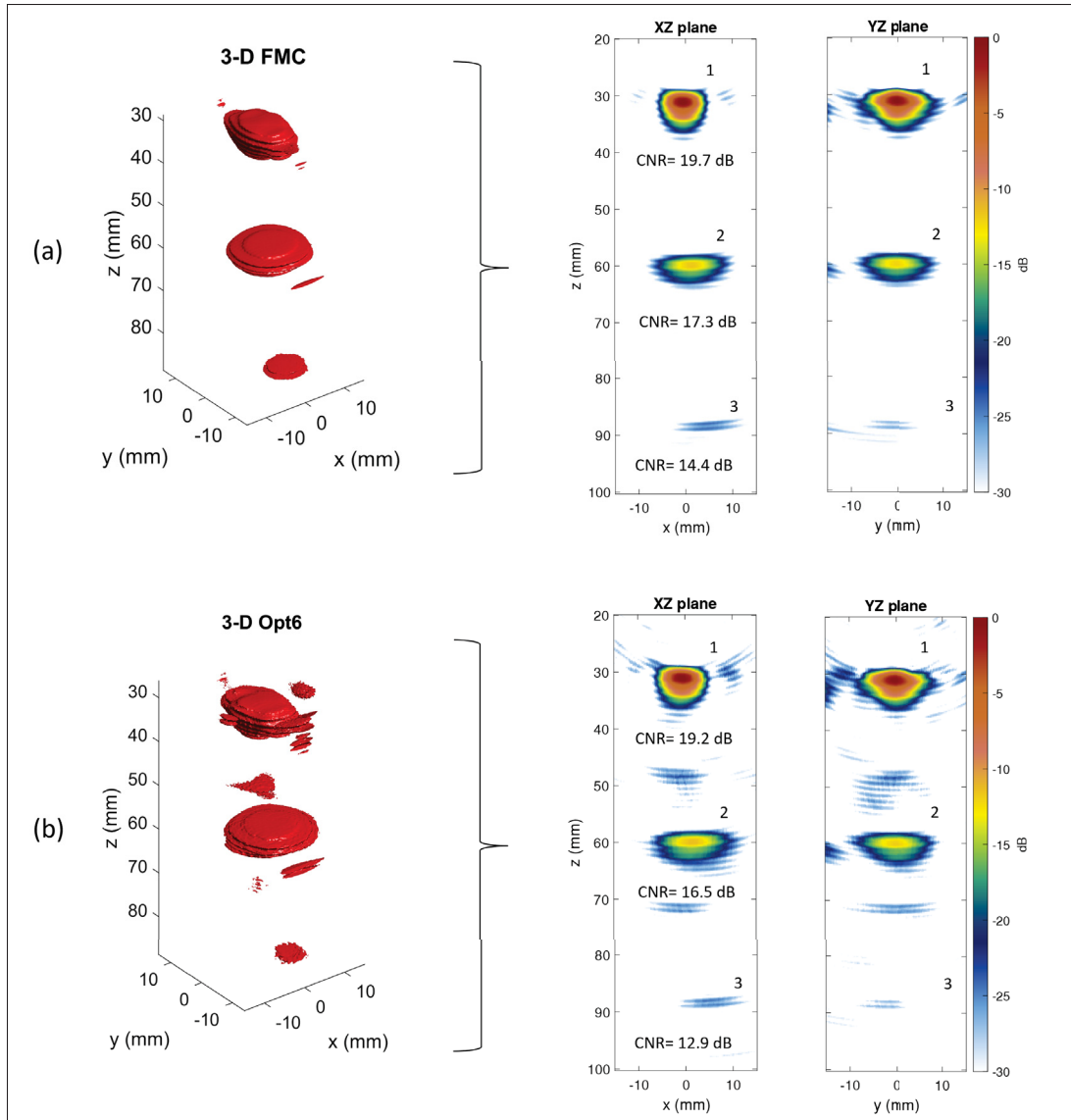
Figure 3.10   Experimental ultrasonic 3-D TFM images and corresponding 2-D image slices of setup 1: (a) FMC and (b) optimal sparse layout using 6 firing events (Opt6). CNR results for each SDH are also given

calculated to estimate the reduction in computational time. Table 3.2 contains the computation time reduction from the analyzed setups. The incorporation of sparse arrays led to a remarkable 90% reduction in volumetric imaging time. This outcome, coupled with the image quality results, indicates that the optimal sparse layout produced a volumetric TFM image comparable to that generated through FMC, but in significantly less time. For example, Opt6 accomplished
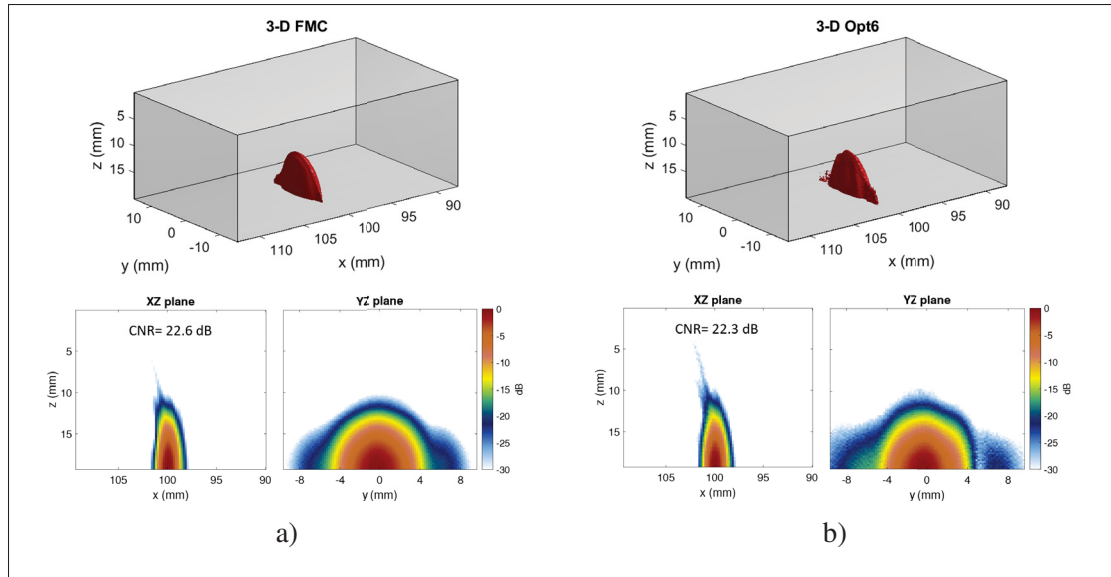
Figure 3.11   Experimental ultrasonic 3-D TFM images and corresponding 2-D image slices of notch B1 (setup 2): (a) FMC and (b) Opt6. Images were generated using TT-T wave paths
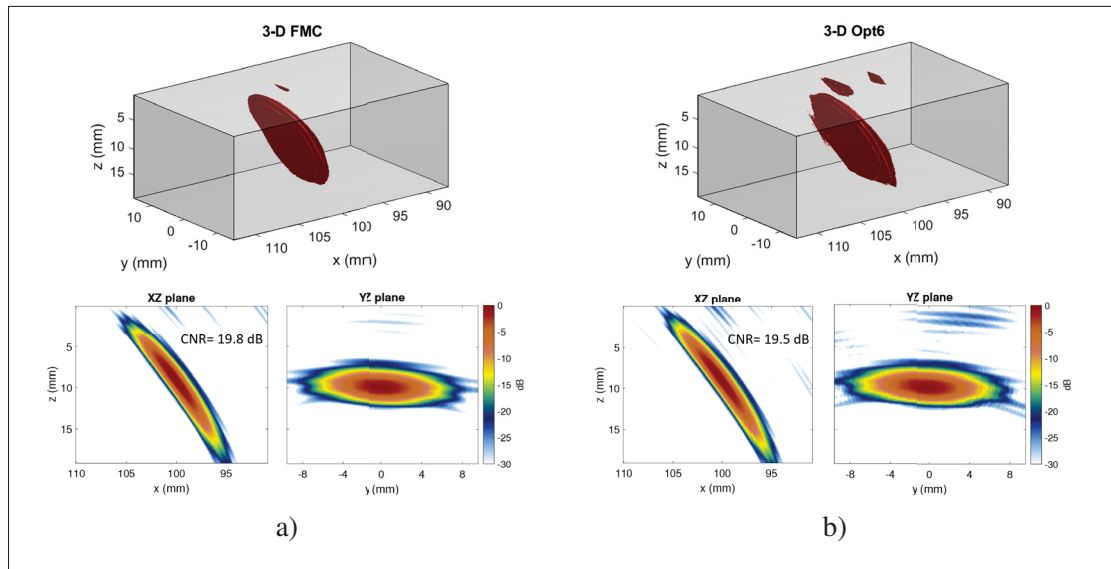
Figure 3.12   Experimental ultrasonic 3-D TFM images and corresponding 2-D image slices of notch C3 (setup 2): (a) FMC and (b) Opt6. Images were obtained through TT-TT mode

the imaging of an equivalent VOI in just 4.5 seconds, whereas an FMC would take roughly 44 seconds. This implies a volumetric imaging processing that is 9.8 times faster in practice using this technique.

Table 3.2　Computational time reduction ($\Delta\%$) for volumetric ultrasonic imaging using sparse array approach compared to FMC regarding each setup used

	Setup 1	Setup 2	
	SDH	Notch B1	Notch C3
Opt6	90	89	89

While the minimum firing events method demonstrated significant success in fast 3-D TFM imaging, it encounters limitations when applied to denser probes. Specifically, this study used a 121-element matrix probe, which allowed the computation of the complete combinatorial set of sparse layouts, to further reduction and subsequent wideband analysis. However, other commercial 2-D probes can feature element counts ranging from 256 to 1024, demanding substantial memory resources to store the matrix of candidate solutions. Nevertheless, a more efficient approach can be derived based on the observed trend in optimal layouts with varying N_s, eliminating the need for exhaustive searches. Fig. 3.13 illustrates the observed pattern of results, depicting the best layouts for varying N_s and how the elements deviate from an equidistant arrangement with edge deactivation.

The optimal layouts demonstrate a minor random adjustment of 1 to 2 columns or rows from an evenly spaced distribution (movements of none or 3 rows/columns are rare). Therefore, deactivating edge elements, evenly distributing the active elements based on N_s, and introducing random position shifts adhering to the spatial constraints of layer 3 can potentially yield a suboptimal 2-D sparse configuration. Here, "suboptimal" implies a neighboring solution to the optimal layout with a slight variation in MLW and SLL. In this way, the procedure of designing a 2-D sparse layout is facilitated, without undergoing any exploration. Fig. 3.14 shows the application of this approach using the same probe as in this study and N_s=6.
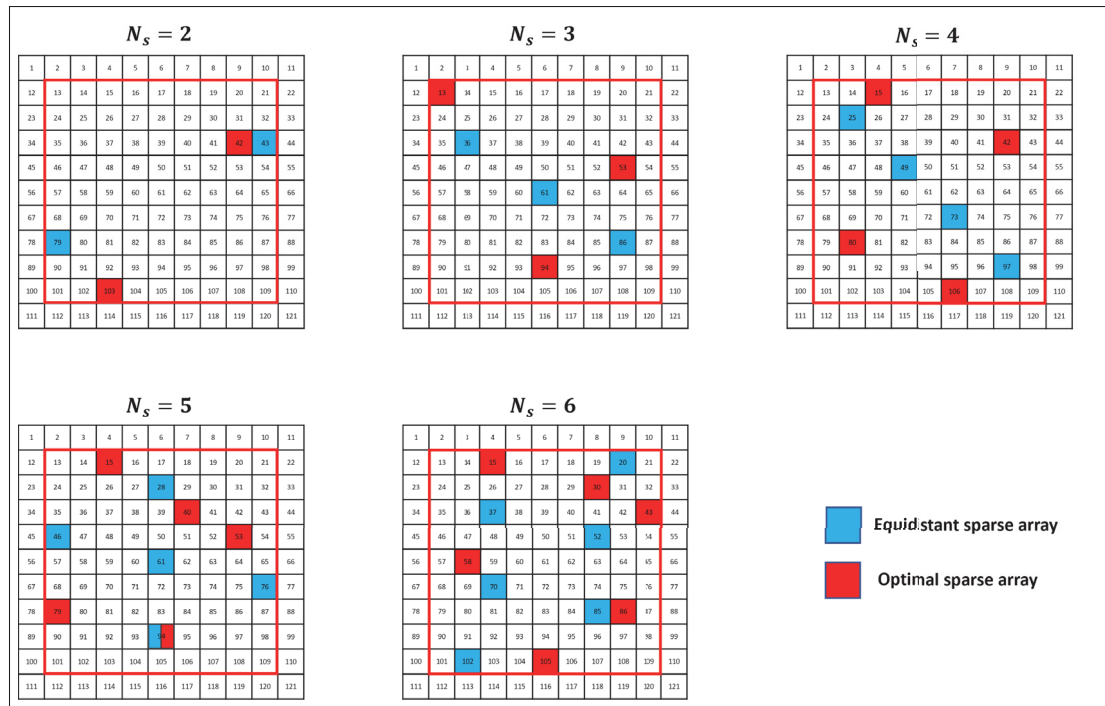
Figure 3.13   Layouts of the optimization results and their respective equidistant array considering N_s. The optimal solutions are closely related to the equidistant layouts, differing by just a random change of columns and rows
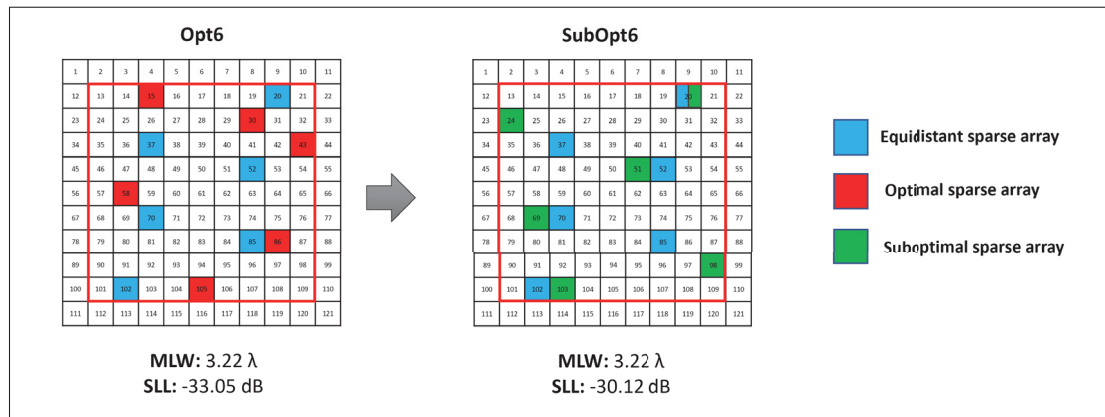
Figure 3.14   Suboptimal sparse array design illustration for 6 firing events. Random placement of elements from an equidistant layout may achieve roughly the same acoustic performance as the optimal choice

Starting from an equidistant layout, a suboptimal sparse configuration, referred to as SubOpt6, is achieved, and its PSF characteristics are assessed. While the MLW values found remain unchanged, the SLL is higher by approximately 3 dB in this particular solution. SubOpt6 was then used in the volumetric imaging of setups 1 and 2, and its CNR was evaluated for comparison. These results are comprised in Table 3.3. It can be seen that the use of the optimal layout (Opt6) results in a marginal gain compared to SubOpt6 for both setups (see Figs. 3.10-3.12 for comparison). SubOpt6 represents a neighboring solution to the optimum, with nearly identical acoustic performance. This translates to a minor CNR difference, sometimes as low as 0.1 dB. The difference in SLL between the sparse layouts likely contributes to this variation. Notably, SubOpt6 offers similar results without the need to run the algorithm, representing a viable and practical alternative for designing sparser 2-D probes.

Table 3.3   CNR results measured from the 3-D TFM images obtained using the proposed suboptimal sparse array and Opt6

Defect	SubOpt6 CNR (dB)	Opt6 CNR (dB)
SDH		
1	19.1	19.2
2	16.4	16.5
3	12.3	12.9
Notch		
B1	22.1	22.3
C3	19.3	19.8

Defect sizing relied on comparing FMC and sparse array results, with the defect image size estimated using the −6-dB drop method. Table 3.4 shows the sizing variations (Δs) of each defect analyzed, except SDH 3, for which this measurement was not possible. For the SDH case, Opt6 and SubOpt6 presented similar variations in size compared to FMC. On the other hand, smaller variations between them were observed for the notches, with SubOpt6 having a maximum variation of 8% compared to 5% for Opt6. Most importantly, both sparse array designs are within a maximum variation of 8% of the FMC, showing high accuracy in defect sizing based on the full array measurements using the proposed sparse arrangements.

Table 3.4   Results of defect size and computed
variations using FMC and the sparse layouts

Defect	FMC	Opt6		SubOpt6	
	Size	Size	Δs (%)	Size	Δs (%)
SDH					
1	5.48	5.78	5	5.76	5
2	10.86	11.07	2	11.12	2
3	-	-	-	-	-
Notch					
B1	6.00	6.30	5	6.50	8
C3	5.35	5.44	2	5.63	5

3.5   Conclusions

This study introduced an alternative to improve 3-D TFM imaging productivity by implementing the minimum firing event method for designing 2-D sparse arrays. To allow efficient processing of 3-D PSFs of arbitrary 2-D ultrasound arrays using this method, a refinement stage was proposed. This step reduced the computational load of the wideband analysis by lowering the available combinations by more than 96% without affecting the final sparse solution, eliminating redundancies and ineffective layouts. The analysis revealed that a 2-D sparse array pattern comprising 6 active transmitting elements is the minimum number of firing events required to replicate the performance of the complete array. It generated images comparable in quality to those obtained from the FMC, as evidenced by similar CNR, and most notably, this sparse layout allowed for a 9.8-fold acceleration in volumetric image processing. Moreover, the study demonstrated the feasibility of creating suboptimal 2-D sparse arrays without undergoing the exploration process, therefore offering notable practical value for sparsely designing other 2-D probes.

CHAPTER 4

COMPRESSIVE SENSING STRATEGY ON SPARSE ARRAY TO ACCELERATE ULTRASONIC TFM IMAGING

Lucas Pereira Piedade[1] , Guillaume Painchaud-April[2] , Alain Le Duff[2] , Pierre Bélanger[1]

[1] PULETS, Department of Mechanical Engineering, École de Technologie Supérieure, 1100 Notre-Dame Ouest, Montréal, Québec, Canada H3C 1K3
[2] Evident Industrial, 3415 Rue Pierre-Ardouin, Québec, Québec, Canada G1P 0B3

4.1 Abstract

Phased array ultrasonic testing (PAUT) based on full matrix capture (FMC) has recently been gaining popularity in the scientific and nondestructive testing communities. FMC is a versatile acquisition method that collects all the transmitter–receiver combinations from a given array. Furthermore, when postprocessing FMC data using the total focusing method (TFM), high-resolution images are achieved for defect characterization. Today, the combination of FMC and TFM is becoming more widely available in commercial ultrasonic phased array controllers. However, executing the FMC-TFM method is data-intensive, as the amount of data collected and processed is proportional to the square of the number of elements of the probe. This shortcoming may be overcome using a sparsely populated array in transmission followed by an efficient compression using compressive sensing (CS) approaches. The method can therefore lead to a massive reduction of data and hardware requirements and ultimately accelerate TFM imaging. In the present work, a CS methodology was applied to experimental data measured from samples containing artificial flaws. The results demonstrated that the proposed CS method allowed a reduction of up to 80% in the volume of data while achieving adequate FMC data recovery. Such results indicate the possibility of recovering experimental FMC signals using sampling rates under the Nyquist theorem limit. The TFM images obtained from the FMC, CS-FMC, and sparse CS approaches were compared in terms of contrast-tonoise ratio (CNR). It was seen that the CS-FMC combination produced images comparable to those acquitted using the FMC.

Implementation of sparse arrays improved CS reconstruction times by up to 11 folds and reduced the firing events by approximately 90%. Moreover, image formation was accelerated by 6.6 times at the cost of only minor image quality degradation relative to the FMC.

4.2 Introduction

Phased array ultrasonic testing (PAUT) is a commonly used method in nondestructive testing (NDT). The adoption of the technology has recently been on the upswing because it is a reliable, operator-safe, and flexible inspection method (Wilcox, Holmes & Drinkwater, 2007; Bai, Velichko & Drinkwater, 2015). Multi-channel acquisition techniques allow high-resolution imaging by processing signals collected with an ultrasonic phased array probe. In particular, full matrix capture (FMC) data acquisition is becoming increasingly popular among the scientific and NDT communities due to its versatility. FMC data contains rich information about the inspected medium and consists in sequentially collecting the echoes from individual elemental firings with all array elements. This data acquired during FMC can then be post-processed for flaw characterization via the total focusing method (TFM), which was reported to have notable image quality relative to current PAUT imaging methods (Fan *et al.*, 2014; Zhang *et al.*, 2013). Years after the introduction of the FMC method (Holmes *et al.*, 2005), it became widely used, and now most commercial ultrasonic array controllers support FMC-TFM capabilities. While FMC-TFM is a robust tool for a range of NDT applications, there are certain shortcomings associated with the method. For an ultrasonic array containing N_e elements, FMC needs N_e firing events, which leads to slow data acquisition due to the time interval between consecutive firings, and results in a N_e^2 size matrix of data. Moreover, this large amount of data must be transmitted and stored, hence the need for more complex systems and memory space. Other sources of acquisition speed reduction are the system architecture used and additional ultrasound paths required to perform the inspection. Today, high-end devices can handle the data processing and acquisition time burdens associated with the FMC-TFM operation. However, that is not the case for some applications, where the cost-effectiveness of such equipment remains prohibitive.

Therefore, a reduction of the generated data size is desirable for data-heavy acquisition schemes such as the FMC.

The sampling procedure in many fields traditionally follows the Nyquist-Shannon theorem, which states that the sampling rate must be twice the maximum frequency present in the signal as the minimum requirement to avoid aliasing. In practice, sampling rates 4 to 10 times higher than the Nyquist-Shannon requirement may be used to ensure that no unwanted aliasing occurs as well as to facilitate the reconstruction filter design. These high-dimensional signals are considered Compressible when expressed in a transform base such as Fourier, which means that most coefficients are irrelevant for reconstructing the original signal and can be removed. This compression paradigm is hard-coded in nearly all modern devices. A simplified version of the conventional transform domain compression can be described as follows: (1) acquisition of N signal samples, (2) computation of the transform coefficients (e.g., Fourier or wavelet), and (3) quantization and encoding, selecting only the $K \ll N$ most significant coefficients (Achim *et al.*, 2010), where K is the total number of nonzero coefficients and N the length of the vector. It can be seen that this is not an efficient procedure, as most of the analog-to-digital conversion (ADC) output is discarded. For an NDT inspection based on an FMC acquisition, in which the signals collected scale with N_e^2, this procedure becomes even more inefficient. The N_e^2 data from FMC is usually oversampled, resulting in a huge volume of data collected by the system front-end that ends up being thrown away at the compression stage. Consequently, more efficient data compression methods should be explored to improve the acquisition speed and relieve the pressure on the system front-end.

Compressed sensing (CS) is a relatively new sampling scheme that has been demonstrated to be a viable approach to reducing the data volumes (Candes *et al.*, 2006; Donoho, 2006). CS theory offers the possibility of signal recovery from fewer measurements when compared to the Nyquist sampling limit. Unlike conventional compression methods, CS proposes to acquire only the relevant signal information. Because of this, CS has attracted attention in many research fields. It is of research interest in structural health monitoring (SHM) applications such as the sparse recovery of wireless sensor signals (Bao *et al.*, 2013; Brunelli & Caione, 2015). In medical

ultrasound, CS has been extensively used to recover full datasets from a reduced number of measurements (Lorintiu, Liebgott, Alessandrini, Bernard & Friboulet, 2015; Schretter *et al.*, 2018; Ramkumar & Thittai, 2020a,b). For instance, Liu, He & Luo (2017) recovered the entire array dataset from just a few plane waves (PW) using CS in the wavelet domain, reaching a high acquisition frame rate. More recently, CS was applied to the in-phase/quadrature (IQ) domain by Zhang *et al.* (2022). In this work, the method attained a reconstruction time 3 times faster than radio frequency (RF) data and similar image quality compared with RF data. In ultrasound imaging, CS has also been used to generate 3D images with only one sensor (Kruizinga *et al.*, 2017). This suggests that a reduction of elements, combined with CS, can be exploited to reduce the hardware complexity in ultrasound devices. On the other hand, the use of CS in NDT is not as broad-based as in medical ultrasound. The CS approach has been applied to ultrasonic guided waves (Perelli *et al.*, 2013, 2015) and in a few other preliminary explorations using ultrasonic phased arrays (Bai, Chen, Jia & Zeng, 2018a; Pérez *et al.*, 2020). Due to the nature of the ultrasonic signals, CS implementation is still a challenge and sometimes leads to inadequate under-sampled recoveries. Bai *et al.* (2017) applied CS to PAUT with signal recovery based on greedy algorithms. The authors demonstrated the possibility of overcoming the Nyquist limitation in simulation. The same approach, however, could not recover experimental data at the sub-Nyquist rate. In (Xu *et al.*, 2023), the authors suggested recovering FMC data from a 5 MHz linear phased array sampled at 62.5 MHz using a CS framework. However, a sufficient recovery accuracy was achieved using only a 60% compression rate (missing data), which is far above the Nyquist-Shannon criterion. Current works in NDT (Pérez *et al.*, 2020; Bai *et al.*, 2017; Xu *et al.*, 2023) are not able to increase the compression ratio by more than 60% either because the transform basis is not appropriate for the reconstruction framework or because incoherence is not considered in the sampling scheme. In addition, there is a lack of information about defect size and position after applying CS recovery. Even when a sub-Nyquist rate recovery is achieved, the CS reconstruction procedure must be repeated for all A-scans, making the recovery of the entire FMC dataset time-consuming.

In this paper, a CS scheme applied to sparse ultrasonic arrays is proposed as a lighter and faster way to perform TFM imaging. Sparse array techniques (Austeng & Holm, 2002; Moreau *et al.*, 2009) are able to increase TFM productivity by using fewer active elements of the probe in transmission. In addition, sparse arrays can also provide a faster CS recovery. The method is therefore capable of significantly reducing the data size and hardware complexity, and ultimately accelerates TFM imaging. To that end, an efficient CS framework enabling signal recovery at the sub-Nyquist rate is suggested, and further applied to a sparse array arrangement designed to act as the complete array. Research to date in NDT has not yet explored this possibility, and therefore a CS strategy based on sparsity and incoherence concepts was proposed for an optimal CS matrix selection and, consequently, improved signal recovery, which allowed increasing the compression rate to 80%. Then, a sparse array pattern designed beforehand and independent of the compression strategy is applied. Different from other CS approaches (Ramkumar & Thittai, 2020a; Pérez *et al.*, 2020), the sparse array design is not incorporated into the sampling strategy but is rather performed separately through a simplified approach without using optimization algorithms and conditioned to the array impulse response. In this way, CS reconstruction is exclusively aimed at signal reconstruction for reduced sampling rates while imaging performance is not compromised. Therefore, the purpose of CS is to reduce the data volumes, while the sparse array concept is used to reduce the data acquisition and data processing times. Previous work (Piedade *et al.*, 2022) demonstrated the feasibility of designing an efficient sparse array that performs similarly to the full array, but using only a few firing events. In that method, less than 90% of the elements are active in transmission. In this article, this sparse array method is extended to the context of CS recovery of ultrasonic signals and to investigate adopting the CS framework for TFM imaging. Additionally, a sparse array design that, different from our previous approach (Piedade *et al.*, 2022), does not require any algorithm execution or intensive search is presented. Instead, it is suggested an equally spaced pattern with corner element deactivation as a sub-optimal configuration, also capable of operating with less than 90% of the array active in transmission. The reduction of the acquisition time and the collected A-scans achieved using such a sparse configuration can boost the CS recovery speed while keeping

the TFM accuracy relatively high. This is particularly attractive for applications that required real-time imaging.

The aim of this paper is to combine CS and sparse approaches to dramatically increase the data acquisition rate while reducing the data size. The proposed sparse CS approach was tested on experimental data and the signal recovery accuracy estimated. The TFM images generated from the CS-FMC and sparse CS datasets were quantitatively compared with the fully sampled FMC to assess the impact of data reduction on image quality. The CS reconstruction impact on defect sizing and position was also evaluated.

This article is organized as follows. Section 4.3 summarizes the fundamentals of CS. In Section 4.4, the materials and methods are presented, detailing the experimental setups, and describing the TFM imaging algorithm, and the sparse array layouts adopted. Furthermore, the proposed CS sampling scheme and the evaluation metrics are outlined. The experimental results and discussion are presented in Section 4.5 and Section 4.6, respectively. Finally, in Section 4.7, conclusions are drawn.

4.3   CS theory

According to CS theory, it is possible to recover a high-dimensional signal from measurements made at a sub-Nyquist sampling rate (Candes *et al.*, 2006; Donoho, 2006). To achieve this, CS exploits the signal sparsity on a generic transform basis. Considering an N-dimensional real-valued signal $x \in \mathbb{R}^N$ free of noise interference, which can be written as a sparse vector $s \in \mathbb{R}^N$ on a transform basis $\mathbf{\Psi} \in \mathbb{R}^{N \times N}$:

$$x = \mathbf{\Psi}s. \tag{4.1}$$

The vector s is said to be K-sparse in $\mathbf{\Psi}$ because it contains predominantly zero elements, and precisely K nonzero entries. The CS procedure consists of recovering the K-sparse vector s in

Eq. 4.1 from a reduced number of random measurements, M. The measurements are done as follows:

$$y = \mathbf{\Phi} x \tag{4.2}$$

where $\mathbf{\Phi} \in \mathbb{R}^{M \times N}$ is the measurement matrix and $y \in \mathbb{R}^M$ is the measured signal sampled using $\mathbf{\Phi}$, with the vector y containing a dramatic subsampling $M \ll N$ compared to x. Thus, combining Eq. 4.1 and 4.2 leads to:

$$y = \mathbf{\Phi}\mathbf{\Psi} s = \mathbf{\Theta} s \tag{4.3}$$

where $\mathbf{\Theta}$ is the $M \times N$ sensing matrix. For successful signal recovery from measurements $M \ll N$, $\mathbf{\Phi}$ must be incoherent with regards to $\mathbf{\Psi}$, which means the rows of $\mathbf{\Phi}$ need to be orthogonal to the columns of $\mathbf{\Psi}$. The incoherence can be measured by:

$$\mu(\mathbf{\Phi}, \mathbf{\Psi}) = \sqrt{N} \max_{1 \leq k, j \leq N} \left| \langle \varphi_k, \psi_j \rangle \right| \tag{4.4}$$

where φ_k is the kth row of the measurement matrix, $\mathbf{\Phi}$, and ψ_j is the jth column of the transform matrix, $\mathbf{\Psi}$ (Donoho & Huo, 2001). The CS reconstruction consists in solving the convex optimization problem:

$$\hat{s} = \min_s \|\mathbf{s}\|_1 \quad \text{subject to} \quad \|y - \mathbf{\Theta} s\|_2 \leq \varepsilon. \tag{4.5}$$

Eq. 4.5 is solved by finding the sparsest vector $\hat{s}$ consistent with the measurements y (Candès & Romberg, 2005), where ε is the tolerated error, $\| \cdot \|_1$ and $\| \cdot \|_2$ denote the ℓ^1 and ℓ^2 norms, respectively. Afterwards, $\hat{s}$ can be inverse-transformed using Eq. 4.1 to obtain the signal x.

4.4 Materials and methods

4.4.1 Experimental setup

Experiments were carried out using two different setups: (1) the probe placed in direct contact and (2) the probe mounted on a wedge, which corresponds to a double-layer medium inspection. The first configuration features side-drilled holes (SDH) situated at different depths in an aluminum block, while the second one presents a low-carbon steel plate containing angled electrical discharged machined (EDM) notches. The conclusions of this work can however be extended to other materials and applied to different flaws. In both setups, the probe was connected to a Vantage-64 LE acquisition system. FMC acquisition was performed for each scenario at a sampling rate (SR) of 62.5 MHz and the data was post-processed in MATLAB using the delay-and-sum (DAS) method to obtain the TFM images. A square pixel resolution of 0.10 mm was used to generate the images.

4.4.1.1 SDH Inspection

For the first setup, a 5L64-I1 Olympus linear ultrasonic phased array probe was positioned in contact with an aluminum block containing side-drilled holes (SDH) at different depths. This probe features 64 piezoelectric elements operating at a center frequency of 5 MHz and with an elementary pitch of 0.6 mm. The SDH were made within the block at five different depths and shifted 1 mm laterally with respect to the previous SDH. The block dimensions were 160 mm $\times$ 62 mm $\times$ 50 mm. Two full matrix capture (FMC) datasets were collected, corresponding to different block orientations: vertical and horizontal, herein named VBP (vertical block position) and HBP (horizontal block position), respectively. This was done to evaluate the proposed approach's performance on defects placed in the axial and lateral directions relative to the probe. Fig. 4.1 (a) shows the block inspection and its dimensions, along with the region of interest (ROI) for each orientation.

4.4.1.2 Angled Notch Inspection

For the second setup, a low-carbon steel plate, 19.05 mm thick, containing four surface-breaking electrical discharged machined (EDM) notches of 0.3 mm width was used. The notches were machined in the bottom of the plate at angles ranging from 60−90° (see Fig. 4.1(b)). These artificial flaws resemble the defects that might arise in welds. Measurements were performed using the 7.5L60-PWZ1 Olympus linear ultrasonic phased array probe (7.5 MHz center frequency, 1.0 mm pitch, and 60 elements) mounted on a wedge (Olympus SPWZ1-N55S). Only the results for notches B1 (90°) and B3 (70°) are presented in this paper. The probe was placed on the right-hand side of the notch, much the same as an actual weld bevel scanning position. The FMC acquisition was performed for each notch. Table 4.1 displays all the experimental parameters used in each configuration.
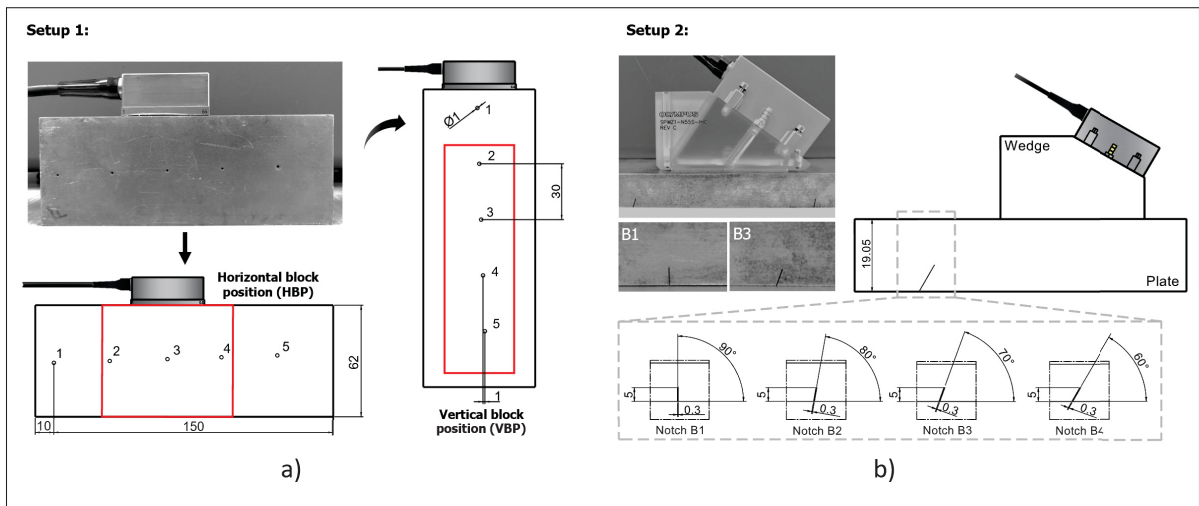
Figure 4.1 Experimental setups used. First setup: (a) 5L64-I1 ultrasonic probe in contact, block orientations and regions of interest. Second setup: (b) 7.5L60-PWZ1 ultrasonic probe mounted on a wedge and detailed views of the surface-breaking EDM notches in the low-carbon steel plate. Only results for notches B1 and B3 are presented in this paper

Table 4.1   Experimental parameters

Parameters	Setup 1 (SDH Inspection)	Setup 2 (Angled Notch Inspection)
Transducer		
Center frequency	5 MHz	7.5 MHz
Element count	64	60
Bandwidth (-6dB)	83%	75%
Pitch	0.6 mm	1.0 mm
Wedge		
Model	-	SPWZ1-N55S
Angle	-	55º
Material	-	Rexolite
Sample		
Material	Aluminum	Low-carbon steel
Longitudinal sound velocity	6354 m/s	5953 m/s
Shear sound velocity	3113 m/s	3243 m/s

4.4.2   Total focusing method and sparse array

Delay functions applied to signals from ultrasonic phased array allow to focus on a specific location, which improves local sensitivity and consequently increases the probability of detection. When a defined region is segmented into a grid of pixels, it is possible to synthetically focus on every point, creating a fully focused image. This is the founding principle of the TFM technique, which involves reconstructing an image based on FMC. According to the TFM imaging algorithm principle, focusing is performed on every point of the ROI and the signals S_{ij} from all N_e array elements are summed. Then, the image intensity $I(x, z)$ at any pixel point can then be obtained by:

$$I(x, z) = \left| H\left(\sum_{i=1}^{N_e} \sum_{j=1}^{N_e} S_{ij}\left(t_{ij}(x, z)\right) \right) \right| \tag{4.6}$$

where H represents the Hilbert transform, and t_{ij} corresponds to the propagation time of the ultrasonic wave from the transmitting element (T) to the target pixel P, and back to the receiving element (R). Consider the xOz coordinate system in Fig. 4.2(a), where a generic probe is centered at the origin O and placed in contact with a block as in the first experimental setup. The array elements are positioned in the X-axis orientation, and the Z-axis is perpendicular to them.

The propagation distance $d_{Ti,Rj}$ considered is the one that travels with the least time according to Fermat's principle and is determined through simple geometric relationships. Therefore, the propagation time t_{ij}, also known as the time-of-flight (TOF), can be computed by dividing this distance by the longitudinal sound velocity of the measured medium, c_2:

$$I(x,z) = \left| H \left(\sum_{i=1}^{N_e} \sum_{j=1}^{N_e} S_{ij} \left(\frac{\sqrt{(x-x_i)^2 + z^2} + \sqrt{(x-x_j)^2 + z^2}}{c_2} \right) \right) \right| \tag{4.7}$$

where x_i and x_j are the position of the ith transmitter (T) and the jth receiver (R) in the x-orientation, respectively.

Expectedly, the TFM imaging procedure can be extended to inspections using a wedge, such as the second setup case. The model is considered equivalent to a double-layer medium measurement. The xOz coordinate system is kept positioned at the interface, but the array elements are inclined at an angle θ with respect to the x-direction and elevated at different heights h_n (with $n = 1, 2, 3, \ldots, N_e$) by the wedge, as seen in Fig. 4.2(b). For an incident point e_i on the interface corresponding to the ray of the ith transmitter element, the incident angle is θ_i, and the refracted angle is θ_e. The incident point position $e_i(x_{it}, 0)$ of the ith transmitter and the jth receiver $e_j(x_{jr}, 0)$ can be found by combining Fermat's principle and Snell's law. Thus, the TOF for the TFM image intensity using Eq. 4.6 is now computed as follows:

$$t_{ij}(x,z) = \frac{\sqrt{(x_i - x_{it})^2 + (-h_i)^2} + \sqrt{(x_j - x_{jr})^2 + (-h_j)^2}}{c_1} + \frac{\sqrt{(x-x_{it})^2 + (z)^2} + \sqrt{(x-x_{jr})^2 + (z)^2}}{c_2} \tag{4.8}$$

where c_1 is the longitudinal sound velocity in the wedge, and x_{it} and x_{jr} are the position in the x-direction of the transmitter and the receiver incident point at the interface, respectively.
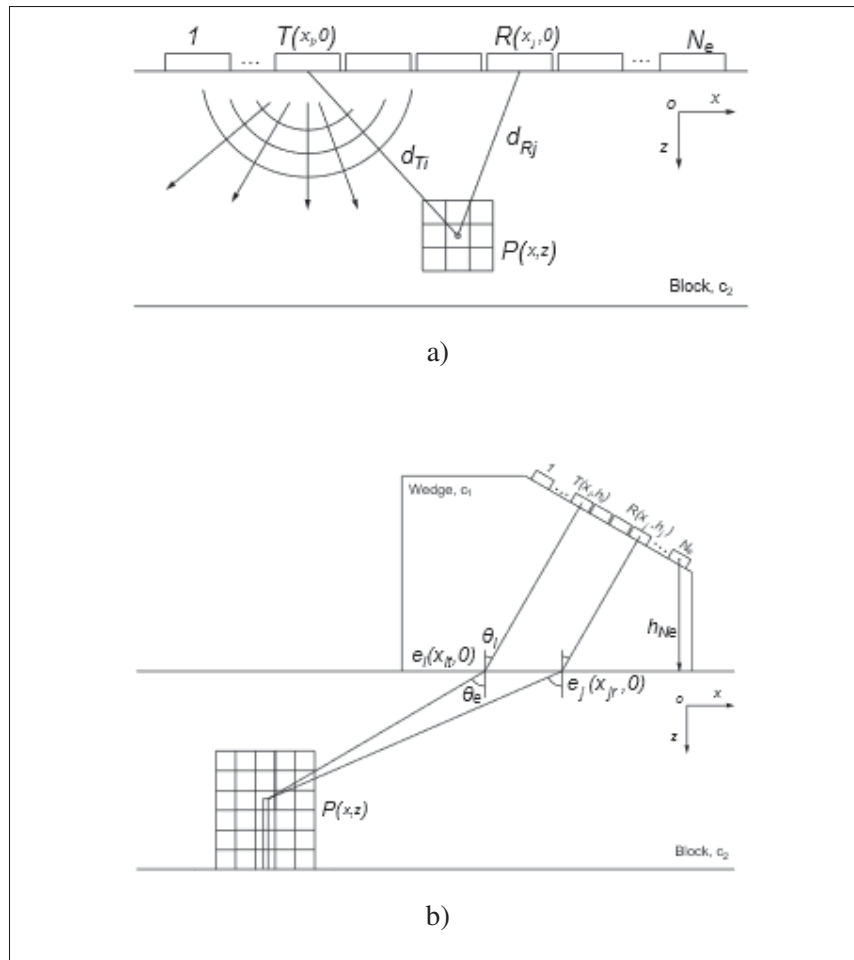
Figure 4.2   TFM imaging schematic: (a) contact and (b) wedge

It can be seen that adopting the FMC-TFM method increases the acquisition and computation time, as the amount of data acquired in the FMC and processed by the TFM is directly related to the number of probe elements. On the other hand, the sparse array technique is a practical alternative for this case (Austeng & Holm, 2002; Moreau *et al.*, 2009). From a given number of active elements N_{actv} selected for the sparse layout, other elements are deactivated in transmission, while the entire array is used in reception. The result is a subset of the full array that contains a reduced amount of data as the FMC (i.e., $N_{actv} \times N_e$ dataset is used instead of the $N_e \times N_e$ matrix), and that is collected and post-processed more rapidly. In (Piedade *et al.*, 2022), the authors demonstrated the viability of using a sparse array layout using only 5 elements in

transmission. By exploring all array combinations, an optimal sparse layout was obtained using this method. In addition, a sparse equally spaced layout with corner element deactivation was able to achieve roughly the results from the optimal sparse configuration without requiring the exploration process. This was an important observation as the time needed to explore the entire set of combinations may represent an obstacle for other ultrasonic probe sparse designs. The minimum firing events method was therefore chosen as the sparse array approach used in this work. For the first setup, the optimal sparse design from Piedade *et al.* (2022) with $N_{actv} = 5$ was used, as the measurements of this setup were done with the same ultrasonic probe (5L64-I1 ultrasonic array). The optimal sparse layout corresponds to elements [12 20 34 42 56] active in transmission. Meanwhile, the sparse design adopted for the second setup was equally spaced, with the edge elements deactivated, and so the exploration process was not required. $N_{actv} = 5$ was also used for this scenario. In this design, the elements from both array edges are discarded in transmission (e.g., elements 1 to 5, and 55 to 60, when considering probe 7.5L60-PWZ1) and the remaining elements are placed in a periodic distribution according to N_{actv}. The sparse layout used in this case was [10 20 30 40 50].

4.4.3   CS framework

For a successful signal recovery, the CS premises of sparsity and incoherence must be fulfilled. In other words, high sparsity and incoherence are needed for a high probability of ℓ^1 norm minimization in Eq. 4.5 to converge to the sparsest vector, $\hat{s}$. Therefore, selecting the optimal matrices $\mathbf{\Phi}$ and $\mathbf{\Psi}$ is of critical importance. In this study, a CS strategy based on the selection of optimal transform and measurement matrices to reconstruct the FMC is proposed. The optimal transform basis was chosen between the discrete cosine transform (DCT) and the discrete wavelet transform (DWT). For that, the sparseness of the A-scans (x) with respect to each transform was estimated (Hoyer, 2004):

$$Sparseness = \frac{\sqrt{N} - \frac{\|X\|_1}{\|X\|_2}}{\sqrt{N} - 1} \tag{4.9}$$

Here, N is the length of the transformed signal X, $\| \cdot \|_1$ and $\| \cdot \|_1$ are the ℓ^1 and ℓ^2 norms, respectively. The vector is sparse when the computed value is 1, whereas a dense vector (all elements are non-zero) is equal to 0. Four wavelet families were used for DWT: Daubechies (db2–6), Coiflets (coif1–5), Symlets (sym2–10), and Biorthogonal (bior2.2–2.8, 4.4, 5.5, 6.8). Each wavelet was considered at different decomposition levels, ranging from 2 to 6. It is important to highlight that the sparsity of the signal and the sparse layout of the probe elements are two distinct subjects in this work and are therefore not related. After selecting the best matrix Ψ, the incoherence with Φ must be measured using Eq. 4.4. The μ value ranges between 1 and $\sqrt{N}$ depending on the matrix used. Measurement matrices with random Gaussian and Bernoulli distributions, as well as the partial Hadamard matrix, were chosen to be tested. These sampling matrices are known to be incoherent with most transform bases (Candes & Tao, 2006; Liu & Luo, 2018). The partial Hadamard matrix is designed randomly, selecting M lines from the $N \times N$ Hadamard matrix.

Once the optimal Ψ and Φ matrices were selected, the CS reconstruction procedure could begin. A routine was created in MATLAB to reconstruct the FMC dataset. The FMC acquired from setups 1 and 2 were given as input to the CS framework. The routine was composed of the optimal matrices and the solver (Candès & Romberg, 2005). According to the desired compression rate (CR), the vector y containing fewer measurements M is obtained using 4.2. The CR is calculated by:

$$CR = \left(1 - \frac{M}{N}\right) \times 100 \tag{4.10}$$

where M is the length of the vector y, and N is the length of the original signal x. The CS-FMC and sparse CS methods use the fully sampled datasets from setups 1 and 2 as input. Then, each A-scan passes through downsampling using Eq. 4.3 and is recovered after solving Eq. 4.5. The reconstructed signals are sequentially placed in a new matrix. This procedure is repeated for all the A-scans in the case of CS-FMC $N_e \times N_e$. On the other hand, for the sparse CS method, only the A-scans from the corresponding number of active elements ($N_{actv} \times N_e$) are recovered,

which results in faster CS recovery. The CS-FMC and the sparse CS data matrices are later used to generate the TFM images.

4.4.4   Performance metrics

The percent residual difference (PRD) between the reference and the recovered signals is the metric used to determine the CS recovery efficiency (Perelli *et al.*, 2015; Bai *et al.*, 2017), according to:

$$\text{PRD} = \sqrt{\frac{\sum_{n=1}^{N}(x_n - \hat{x}_n)^2}{\sum_{n=1}^{N}(x_n)^2}} \times 100 \tag{4.11}$$

where x is the original signal, $\hat{x}$ is the recovered signal using CS, and N is the length of both signals. Thus, higher PRD values indicate poor reconstruction quality.

The image contrast was the metric used to assess the TFM image quality through the contrast-to-noise-ratio (CNR). Due to the presence of multiple defects in the images from setup 1, individual subsets of the ROI containing each defect were selected for evaluation. Equal subsets of 30 mm × 40 mm were used for VBP and 35 mm × 23 mm for HBP. This procedure did not apply to setup 2, and thus the entire ROI was considered in this case. The −6 dB drop pixels corresponded to the defect portion in the image, while the remaining pixels were defined as the noise in the background. The CNR is therefore given by:

$$\text{CNR} = 20 \log_{10} \left(\frac{|\mu_{\text{df}(-6\text{dB})} - \widetilde{m}_{\text{bg}}|}{\sigma_{\text{bg}}} \right) \tag{4.12}$$

where $\mu_{\text{df}(-6\text{dB})}$ is the mean of −6 dB drop pixels, which corresponds to the defect, $\widetilde{m}_{\text{bg}}$ is the median of the background (entire window excluding −6 dB drop pixels), and σ_{bg} is the standard deviation of the background.

The defect size and position accuracy were also investigated. Each image defect was individually compared to the actual defects in the samples. To estimate the position of the defects, the

maximum intensity pixel was considered. For the SDH, the maximum intensity corresponds to the reflections from the top of the hole, whereas for the crack-like flaws, it corresponds to the incident face of the notch. The −6 dB drop technique was the sizing method used (Felice & Fan, 2018). This procedure is done by measuring the transverse distribution of the defects in the images at the maximum intensity pixel location. For notch B3, simple trigonometry is required for sizing in the transverse distribution, whereas for notch B1, the longitudinal distribution ranging from the maximum and up to −6 dB corresponds to its size (notch face length).

4.5   Results

4.5.1   CS signal recovery

The compression performance of two different sparse bases was compared in the initial series of analyses. Signal sparsity in a generic transform basis is an a priori condition for a successful CS signal recovery. The sparser the representation of the original signal, the greater the recovery accuracy of its under-sampled version. The sampling frequency according to the Nyquist-Shannon theorem should be higher than twice the maximum frequency component present in the signal [i.e., $2 \times$ (center frequency + bandwidth/2)]. Notably, the frequency contents of the signal will rely on the bandwidth of both the instrumentation and the probe used. Following this theorem, the minimum sampling for setup 1 is 14.15 MHz, and 20.62 MHz for setup 2 (see Table 4.1). However, the collected experimental signals were oversampled according to the Vantage-64 LE configuration (62.5 MHz of sampling frequency).

Fig. 4.3(a) shows an experimental A-scan from setup 1 sampled at 62.5 MHz, which corresponds to 4.4 times the minimum required by Nyquist, considering the probe's central frequency and bandwidth (14.15 MHz). Information on the front and back walls and the SDHs is also shown. The CS procedure consists of removing some parts of the original signal using Eq. 4.2, and thus a compression rate of 80% was applied to keep the number of samples under the Nyquist limit. Fig. 4.3(b) and Fig. 4.3(c) show the reconstructed A-scan and the corresponding PRD values using the DCT and the four-level sym8 DWT, respectively. A typical random Gaussian matrix

was adopted for the subsampling. The signal reconstruction is clearly more efficient when using the DWT, as it can provide a sparser representation of the ultrasonic signals compared to the DCT. In this case, the sparseness was measured as 0.55 for DCT and 0.69 for DWT. A similar CR was applied to the signals of setup 2, and the same reconstruction accuracy trends were observed.
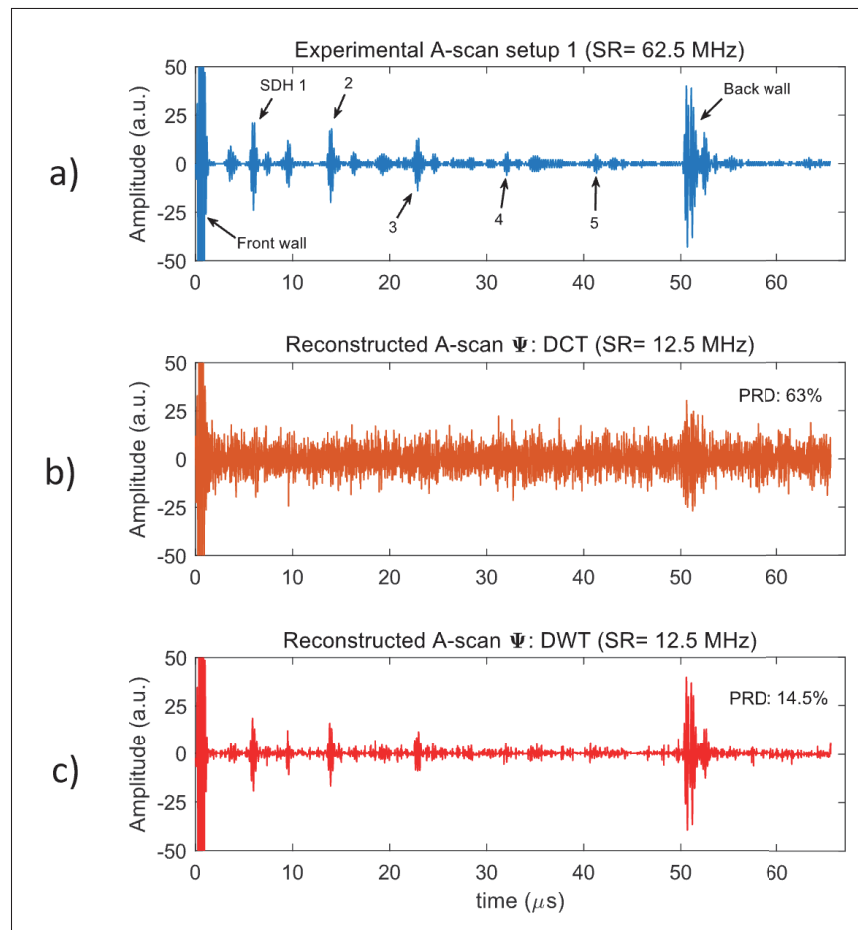
Figure 4.3   (a) Original experimental A-scan from setup 1 and the recovery results of the (b) DCT and (c) DWT. The number of samples used corresponds to a sampling rate (SR) of 12.5 MHz according to the CR applied

To further demonstrate the reconstruction efficiency of the DWT over the DCT, the complete dataset from the 35th transmitting element is presented in Fig. 4.4. The images are composed of A-scans stacked side by side in the vertical position, the responses from defects, front wall, and

back wall are all marked. Fig. 4.4(a) is the reference image and it contains the fully sampled data, while Fig. 4.4(b) and Fig. 4.4(c) show the results for the reconstructed data using DCT and DWT, respectively. Similar to the A-scan results presented in Fig. 34.3, it is observed that the level of reconstruction error is higher for DCT than DWT. It is not possible to infer the responses from SDH 3 to 5 and the remaining indications are compromised by the poor reconstruction quality. On the other hand, the DWT in Fig. 4.4(c) presents a closer representation of the fully sampled data, with only SDH 4 and 5 showing an amplitude reduction compared to Fig. 4.4(a).
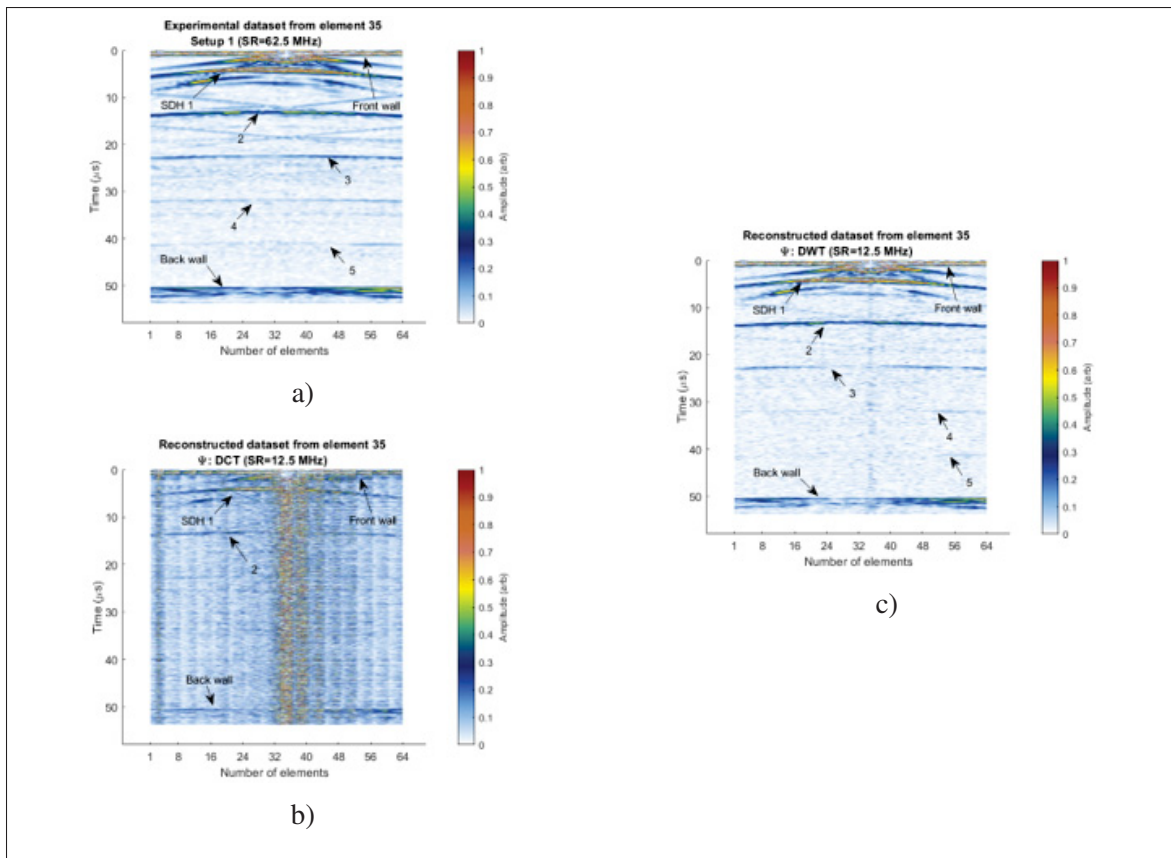
Figure 4.4 Image plots from the complete dataset of the 35th element: (a) fully sampled dataset from setup 1 and the recovered results using the (b) DCT and (c) DWT. High levels of reconstruction errors are observed using the DCT

In total, 30 wavelets were analyzed at several decomposition levels. For the sake of brevity, Fig. 4.5(a) plots only three of the sparseness measurement results. The figure shows that the six-level decomposition of coif5 has the highest sparsity value (0.71). The remaining wavelet

families used in this study presented sparsity values over 0.59 after the first decomposition. To further illustrate the effect of sparsity on signal reconstruction efficiency, the optimal and an inferior wavelet were compared. Fig. 4.5(b) displays the reconstruction result using the wavelet providing the higher sparseness value, while Fig. 4.5(c) shows the reconstruction using the wavelet with the lower sparseness value, represented by the sym2 second decomposition level. The original and the reconstructed signals are superimposed in both figures to highlight the differences between them. More reconstruction errors can be observed in Fig. 4.5(c) than in Fig. 4.5(b) due to the difference in signal sparsity provided by the transform basis.

Another important concept of CS theory is incoherence, and therefore to achieve optimal signal reconstruction, selecting the optimal measurement matrix, $\mathbf{\Phi}$, is also required to be used in Eq. 4.2. Three measurement matrices were examined with respect to the previously chosen optimal sparse basis, $\mathbf{\Psi}$. The incoherence, μ, measured using the Gaussian matrix was 5.1, while the Bernoulli and partial Hadamard matrices were 6.1 and 11.5, respectively. The maximum incoherence is measured when μ is equal to 1, and thus the Gaussian matrix is the most adequate for the CS strategy. Therefore, it was found that the optimal reconstruction was the DWT, using a random Gaussian measurement matrix and the ℓ^1 norm minimization for signal recovery. In view of these results, the proposed CS strategy was implemented in a MATLAB routine and was applied to the FMC ultrasonic A-scan signals.

4.5.2 SDH inspection results

Fig. 4.6 presents the TFM ultrasonic images of VBP. The images were generated using the TFM algorithm for the fully FMC, CS-FMC, and sparse CS data matrix. The SDHs from 2 to 5 and the back wall are displayed in the images. All the TFM images were preferably displayed using the linear scale from 0 to 1 instead of the decibel (dB) scale, so that features that impact image quality such as background noise and artifacts are visible for all cases without requiring dynamic range adjustments. In Figs. 4.6(a–c), a decrease in the image indicators' amplitude is observed as a result of the attenuation. Compared to the reference FMC image, a loss in amplitude is seen for the deeper defects of CS-FMC [SDH 4 and 5 in Fig. 4.6(a) and Fig. 4.6(b)]. However, Fig.
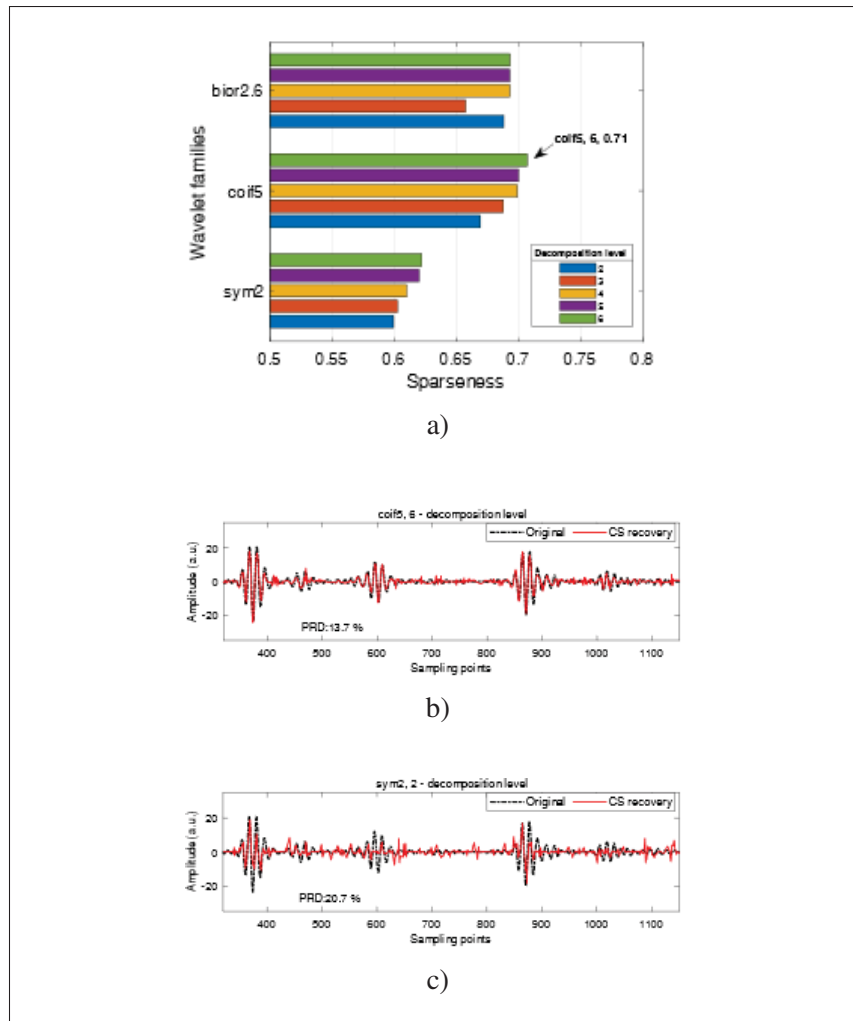
Figure 4.5   (a) Sparseness results of the ultrasonic
signals using three wavelet families varying the
decomposition level. The CS recovery using (b) the
optimal wavelet, and (c) the sym2 second level of
decomposition. Some reconstruction errors are evident
when using the inferior wavelet compared to the optimal

4.6(b) shows a reduction in the level of artifacts surrounding the SDH. Fig. 4.6(c) on the other hand exhibits more background noise. Still, it is possible to locate and size the defects in the image.

Fig. 4.7 displays the ultrasonic images obtained for HPB. The defects, probe position and back wall are shown. Most of the ultrasonic energy is received by defects placed under the aperture of
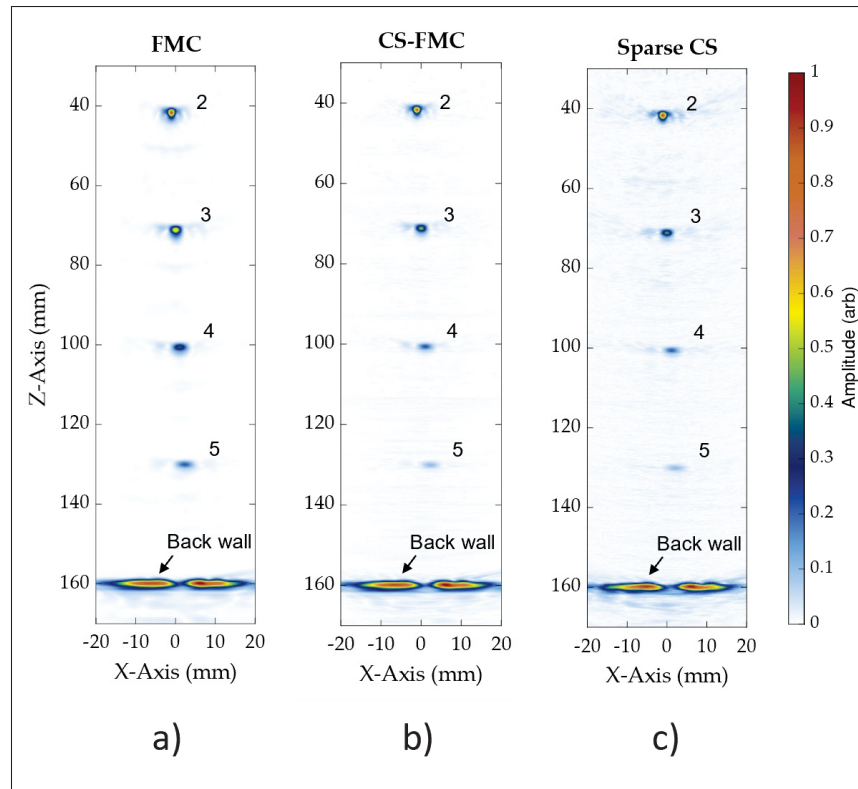
Figure 4.6   Experimental ultrasonic TFM images of
VBP generated from (a) FMC, (b) CS-FMC and (c) sparse
CS datasets. The same ROI and pixel resolution were
used for each plot

the probe, and therefore, SDH 3 exhibits the highest amplitude as compared to SDH 2 and 4, for all cases. The images followed a behavior similar to VBP, with the CS-FMC in Fig. 4.7(b) presenting reduced artifacts around the SDH and background noise as compared to the reference Fig. 4.7(a), while the sparse CS [Fig. 4.7(c)] shows comparable results in terms of the full array, despite a small loss in image quality.

The CNR plots relative to the SDH number for the inspected block positions are shown in Fig. 4.8. In Fig. 4.8(a), the CNR curves fall downwards due to attenuation in VBP, with SDH 2 presenting the highest CNR value and decreasing until SDH 5. On the other hand, Fig. 4.8(b) displays three-cornered curve trends. SDH 3 is placed under the aperture of the probe and thus presents the highest CNR, while SDH 2 and 4 are on the left and right ends of the curves,
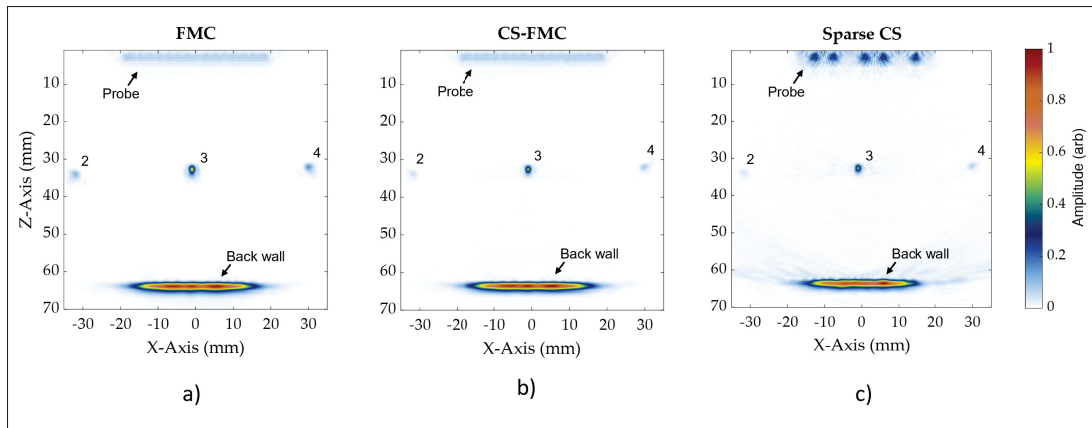
Figure 4.7   Experimental ultrasonic TFM images of HPB using the same ROI and pixel resolution from (a) FMC, (b) CS-FMC and (c) sparse CS datasets. The probe position, back wall, and defects can be seen in the images. Artifact reduction is noticed in CS-FMC, whereas a sparse CS can produce comparable results as the full array, with fewer firing events and data

respectively. There is a slight difference between SDH 2 and SDH 4 CNR values in Fig. 4.8(b), accounting for the distinct amounts of transmitted ultrasonic energy to their positions. It can be seen that CS-FMC provides an image quality similar to the FMC for both block positions. The CS-FMC image quality is indeed better considering the high amplitude image reflectors (see Figs. 4.6 and 4.7), while the lower amplitude defects present a performance close to that of the FMC. Despite the substantial reduction of data and firing events, only a small reduction in image quality was observed for the sparse CS images, with a more pronounced difference seen in the lower amplitude defects (SDH 4 and 5 in VBP; SDH 2 and 4 in HBP).

Tables 4.2 and 4.2 provide the flaw sizing and position accuracy results with respect to the actual block for VBP and HBP, respectively. A percent difference was computed for each SDH relative to their actual position and size. The notations δ_x and δ_z indicate the percentage difference in the x- and z-axes, respectively, and δ_s is size accuracy. The flaw size was measured only in the x-dimension, as the z-dimension is a function of pulse width instead of the flaw size (Felice & Fan, 2018). From both tables, it can be seen that the CS reconstruction did not cause significant variations in the defect position. A variation of 6% was the highest value measured, and for some of the SDHs, no or small variations were observed. The ultrasonic beam spread
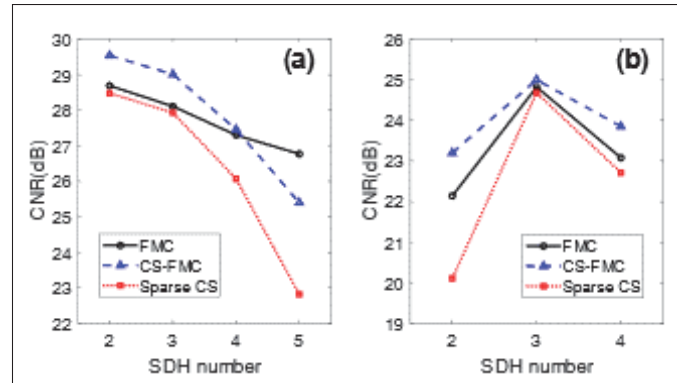
Figure 4.8   CNR plots of (a) VBP and (b)
HBP measured from the images shown in
Fig. 4.5 and 4.6

has a significant effect on image sharpness, and therefore, δ_s scales with increasing defect depth (see Table 4.2). This effect is reduced in HBP, as the maximum flaw depth is around 35 mm, and hence a smaller variation occurred. Higher variations were observed for defects outside the probe's aperture in this case.

Table 4.2   Variation of defect position and size
of VBP regarding the actual test sample

SDH number	CS-FMC/Actual			Sparse CS/Actual		
	$\delta x(\%)$	$\delta z(\%)$	$\delta s(\%)$	$\delta x(\%)$	$\delta z(\%)$	$\delta s(\%)$
2	0	6	61	1	5	70
3	0	2	113	1	2	118
4	0	2	194	0	1	213
5	1	1	251	1	1	307

Table 4.3   Variation of defect position and size
of HBP regarding the actual test sample

SDH number	CS-FMC/Actual			Sparse CS/Actual		
	$\delta x(\%)$	$\delta z(\%)$	$\delta s(\%)$	$\delta x(\%)$	$\delta z(\%)$	$\delta s(\%)$
2	5	5	76	5	5	86
3	1	4	18	1	4	27
4	2	5	78	2	6	77

4.5.3   Angled notch inspection results

Several ultrasonic ray paths, such as direct, half-skip, and full skip, were considered in imaging setup 2. Only the TT-T and TT-TT modes were selected as they were more sensitive to specular reflections considering the adopted flaw angles, and consequently, provided more information about the notches. Fig. 4.9 shows the TFM images of setup 2. For notch B1 in Fig. 4.9(a), just the TT-T mode was used, and only the TT-TT mode for notch B3 [Fig. 4.9(b)]. These ray paths correspond to the transversal mode half-skip, TT-T (forward, reflection, and backward), and full-skip, TT-TT (forward, forward reflection, backward reflection, and backward). A reduction in the background noise as well as in the magnitude of the artifacts in CS-FMC can be seen for notch B1. A similar behavior is seen for notch B3, where the CS-FMC image showed less background noise relative to the FMC. Furthermore, the sparse CS image of notch B1 is almost a faithful representation of the reference image. Some artifacts can be seen in the sparse CS image of Fig. 4.9(b), which did not influence the interpretation of the results and notch detection. The notch from the sparse CS image remained visible as did the notches in the FMC and CS-FMC images. It can also be seen that the CS reconstruction is efficient regardless of the flaw angle.

Fig. 4.10 presents the CNR results for setup 2. Fig. 4.10(a) displays the results for notch B1 and Fig. 4.10(b) for notch B3. It can be seen that the CS-FMC presents a superior image quality as compared to the FMC. In this case, the size of the collected FMC dataset was considerably reduced, and at the same time, the CNR improved. Further data reduction was achieved with the sparse CS images, and the performance in terms of CNR was within 8% of the FMC results. Table 4.4 shows the results for sizing and position difference of the notches. The compressed reconstruction also did not affect the defect size and its position in the double-layer medium inspection. Notch B1 showed a maximum of 2% variation in position and a 5% difference in size. For notch B3, the face length of the defect corresponds to its size and was computed using simple trigonometry. In this case, the position results are within 5% of the actual sample, whereas for the size they are 6%.
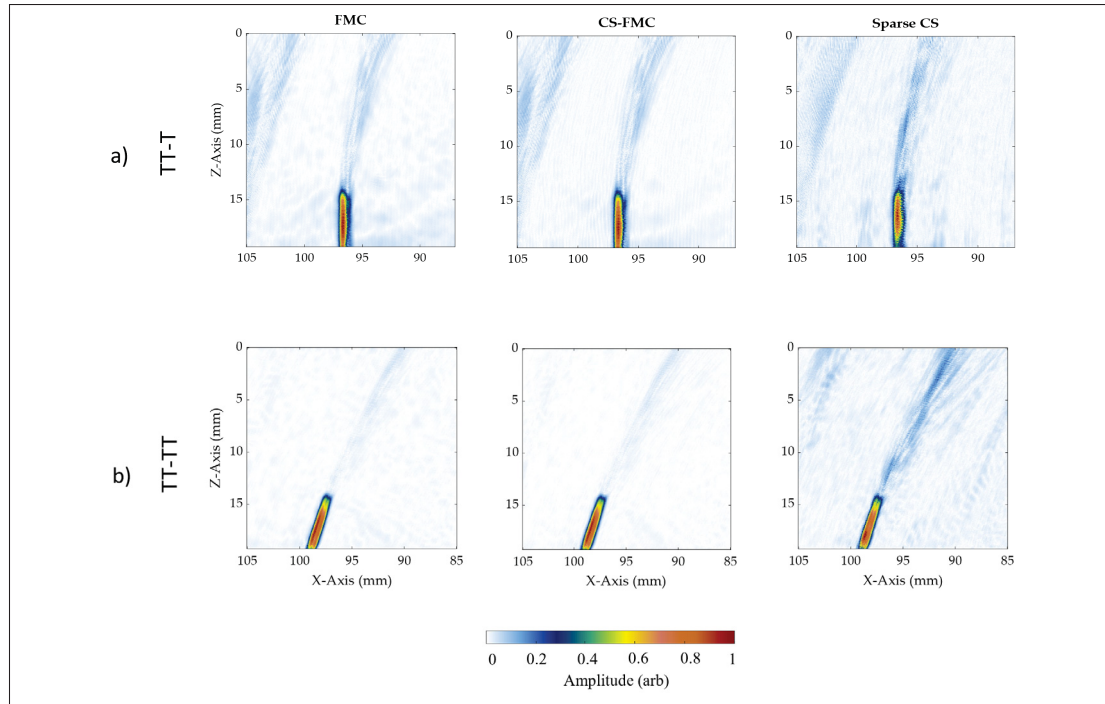
Figure 4.9   TFM images obtained using FMC, CS-FMC, and sparse CS experimental datasets of setup 2 for the notches (a) B1 and (b) B3. Improvements in image quality are noted when comparing FMC and CS-FMC. The sparse CS images are a close representation of FMC despite the drastic reduction in firing events in the latter
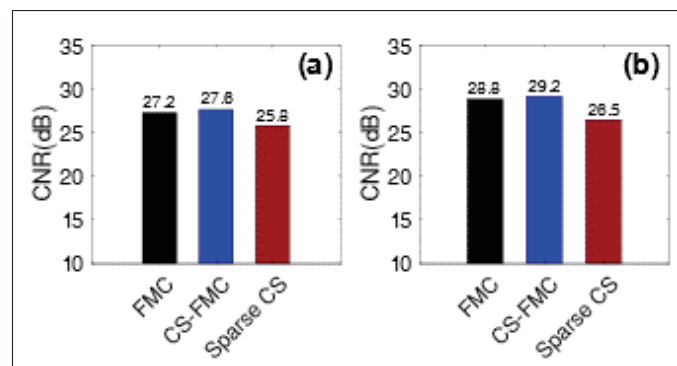
Figure 4.10   CNR bar graphs of notch (a) B1 and (b) B3 measured from the images shown in Fig. 9 regarding each acquisition method used

Table 4.4   Variation of notch position and size
with respect to the actual test sample

	CS-FMC/Actual			Sparse CS/Actual		
SDH number	$\delta x(\%)$	$\delta z(\%)$	$\delta s(\%)$	$\delta x(\%)$	$\delta z(\%)$	$\delta s(\%)$
B1	2	2	0	2	1	5
B3	1	5	4	1	6	6

4.5.4   Computational time

The temporal aspect is essential for fast TFM imaging. It was shown that the CS-FMC approach could reduce the data volumes by 80%. However, CS-FMC operation demands long reconstruction times, which represents an obstacle to rapid image processing, and therefore, implementation of sparse arrays was suggested. To examine CS reconstruction time reduction, the computational times from CS-FMC and sparse CS methods were measured and the respective variations were computed. The image formation times from FMC and sparse CS methods were also measured to estimate the TFM imaging acceleration. For the sake of brevity, only the reconstruction times for HBP are presented in Fig. 4.11. In this case, CS reconstruction was performed using the FMC matrix of dimensions $2048 \times 64 \times 64$ (A-scan length, number of transmitted channels, number of received channels). Fig. 4.11 shows that it takes about 1,384s to complete the CS reconstruction for CS-FMC and 109s for sparse CS, thus a reduction of 92%. Also, a reduction of 89% is observed for TFM imaging time using sparse CS. One can see that the total time of CS-FMC is higher than FMC due to the longer CS reconstruction time. On the other hand, sparse CS total time result is close to FMC. For the remaining setup configurations, a percentage variation is presented. Table 4.5 shows the computation time reduction $\delta t\%$ of CS reconstruction using the sparse CS method relative to CS-FMC and sparse CS TFM imaging time reduction relative to FMC for all setups. It can be seen that the implementation of sparse arrays reduced the CS reconstruction time by up to 92%. Because the CS reconstruction procedure is sequentially repeated for all A-scans, the total computation time is linearly dependent on the number of reconstructed signals. Therefore, the time reduction is also proportional to the number of deactivated elements in transmission, which corresponds to 92% in setup 1 and 91% in setup 2 considering $N_{actv} = 5$ and total element count (see Table 4.1). These results are illustrated by

the example provided in Fig. 4.11 for HBP. Furthermore, the sparse CS TFM imaging is 85% faster on average than FMC. This indicates, for example, that the sparse CS approach would only require 3s to image the same ROI of an FMC with 20s of computation time (TFM imaging 6.6 times faster in practice). It should be noted that the CS framework alone grants faster data processing, and consequently, faster ultrasonic imaging thanks to the lower sampling frequency used in the recovery (12.5 MHz). This may also contribute to accelerating TFM imaging and would be combined with the time reductions from Table 4.5 to further decrease imaging time.
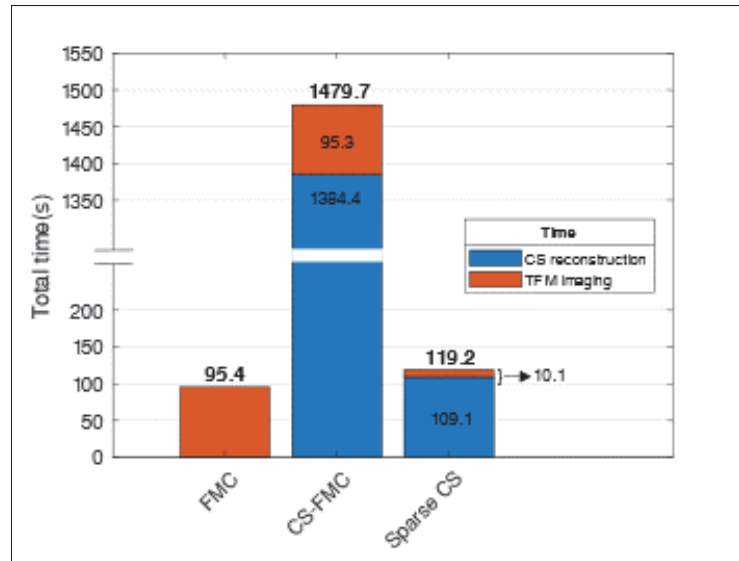
Figure 4.11   Total reconstruction time of
CS-FMC and sparse CS approaches compared
to FMC for HBP, setup 1

Table 4.5   Computational time reduction $\delta t (\%)$
of sparse CS data reconstruction compared to
CS-FMC, and sparse CS TFM imaging
compared to FMC. Reductions are displayed for
each setup used

	Setup 1 (SDH Inspection)		Setup 2 (Angled Notch Inspection)	
	VBP	HBP	B1	B3
Sparse CS reconstr.	92	92	91	91
Sparse CS imaging	85	89	83	84

4.6   Discussion

Regarding signal reconstruction, the proposed CS approach was able to accurately recover the FMC ultrasonic signals from under-sampled measurements. An average PRD was computed for each reconstructed FMC dataset of setups 1 and 2, and a global average error from the four reconstructed datasets was estimated. The global average error calculated was 11.2%, which is an acceptable result considering the applied CR of 80%. Such a drastic reduction of points inevitably leads to reconstruction errors. This is represented by the artifacts present in the reconstructed signal in Fig. 4.5(c). At first glance, these artifacts could be interpreted as random noise. In reality, the artifacts are not noise, but rather, a result of random under-sampling. The under-sampling leads to energy leakage from the nonzero coefficients that end up within the recovered signal coefficients, which were originally zero elements (Lustig, Donoho & Pauly, 2007). Some authors have suggested the possibility of computing this leakage to mitigate such errors (Donoho, Tsaig, Drori & Starck, 2012). However, with the implementation of the optimal CS matrices as suggested in this work, the reconstruction errors were minimized, as shown in Figs. 4.3, 4.4, and 4.5, achieving a satisfactory reconstruction even though a 5-fold under-sampling was applied. It should be noted that the CS method was not used in the experimental sampling process. In this work, high-dimensional data was post-processed to demonstrate the feasibility of using CS to reconstruct FMC ultrasonic signals at the sub-Nyquist rate for later implementation in an actual acquisition system. It is known that the data processed by the scanners are uniformly sampled, and thus not suitable for CS reconstructions, which ultimately requires random sampling for successful signal recovery. The findings of this work can therefore be extended to the design of an actual hardware architecture acquisition device, where the CS would be involved in the sampling procedure as demonstrated.

By analyzing the TFM images from the setups used, it can be seen that the CS-FMC images often showed an image quality that was better than or similar to that with the fully sampled FMC. This is a result of the wavelet transform implementation. Because the DWT allows the localization of data components at multiple scales, the relevant information of the signal can be preserved while the noise is reduced. This result can be seen in the CS-TFM images in Figs. 4.6,

4.7, and 4.9, where the level of background noise or the amplitude of the artifacts was reduced. Consequently, the CNR was increased in these cases. Most low-amplitude defects still present a slight reduction in CNR. As mentioned before, under-sampling leads to the appearance of artifacts in the recovered signal. Lower amplitude indications in the signal such as the ones from SDH 4 and 5 in VBP may fall closer to this "noise level" when reconstructed, resulting in a lower CNR. These findings represent one of the limitations of the proposed method and can be generalized to other deep, weak reflecting targets and flaws found outside the probe aperture. Regardless of the presence of such errors and small losses, no significant variation in flaw size and position was seen for both setups, demonstrating the viability of the proposed compressed reconstruction. This is an important result in terms of FMC data size reduction as well as signal processing efficiency.

The CS-FMC achieved high image quality with a reduced generated data size, but at the expense of longer CS reconstruction times. The CS-FMC computation time is linearly proportional to the number of reconstructed A-scans, as the CS reconstruction is performed sequentially for all signals. The sparse array approach was therefore suggested to overcome this issue, in addition to further reducing the data size and TFM imaging time. The CS reconstruction computation time saw an overall reduction of 90% using the minimum firing events sparse design, as the number of A-scans collected and processed fell drastically with $N_{actv} = 5$. Some losses were expected using such a small number of transmissions, due to the reduction of frames used to generate the TFM image. Sparse CS results showed image quality within 8% of the FMC for setup 2, while for setup 1, the maximum variation was 15% when considering the low amplitude defects. On the other hand, results comparable to CS-FMC were seen for the flaw position and sizing (see Tables 4.2–4.4). The sparse CS performance can be considered close to that of FMC with a small reduction in CNR. This is thanks to the fact that the data contained in FMC is redundant (Karaman *et al.*, 2009), and therefore, a proper selection of the sparse elements, such as the layouts used herein, can achieve similar TFM results but with way less data (Piedade *et al.*, 2022). In sparse CS imaging, the number of firing events dropped to 92% on average,

considering both setups, which allowed practical TFM image processing 6.6 times faster than with FMC.

Current commercial ultrasonic scanners are typically set to sampling frequencies between 4 to 10 times the probe central frequency, as in the case of the Verasonics Vantage system. In this proof of concept, the results of the proposed CS framework indicate that using sampling rates under the Nyquist theorem limit is possible. This corresponds to a theoretical data processing that is 5 times faster, considering the SR used for CS reconstructions (12.5 MHz) and the one corresponding to the actual system. When applied to sparse arrays, such a compressed method was shown to be viable for reducing the TFM computation cost and allows to mitigate the hardware complexity of conventional ultrasound systems.

4.7 Conclusion

In this work, we have presented a compressed sensing framework applied to ultrasonic sparse arrays for lightweight and faster TFM imaging. Based on sparseness and incoherence measurements, a DWT featuring six-level of decomposition of the coif5 wavelet and the Gaussian random were selected as the optimal matrices for signal reconstruction. The proposed CS strategy can recover experimental FMC A-scans with fewer points than required by the Nyquist sampling theorem. These results point to theoretical data processing 5 times faster than with existing acquisition systems, and an 80% reduction in the volume of FMC data to be stored and transmitted. In addition, the adopted sparse array design resulted in an eleven-fold CS reconstruction time improvement and TFM imaging that was 6.6 times faster, with only a minor drop in image quality. These results can potentially lead to the practical implementation of low-processing power hardware in NDT applications. Moreover, this method can be extended to the design of a simple hardware architecture acquisition device. For future work, parallel computation using a graphics processing unit (GPU) can be applied to optimize the CS reconstruction time, as the signals are independently processed.

CONCLUSION AND RECOMMENDATIONS

The research undertaken in this thesis comprises a multifaceted investigation aimed at enhancing the productivity and efficiency of ultrasonic TFM imaging using sparse array designs and advanced data compression techniques. In particular, this work tackled the constraints related to employing ultrasonic matrix phased arrays in 3-D TFM, aiming to broaden the technology's application in NDT industrial sectors. The production of three distinct manuscripts contributes significantly to the advancement of this subject in NDT, particularly regarding reducing transmission events, optimizing sparse array layouts, and employing compressive sensing for faster TFM imaging. For that, experimental trials were carried out on different types of samples containing artificial flaws, such as SDH and EDM notches, to evaluate the performance of the proposed approach.

An initial study presented a novel approach to designing optimal sparse array layouts, introducing the minimum transmission event (MTE) method. Comparative studies between two types of sparse array configurations and PWI revealed the superiority of the MTE approach, achieving improved CNR and API for axial and lateral defects. The findings demonstrated that using just 7.8% of FMC data, the MTE approach produced comparable images to FMC, demonstrating a remarkable 92.2% reduction in firing events. Alternatively, an equally spaced arrangement with edge elements deactivation yielded results comparable to the optimal layout, maintaining a difference within 9% without necessitating computations. These results highlight the efficacy of this method in significantly enhancing TFM productivity, offering promising prospects for industrial applications of ultrasonic phased arrays.

The subsequent work introduced advancements in accelerating 3-D TFM imaging by optimizing wideband 2-D sparse arrays through an adaptation of the MTE approach, now referred to as the minimum firing event method. A refinement stage was proposed to reduce the computational load of this analysis by more than 96% without compromising sparse array performance. Results

revealed that a 2-D sparse array pattern with only 6 active transmitting elements replicated the imaging and sizing performance of a complete array, offering a 9.8-fold acceleration in volumetric TFM processing. Furthermore, the study showed the practical value of creating suboptimal sparse arrays without extensive exploration, thereby streamlining the design process for 2-D probes.

Lastly, a compressive sensing framework applied to ultrasonic sparse arrays, focusing on lightweight and faster TFM imaging was explored. The proposed strategy exhibited the potential to recover experimental FMC data with fewer sampling points than the Nyquist sampling theorem necessitates, leading to an 80% reduction in data volume. The adopted sparse array design from the previous studies resulted in significant improvements, achieving an 11-fold reduction in CS reconstruction time and accelerating TFM imaging by 6.6 times while maintaining acceptable image quality. These findings pave the way for the practical implementation of low-processing power hardware in NDT applications.

In summation, the collective contributions of these manuscripts advance the frontiers of ultrasonic NDT by introducing innovative sparse array designs, efficient data compression techniques, and streamlined methodologies, significantly improving TFM imaging productivity. The outcomes of this research have substantial implications for industrial applications, offering promising avenues for faster, more efficient, and practical implementation of volumetric ultrasonic imaging in the evaluation and detection of flaws across various industries.

Future research should focus on key aspects to complement this work and to advance this research field, addressing some of the following observed limitations. Firstly, exploring and implementing other algorithms to expand the optimal sparse layout search beyond the capabilities of the minimum firing event method holds promise to further improve image quality relative to FMC while maintaining rapid inspection capabilities. Furthermore, practical implementation and enhancement of CS in real-world scenarios present a significant avenue for future investigation.

Integrating sparse CS frameworks with GPU-optimized parallel computation to enhance CS reconstruction time is a prospect to facilitate faster processing of voluminous data acquired during ultrasonic inspections based on 2-D transducers. Lastly, efforts should also concentrate on mitigating reconstruction errors observed in the sparse CS method, particularly in scenarios involving deep, weak reflecting targets in the recovered FMC datasets that subsequently produced image artifacts.

APPENDIX I

SPARSE COMPRESSIVE SENSING APPLIED TO 3-D TFM IMAGING

1. CS-based 2-D sparse methodology and findings: A summary

Considering that the CS methodology presented in Chapter 4 can be applied to the recovery of any A-scan collected with an array, we utilized this technique with 2-D array FMC data. The dataset employed was identical to the one collected in Chapter 3, obtained using the matrix phased array in contact with an aluminum sample containing SDHs at various depths. The CS procedure consists of removing some parts of the original signal acquired using the FMC method. In this case, only the signals corresponding to the FMC and optimal 2-D sparse array design were taken into consideration for comparison. To ensure that the number of sampling points remained below the Nyquist limit, a compression ratio of 85% was utilized. This compression was executed using random Bernoulli distributions of 1s and 0s, which reflects a possible CS hardware implementation scenario involving binary representation. A successful recovery was achieved using just 4 levels of decomposition with the coif5 discrete wavelet transform, which was determined as the optimal transform basis in our previous work from Chapter 4.

Subsequently, the signals were decompressed using the inverse wavelet transform and the TFM algorithm was applied. The figures corresponding to this analysis are displayed in the next section along with a table showing the CNR variation for each analyzed SDH relative to FMC. The findings about image formation time remained the same as those in Chapter 4: the 2-D sparse array approach achieved approximately a 95% reduction in firing events and imaging is 9.8 times faster than the FMC. However, for the 3-D case, the sparse CS imaging was performed with 85% data compression (less than required by the Nyquist sampling theorem for this case). It is worth noting that in this instance, CS reconstruction using the Opt6 layout was approximately 20.2 times faster. Also, a minor penalty in image quality was observed for low-amplitude reflectors.

1.1 Figures and table in appendix
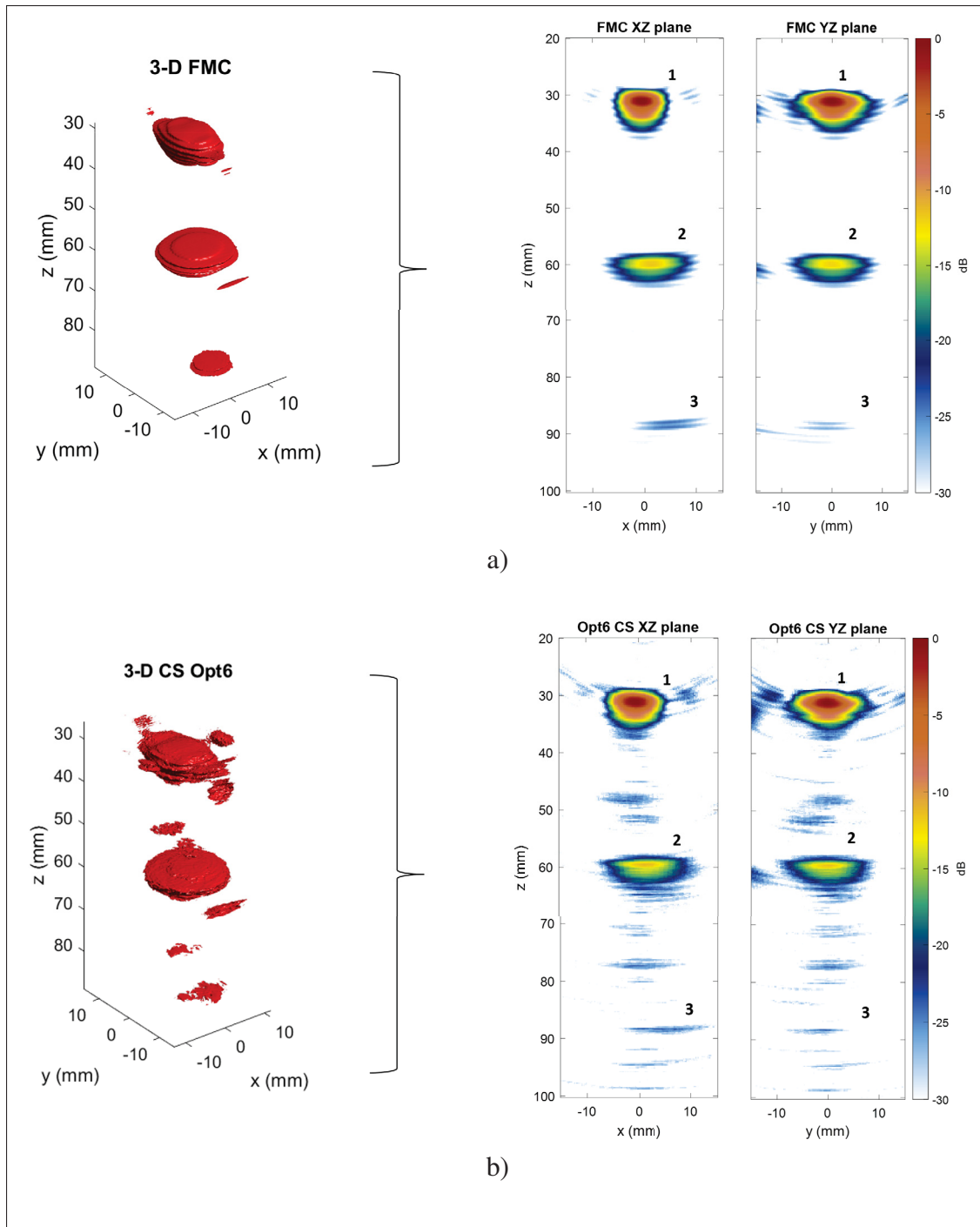
Figure-A I-1   Experimental ultrasonic 3-D TFM images and corresponding
2-D image slices: (a) FMC and (b) CS Opt6

Table-A I-1   CNR variation $\Delta(\%)$ results from the CS Opt6 compared to FMC

	CNR $\Delta(\%)$	
SDH	**XZ**	**YZ**
1	1	1
2	5	6
3	14	16

BIBLIOGRAPHY

Achim, A., Buxton, B., Tzagkarakis, G. & Tsakalides, P. (2010). Compressive sensing for ultrasound RF echoes using a-Stable Distributions. *2010 Annual International Conference of the IEEE Engineering in Medicine and Biology*, pp. 4304-4307. doi: 10.1109/IEMBS.2010.5626210.

Adler, D. (1993). Genetic algorithms and simulated annealing: a marriage proposal. *IEEE International Conference on Neural Networks*, pp. 1104-1109 vol.2. doi: 10.1109/ICNN.1993.298712.

Austeng, A. & Holm, S. (2002). Sparse 2-D arrays for 3-D phased array imaging - design methods. *IEEE Transactions on Ultrasonics, Ferroelectrics, and Frequency Control*, 49(8), 1073-1086. doi: 10.1109/TUFFC.2002.1026019.

Austeng, A., Holm, S., Weber, P., Aakvaag, N. & Iranpour, K. (1997). 1D and 2D algorithmically optimized sparse arrays. *1997 IEEE Ultrasonics Symposium Proceedings. An International Symposium (Cat. No.97CH36118)*, 2, 1683-1686. doi: 10.1109/ULTSYM.1997.663319.

Bai, L., Velichko, A. & Drinkwater, B. W. (2015). Characterization of defects using ultrasonic arrays: a dynamic classifier approach. *IEEE Transactions on Ultrasonics, Ferroelectrics, and Frequency Control*, 62(12), 2146-2160. doi: 10.1109/TUFFC.2015.007334.

Bai, Z., Chen, S., Jia, L. & Zeng, Z. (2017). Phased array ultrasonic signal compressive detection in low-pressure turbine disc. *NDT & E International*, 89, 1-13. doi: https://doi.org/10.1016/j.ndteint.2017.03.002.

Bai, Z., Chen, S., Jia, L. & Zeng, Z. (2018a). Ultrasonic Phased Array Compressive Imaging in Time and Frequency Domain: Simulation, Experimental Verification and Real Application. *Sensors*, 18(5). doi: 10.3390/s18051460.

Bai, Z., Chen, S., Xiao, Q., Jia, L., Zhao, Y. & Zeng, Z. (2018b). Compressive sensing of phased array ultrasonic signal in defect detection: Simulation study and experimental verification. *Structural Health Monitoring*, 17(3), 434-449. doi: 10.1177/1475921717701462.

Bannouf, S., Robert, S., Casula, O. & Prada, C. (2013). Data set reduction for ultrasonic TFM imaging using the effective aperture approach and virtual sources. *Journal of Physics: Conference Series*, 457(1), 012007. doi: 10.1088/1742-6596/457/1/012007.

Bao, Y., Li, H., Sun, X., Yu, Y. & Ou, J. (2013). Compressive sampling–based data loss recovery for wireless sensor networks used in civil structural health monitoring. *Structural Health Monitoring*, 12(1), 78-95. doi: 10.1177/1475921712462936.

124

Baraniuk, R. G. (2007). Compressive Sensing [Lecture Notes]. *IEEE Signal Processing Magazine*, 24(4), 118-121. doi: 10.1109/MSP.2007.4286571.

Brunelli, D. & Caione, C. (2015). Sparse Recovery Optimization in Wireless Sensor Networks with a Sub-Nyquist Sampling Rate. *Sensors*, 15(7), 16654–16673. doi: 10.3390/s150716654.

Brunke, S. & Lockwood, G. (1997). Broad-bandwidth radiation patterns of sparse two-dimensional vernier arrays. *IEEE Transactions on Ultrasonics, Ferroelectrics, and Frequency Control*, 44(5), 1101-1109. doi: 10.1109/58.655635.

Candes, E. & Tao, T. (2005). Decoding by linear programming. *IEEE Transactions on Information Theory*, 51(12), 4203-4215. doi: 10.1109/TIT.2005.858979.

Candes, E., Romberg, J. & Tao, T. (2006). Robust uncertainty principles: exact signal reconstruction from highly incomplete frequency information. *IEEE Transactions on Information Theory*, 52(2), 489-509. doi: 10.1109/TIT.2005.862083.

Candès, E. J. & Romberg, J. K. (2005). 11-magic : Recovery of sparse signals via convex programming. Retrieved from: https://api.semanticscholar.org/CorpusID:1038158.

Candes, E. J. & Tao, T. (2006). Near-Optimal Signal Recovery From Random Projections: Universal Encoding Strategies? *IEEE Transactions on Information Theory*, 52(12), 5406-5425. doi: 10.1109/TIT.2006.885507.

Candes, E. J. & Wakin, M. B. (2008). An Introduction To Compressive Sampling. *IEEE Signal Processing Magazine*, 25(2), 21-30. doi: 10.1109/MSP.2007.914731.

Candès, E. & Becker, S. (2013). Compressive sensing: Principles and hardware implementations. *2013 Proceedings of the ESSCIRC (ESSCIRC)*, pp. 22-23. doi: 10.1109/ESSCIRC.2013.6649062.

Cheeke, J. D. N. (2012). *Fundamentals and Applications of Ultrasonic Waves* (ed. 2). Boca Rato, USA: CRC Press. doi: https://doi.org/10.1201/b12260.

Clark, R. (2004). Rail flaw detection: overview and needs for future developments. *NDT & E International*, 37(2), 111-118. doi: https://doi.org/10.1016/j.ndteint.2003.06.002.

Cosarinsky, G., Cruza, J., Muñoz, M. & Camacho, J. (2023). Optimized auto-focusing method for 3D ultrasound imaging in NDT. *NDT & E International*, 134, 102779. doi: https://doi.org/10.1016/j.ndteint.2022.102779.

Couture, O., Fink, M. & Tanter, M. (2012). Ultrasound contrast plane wave imaging. *IEEE Transactions on Ultrasonics, Ferroelectrics, and Frequency Control*, 59(12), 2676-2683. doi: 10.1109/TUFFC.2012.2508.

Dabrowski, W., Dunmore-Buyze, J., Cardinal, H. N. & Fenster, A. (2001). A real vessel phantom for flow imaging: 3-D Doppler ultrasound of steady flow. *Ultrasound in medicine & biology*, 27(1), 135–141. doi: https://doi.org/10.1016/s0301-5629(00)00277-5.

Davidsen, R. E., Jensen, J. A. & Smith, S. W. (1994). Two-Dimensional Random Arrays for Real Time Volumetric Imaging. *Ultrasonic Imaging*, 16(3), 143-163. doi: 10.1177/016173469401600301.

Diarra, B., Liebgott, H., Tortoli, P. & Cachard, C. (2011). 2D matrix array optimization by simulated annealing for 3D hepatic imaging. *2011 IEEE International Ultrasonics Symposium*, pp. 1595-1598. doi: 10.1109/ULTSYM.2011.0396.

Diarra, B., Liebgott, H., Robini, M., Tortoli, P. & Cachard, C. (2012). Optimized 2D array design for Ultrasound imaging. *2012 Proceedings of the 20th European Signal Processing Conference (EUSIPCO)*, pp. 2718-2722.

Diarra, B., Robini, M., Tortoli, P., Cachard, C. & Liebgott, H. (2013). Design of Optimal 2-D Nongrid Sparse Arrays for Medical Ultrasound. *IEEE Transactions on Biomedical Engineering*, 60(11), 3093-3102. doi: 10.1109/TBME.2013.2267742.

Diarra, B., Roux, E., Liebgott, H., Ravi, S., Robini, M., Tortoli, P. & Cachard, C. (2016). Comparison of different optimized irregular sparse 2D ultrasound arrays. *2016 IEEE International Ultrasonics Symposium (IUS)*, pp. 1-4. doi: 10.1109/ULTSYM.2016.7728414.

Donoho, D. L., Tsaig, Y., Drori, I. & Starck, J.-L. (2012). Sparse Solution of Underdetermined Systems of Linear Equations by Stagewise Orthogonal Matching Pursuit. *IEEE Transactions on Information Theory*, 58(2), 1094-1121. doi: 10.1109/TIT.2011.2173241.

Donoho, D. (2006). Compressed sensing. *IEEE Transactions on Information Theory*, 52(4), 1289-1306. doi: 10.1109/TIT.2006.871582.

Donoho, D. & Huo, X. (2001). Uncertainty principles and ideal atomic decomposition. *IEEE Transactions on Information Theory*, 47(7), 2845-2862. doi: 10.1109/18.959265.

Downey, D. B., Nicolle, D. A., Levin, M. F. & Fenster, A. (1996). Three-dimensional ultrasound imaging of the eye. *Eye*, 10, 75–81. doi: https://doi.org/10.1038/eye.1996.11.

Drinkwater, B. W. & Wilcox, P. D. (2006). Ultrasonic arrays for non-destructive evaluation: A review. *NDT & E International*, 39(7), 525-541. doi: https://doi.org/10.1016/j.ndteint.2006.03.006.

Ensminger, D. & Bond, L. J. (2011). *Ultrasonics: Fundamentals, technologies, and applications* (ed. 3). Boca Rato, USA: CRC Press.

Fan, C., Caleap, M., Pan, M. & Drinkwater, B. W. (2014). A comparison between ultrasonic array beamforming and super resolution imaging algorithms for non-destructive evaluation. *Ultrasonics*, 54(7), 1842-1850. doi: https://doi.org/10.1016/j.ultras.2013.12.012.

Felice, M. V. & Fan, Z. (2018). Sizing of flaws using ultrasonic bulk wave testing: A review. *Ultrasonics*, 88, 26-42. doi: https://doi.org/10.1016/j.ultras.2018.03.003.

Fernandez, A., Gammelmark, K., Dahl, J., Keen, C., Gauss, R. & Trahey, G. (2003). Synthetic elevation beamforming and image acquisition capabilities using an 8 /spl times/ 128 1.75D array. *IEEE Transactions on Ultrasonics, Ferroelectrics, and Frequency Control*, 50(1), 40-57. doi: 10.1109/TUFFC.2003.1176524.

Gilja, O. H., Smievoll, A. I., Thune, N., Matre, K., Hausken, T., Odegaard, S. & Berstad, A. (1995). In vivo comparison of 3D ultrasonography and magnetic resonance imaging in volume estimation of human kidneys. *Ultrasound in medicine & biology*, 21(1), 25–32. doi: https://doi.org/10.1016/0301-5629(94)00082-4.

Guo, W., Wang, Y., Wu, G. & Yu, J. (2018). Sidelobe reduction for plane wave compounding with a limited frame number. *BioMedical Engineering OnLine*, 17(1), 1-21. doi: 10.1186/s12938-018-0525-1.

Halmshaw, R. (1997). *Introduction to the Non-Destructive Testing of Welded Joints* (ed. 2). Abingdon, UK: Woodhead Publishing.

Holmes, C., Drinkwater, B. W. & Wilcox, P. D. (2005). Post-processing of the full matrix of ultrasonic transmit–receive array data for non-destructive evaluation. *NDT & E International*, 38(8), 701-711. doi: https://doi.org/10.1016/j.ndteint.2005.04.002.

Hoyer, P. O. (2004). Non-negative matrix factorization with sparseness constraints. *Journal of machine learning research*, 5(9). doi: 10.48550/arXiv.cs/0408058.

Hoyle, E., Sutcliffe, M., Charlton, P. & Rees, J. (2018). Virtual source aperture imaging with auto-focusing of unknown complex geometry through dual layered media. *NDT & E International*, 98, 55-62. doi: https://doi.org/10.1016/j.ndteint.2018.04.005.

Hu, H., Du, J., Xu, N., Jeong, H. & Wang, X. (2017). Ultrasonic sparse-TFM imaging for a two-layer medium using genetic algorithm optimization and effective aperture correction. *NDT & E International*, 90, 24-32. doi: https://doi.org/10.1016/j.ndteint.2017.05.002.

Hughes, S., D'Arcy, T., Maxwell, D., Chiu, W., Milner, A., Saunders, J. & Sheppard, R. (1996). Volume estimation from multiplanar 2D ultrasound images using a remote electromagnetic position and orientation sensor. *Ultrasound in Medicine & Biology*, 22(5), 561-572. doi: https://doi.org/10.1016/0301-5629(96)00022-1.

Hwang, S.-F. & He, R.-S. (2006). Improving real-parameter genetic algorithm with simulated annealing for engineering problems. *Advances in Engineering Software*, 37(6), 406-418. doi: https://doi.org/10.1016/j.advengsoft.2005.08.002.

Jensen, J. A., Holten-Lund, H., Nilsson, R. T., Hansen, M., Larsen, U. D., Domsten, R. P., Tomov, B. G., Stuart, M. B., Nikolov, S. I., Pihl, M. J., Du, Y., Rasmussen, J. H. & Rasmussen, M. F. (2013). SARUS: A synthetic aperture real-time ultrasound system. *IEEE Transactions on Ultrasonics, Ferroelectrics, and Frequency Control*, 60(9), 1838-1852. doi: 10.1109/TUFFC.2013.2770.

Karaman, M., Wygant, I. O., Oralkan, O. & Khuri−Yakub, B. T. (2009). Minimally Redundant 2-D Array Designs for 3-D Medical Ultrasound Imaging. *IEEE Transactions on Medical Imaging*, 28(7), 1051-1061. doi: 10.1109/TMI.2008.2010936.

Kruizinga, P., van der Meulen, P., Fedjajevs, A., Mastik, F., Springeling, G., de Jong, N., Bosch, J. G. & Leus, G. (2017). Compressive 3D ultrasound imaging using a single sensor. *Science Advances*, 3(12), e1701423. doi: 10.1126/sciadv.1701423.

Lane, C. J. L., Dunhill, T., Drinkwater, B. W. & Wilcox, P. D. (2010). 3D ultrasonic inspection of anisotropic aerospace components. *Insight*, 52, 72-77. Retrieved from: https://api.semanticscholar.org/CorpusID:110401338.

Le Jeune, L., Robert, S., Lopez Villaverde, E. & Prada, C. (2016). Plane Wave Imaging for ultrasonic non-destructive testing: Generalization to multimodal imaging. *Ultrasonics*, 64, 128-138. doi: https://doi.org/10.1016/j.ultras.2015.08.008.

Levine, R. A., Handschumacher, M. D., Sanfilippo, A. J., Hagege, A. A., Harrigan, P., Marshall, J. E. & Weyman, A. E. (1989). Three-dimensional echocardiographic reconstruction of the mitral valve, with implications for the diagnosis of mitral valve prolapse. *Circulation*, 80(3), 589–598. doi: https://doi.org/10.1161/01.cir.80.3.589.

Lewandowski, M., Walczak, M., Witek, B., Rozbicki, J. & Steifer, T. (2018). A GPU-Based Portable Phased-Array System with Full-Matrix Capture. *2018 IEEE International Ultrasonics Symposium (IUS)*, pp. 1-3. doi: 10.1109/ULTSYM.2018.8579964.

Li, C., Pain, D., Wilcox, P. D. & Drinkwater, B. W. (2013). Imaging composite material using ultrasonic arrays. *NDT & E International*, 53, 8-17. doi: https://doi.org/10.1016/j.ndteint.2012.07.006.

Li, Z. & Chi, C. (2018). Fast computation of far-field pulse-echo PSF of arbitrary arrays for large sparse 2-D ultrasound array design. *Ultrasonics*, 84, 63-73. doi: https://doi.org/10.1016/j.ultras.2017.10.006.

Liu, J. & Luo, J. (2018). Compressed Sensing Based Synthetic Transmit Aperture for Phased Array Using Hadamard Encoded Diverging Wave Transmissions. *IEEE Transactions on Ultrasonics, Ferroelectrics, and Frequency Control*, 65(7), 1141-1152. doi: 10.1109/TUFFC.2018.2832058.

Liu, J., He, Q. & Luo, J. (2017). A Compressed Sensing Strategy for Synthetic Transmit Aperture Ultrasound Imaging. *IEEE Transactions on Medical Imaging*, 36(4), 878-891. doi: 10.1109/TMI.2016.2644654.

Lockwood, G., Li, P.-C., O'Donnell, M. & Foster, F. (1996). Optimizing the radiation pattern of sparse periodic linear arrays. *IEEE Transactions on Ultrasonics, Ferroelectrics, and Frequency Control*, 43(1), 7-14. doi: 10.1109/58.484457.

Lockwood, G., Talman, J. & Brunke, S. (1998). Real-time 3-D ultrasound imaging using sparse synthetic aperture beamforming. *IEEE Transactions on Ultrasonics, Ferroelectrics, and Frequency Control*, 45(4), 980-988. doi: 10.1109/58.710573.

Lorintiu, O., Liebgott, H., Alessandrini, M., Bernard, O. & Friboulet, D. (2015). Compressed Sensing Reconstruction of 3D Ultrasound Data Using Dictionary Learning and Line-Wise Subsampling. *IEEE Transactions on Medical Imaging*, 34(12), 2467-2477. doi: 10.1109/TMI.2015.2442154.

Lustig, M., Donoho, D. & Pauly, J. M. (2007). Sparse MRI: The application of compressed sensing for rapid MR imaging. *Magnetic resonance in medicine*, 58(6), 1182—1195. doi: 10.1002/mrm.21391.

Mansur Rodrigues Filho, J. F. & Bélanger, P. (2021). Probe Standoff Optimization Method for Phased Array Ultrasonic TFM Imaging of Curved Parts. *Sensors*, 21(19). doi: 10.3390/s21196665.

Marmonier, M., Robert, S., Laurent, J. & Prada, C. (2022). Real-time 3D imaging with Fourier-domain algorithms and matrix arrays applied to non-destructive testing. *Ultrasonics*, 124, 106708. doi: https://doi.org/10.1016/j.ultras.2022.106708.

Martínez-Graullera, O., Martín, C. J., Godoy, G. & Ullate, L. G. (2010). 2D array design based on Fermat spiral for ultrasound imaging. *Ultrasonics*, 50(2), 280-289. doi: https://doi.org/10.1016/j.ultras.2009.09.010.

McKee, J. G., Wilcox, P. D. & Malkin, R. E. (2019). Effect of surface compensation for imaging through doubly-curved surfaces using a 2D phased array. *AIP Conference Proceedings*, 2102(1), 100008. doi: 10.1063/1.5099836.

McKee, J. G., Bevan, R. L., Wilcox, P. D. & Malkin, R. E. (2020). Volumetric imaging through a doubly-curved surface using a 2D phased array. *NDT & E International*, 113, 102260. doi: https://doi.org/10.1016/j.ndteint.2020.102260.

Montaldo, G., Tanter, M., Bercoff, J., Benech, N. & Fink, M. (2009). Coherent plane-wave compounding for very high frame rate ultrasonography and transient elastography. *IEEE Transactions on Ultrasonics, Ferroelectrics, and Frequency Control*, 56(3), 489-506. doi: 10.1109/TUFFC.2009.1067.

Moreau, L., Drinkwater, B. W. & Wilcox, P. D. (2009). Ultrasonic imaging algorithms with limited transmission cycles for rapid nondestructive evaluation. *IEEE Transactions on Ultrasonics, Ferroelectrics, and Frequency Control*, 56(9), 1932-1944. doi: 10.1109/TUFFC.2009.1269.

Nikolov, S., Jensen, J., Dufait, R. & Schoisswohl, A. (2002). Three-dimensional real-time synthetic aperture imaging using a rotating phased array transducer. *2002 IEEE Ultrasonics Symposium, 2002. Proceedings.*, 2, 1585-1588. doi: 10.1109/ULTSYM.2002.1192596.

Olympus. (2004). *Introduction to Phased Array Ultrasonic Technology Applications: R/D Tech Guideline*. Waltham, USA: Olympus NDT.

Park, C., Zhao, W., Park, I., Sun, N. & Chae, Y. (2021). A 51-pJ/Pixel 33.7-dB PSNR 4× Compressive CMOS Image Sensor With Column-Parallel Single-Shot Compressive Sensing. *IEEE Journal of Solid-State Circuits*, 56(8), 2503-2515. doi: 10.1109/JSSC.2021.3071875.

Perelli, A., Di Ianni, T., Marzani, A., De Marchi, L. & Masetti, G. (2013). Model-based compressive sensing for damage localization in lamb wave inspection. *IEEE Transactions on Ultrasonics, Ferroelectrics, and Frequency Control*, 60(10), 2089-2097. doi: 10.1109/TUFFC.2013.2799.

Perelli, A., De Marchi, L., Flamigni, L., Marzani, A. & Masetti, G. (2015). Best basis compressive sensing of guided waves in structural health monitoring. *Digital Signal Processing*, 42, 35-42. doi: https://doi.org/10.1016/j.dsp.2015.04.001.

Petrusca, L., Varray, F., Souchon, R., Bernard, A., Chapelon, J.-Y., Liebgott, H., N'Djin, W. A. & Viallon, M. (2018). Fast Volumetric Ultrasound B-Mode and Doppler Imaging with a New High-Channels Density Platform for Advanced 4D Cardiac Imaging/Therapy. *Applied Sciences*, 8(2). doi: 10.3390/app8020200.

Piedade, L. P., Painchaud-April, G., Le Duff, A. & Bélanger, P. (2022). Minimum transmission events for fast ultrasonic TFM imaging: A comparative study. *NDT & E International*, 128, 102627. doi: https://doi.org/10.1016/j.ndteint.2022.102627.

Piedade, L. P., Painchaud-April, G., Le Duff, A. & Bélanger, P. (2023). Compressive Sensing Strategy on Sparse Array to Accelerate Ultrasonic TFM Imaging. *IEEE Transactions on Ultrasonics, Ferroelectrics, and Frequency Control*, 70(6), 538-550. doi: 10.1109/TUFFC.2023.3266719.

Provost, J., Papadacci, C., Demene, C., Gennisson, J.-L., Tanter, M. & Pernot, M. (2015). 3-D ultrafast doppler imaging applied to the noninvasive mapping of blood vessels in Vivo. *IEEE Transactions on Ultrasonics, Ferroelectrics, and Frequency Control*, 62(8), 1467-1472. doi: 10.1109/TUFFC.2015.007032.

Pérez, E., Kirchhof, J., Krieg, F. & Römer, F. (2020). Subsampling Approaches for Compressed Sensing with Ultrasound Arrays in Non-Destructive Testing. *Sensors*, 20(23). doi: 10.3390/s20236734.

Ramadas, S. N., Jackson, J. C., Dziewierz, J., O'Leary, R. & Gachagan, A. (2014). Application of conformal map theory for design of 2-D ultrasonic array structure for ndt imaging application: a feasibility study. *IEEE Transactions on Ultrasonics, Ferroelectrics, and Frequency Control*, 61(3), 496-504. doi: 10.1109/TUFFC.2014.2933.

Ramalli, A., Boni, E., Savoia, A. S. & Tortoli, P. (2015). Density-tapered spiral arrays for ultrasound 3-D imaging. *IEEE Transactions on Ultrasonics, Ferroelectrics, and Frequency Control*, 62(8), 1580-1588. doi: 10.1109/TUFFC.2015.007035.

Ramalli, A., Boni, E., Roux, E., Liebgott, H. & Tortoli, P. (2022). Design, Implementation, and Medical Applications of 2-D Ultrasound Sparse Arrays. *IEEE Transactions on Ultrasonics, Ferroelectrics, and Frequency Control*, 69(10), 2739-2755. doi: 10.1109/TUFFC.2022.3162419.

Ramkumar, A. & Thittai, A. K. (2020a). Compressed Sensing Approach for Reducing the Number of Receive Elements in Synthetic Transmit Aperture Imaging. *IEEE Transactions on Ultrasonics, Ferroelectrics, and Frequency Control*, 67(10), 2012-2021. doi: 10.1109/TUFFC.2020.2995409.

Ramkumar, A. & Thittai, A. K. (2020b). Strategic Undersampling and Recovery Using Compressed Sensing for Enhancing Ultrasound Image Quality. *IEEE Transactions on Ultrasonics, Ferroelectrics, and Frequency Control*, 67(3), 547-556. doi: 10.1109/TUFFC.2019.2948652.

Rotman, J. J. (1995). *An Introduction to the Theory of Groups*. New York, USA: Springer. doi: https://doi.org/10.1007/978-1-4612-4176-8.

Roux, E., Ramalli, A., Tortoli, P., Cachard, C., Robini, M. C. & Liebgott, H. (2016). 2-D Ultrasound Sparse Arrays Multidepth Radiation Optimization Using Simulated Annealing and Spiral-Array Inspired Energy Functions. *IEEE Transactions on Ultrasonics, Ferroelectrics, and Frequency Control*, 63(12), 2138-2149. doi: 10.1109/TUFFC.2016.2602242.

Roux, E., Ramalli, A., Liebgott, H., Cachard, C., Robini, M. C. & Tortoli, P. (2017). Wideband 2-D Array Design Optimization With Fabrication Constraints for 3-D US Imaging. *IEEE Transactions on Ultrasonics, Ferroelectrics, and Frequency Control*, 64(1), 108-125. doi: 10.1109/TUFFC.2016.2614776.

Roux, E., Varray, F., Petrusca, L., Cachard, C., Tortoli, P. & Liebgott, H. (2018). Experimental 3-D Ultrasound Imaging with 2-D Sparse Arrays using Focused and Diverging Waves. *Scientific Reports*, 8(9108). doi: https://doi.org/10.1038/s41598-018-27490-2.

Russell, J., Long, R., Duxbury, D. & Cawley, P. (2012). Development and implementation of a membrane-coupled conformable array transducer for use in the nuclear industry. *Insight - Non-Destructive Testing and Condition Monitoring*, 54(7), 386-393. doi: doi:10.1784/insi.2012.54.7.386.

Schmerr Jr, L. W. (2014). *Fundamentals of Ultrasonic Phased Arrays*. New York, USA: Springer. doi: https://doi.org/10.1007/978-3-319-07272-2.

Schretter, C., Bundervoet, S., Blinder, D., Dooms, A., D'hooge, J. & Schelkens, P. (2018). Ultrasound Imaging From Sparse RF Samples Using System Point Spread Functions. *IEEE Transactions on Ultrasonics, Ferroelectrics, and Frequency Control*, 65(3), 316-326. doi: 10.1109/TUFFC.2017.2772916.

Sciallero, C. & Trucco, A. (2015). Design of a sparse planar array for optimized 3D medical ultrasound imaging. *2015 23rd European Signal Processing Conference (EUSIPCO)*, pp. 1341-1345. doi: 10.1109/EUSIPCO.2015.7362602.

Sciallero, C. & Trucco, A. (2021). Wideband 2-D sparse array optimization combined with multiline reception for real-time 3-D medical ultrasound. *Ultrasonics*, 111, 106318. doi: https://doi.org/10.1016/j.ultras.2020.106318.

Silva, V. M. L., Souza, C. P., Freire, R. C. S., Arruda, B. W. S., Gurjão, E. C. & Reis, V. L. (2020). Novel IEEE-STD-1241-Based Test Methods for Analog-to-Information Converter. *IEEE Transactions on Instrumentation and Measurement*, 69(4), 1609-1619. doi: 10.1109/TIM.2019.2914132.

Sutcliffe, M., Weston, M., Dutton, B., Charlton, P. & Donne, K. (2012). Real-time full matrix capture for ultrasonic non-destructive testing with acceleration of post-processing through graphic hardware. *NDT & E International*, 51, 16-23. doi: https://doi.org/10.1016/j.ndteint.2012.06.005.

Tiran, E., Deffieux, T., Correia, M., Maresca, D., Osmanski, B.-F., Sieu, L.-A., Bergel, A., Cohen, I., Pernot, M. & Tanter, M. (2015). Multiplane wave imaging increases signal-to-noise ratio in ultrafast ultrasound imaging. *Physics in Medicine & Biology*, 60(21), 8549. doi: 10.1088/0031-9155/60/21/8549.

Tropp, J. A. & Gilbert, A. C. (2007). Signal Recovery From Random Measurements Via Orthogonal Matching Pursuit. *IEEE Transactions on Information Theory*, 53(12), 4655-4666. doi: 10.1109/TIT.2007.909108.

Trucco, A. (1999). Thinning and weighting of large planar arrays by simulated annealing. *IEEE Transactions on Ultrasonics, Ferroelectrics, and Frequency Control*, 46(2), 347-355. doi: 10.1109/58.753023.

Wilcox, P. D., Holmes, C. & Drinkwater, B. W. (2007). Advanced Reflector Characterization with Ultrasonic Phased Arrays in NDE Applications. *IEEE Transactions on Ultrasonics, Ferroelectrics, and Frequency Control*, 54(8), 1541-1550. doi: 10.1109/TUFFC.2007.424.

Wildes, D., Chiao, R., Daft, C., Rigby, K., Smith, L. & Thomenius, K. (1997). Elevation performance of 1.25D and 1.5D transducer arrays. *IEEE Transactions on Ultrasonics, Ferroelectrics, and Frequency Control*, 44(5), 1027-1037. doi: 10.1109/58.655628.

Xu, Q., Wang, H., Yao, Y. & Li, X. (2021). Compressive Sensing for Full Matrix Capture RF Signals Reconstruction in Ultrasonic Array. *2021 IEEE Far East NDT New Technology & Application Forum (FENDT)*, pp. 309-317. doi: 10.1109/FENDT54151.2021.9749669.

Xu, Q., Wang, H., Tian, G., Ma, X., Hu, B. & Chu, J. (2023). Compressive sensing of ultrasonic array data with full matrix capture in nozzle welds inspection. *Ultrasonics*, 134, 107085. doi: https://doi.org/10.1016/j.ultras.2023.107085.

Yoo, J., Becker, S., Monge, M., Loh, M., Candès, E. & Emami-Neyestanak, A. (2012). Design and implementation of a fully integrated compressed-sensing signal acquisition system. *2012 IEEE International Conference on Acoustics, Speech and Signal Processing (ICASSP)*, pp. 5325-5328. doi: 10.1109/ICASSP.2012.6289123.

Yoon, H. & Song, T.-K. (2020). Sparse Rectangular and Spiral Array Designs for 3D Medical Ultrasound Imaging. *Sensors*, 20(1). doi: 10.3390/s20010173.

Zhang, H., Bai, B., Zheng, J. & Zhou, Y. (2020). Optimal Design of Sparse Array for Ultrasonic Total Focusing Method by Binary Particle Swarm Optimization. *IEEE Access*, 8, 111945-111953. doi: 10.1109/ACCESS.2020.3001947.

Zhang, J., Drinkwater, B. W. & Wilcox, P. D. (2013). Comparison of ultrasonic array imaging algorithms for nondestructive evaluation. *IEEE Transactions on Ultrasonics, Ferroelectrics, and Frequency Control*, 60(8), 1732-1745. doi: 10.1109/TUFFC.2013.2754.

Zhang, J., Wang, Y., Liu, J., He, Q., Wang, R., Liao, H. & Luo, J. (2022). Acceleration of reconstruction for compressed sensing based synthetic transmit aperture imaging by using in-phase/quadrature data. *Ultrasonics*, 118, 106576. doi: https://doi.org/10.1016/j.ultras.2021.106576.